

Kaon and open charm production in central lead-lead collisions at the CERN SPS

**Kaon en open charm productie in centrale lood-lood
botsingen aan het SPS te CERN**

(met een samenvatting in het Nederlands)

Proefschrift

TER VERKRIJGING VAN DE GRAAD VAN DOCTOR
AAN DE UNIVERSITEIT UTRECHT
OP GEZAG VAN DE RECTOR MAGNIFICUS, PROF. DR. W.H. GISPEN,
INGEVOLGE HET BESLUIT VAN HET COLLEGE VOOR PROMOTIES
IN HET OPENBAAR TE VERDEDIGEN OP
MAANDAG 19 MEI DES OCHTENDS TE 10:30 UUR

DOOR

Marco van Leeuwen

Geboren op 13 juli 1975, te Amsterdam

promotor: **Prof. Dr. R Kamermans**
Faculteit Natuur- en Sterrenkunde
Universiteit Utrecht

copromotor: **Dr. M.A.J. Botje**
Nationaal Instituut voor Kernfysica en
Hoge-Energiefysica, Amsterdam

Dit werk is onderdeel van het onderzoeksprogramma van de “Stichting voor Fundamenteel Onderzoek der Materie” (FOM), financieel gesteund door de “Nederlandse Organisatie voor Wetenschappelijk Onderzoek” (NWO).

Contents

1	Introduction	1
2	Theory	3
2.1	Quarks, gluons, and hadrons	3
2.2	The Quark Gluon Plasma	4
2.2.1	The MIT bag model	4
2.2.2	Lattice QCD	6
2.3	The Quark Gluon Plasma in the laboratory	6
2.4	Kinematics	8
2.5	Glauber models	9
2.6	Particle production in superposition models	10
2.6.1	RQMD	11
2.6.2	Open charm production in PYTHIA	12
2.7	Thermodynamical models	14
2.7.1	Hadron Gas Model	14
2.7.2	Statistical Model of the Early Stage	17
3	Experiment	21
3.1	Accelerator and beams	21
3.2	Detector overview	22
3.3	Beam detectors and trigger	22
3.4	Veto calorimeter and centrality selection	24
3.5	Magnetic field	26
3.6	Time projection chambers	27
3.7	TOF detectors	28
3.8	Data acquisition and event rates	28
3.9	Data samples	29
4	Reconstruction procedure	31
4.1	Track reconstruction	31
4.1.1	Cluster finding	31
4.1.2	Tracking	33
4.1.3	Track fitting	33
4.2	Ionisation energy loss measurement	34
4.2.1	Corrections and calibrations	35
4.2.2	Truncated mean calculation	37

4.2.3	Global dE/dx	38
5	Kaon spectra at 40, 80 and 158 A·GeV	39
5.1	Event cuts	39
5.2	Track cuts	40
5.3	Combined TOF- dE/dx measurement	41
5.4	Spectra analysis	41
5.5	Acceptance and efficiency	44
5.6	Results	46
5.7	Systematic errors	50
6	Discussion of the kaon analysis results	53
6.1	Shapes of the spectra	53
6.2	Hadron Gas Model fit	56
6.3	Energy dependence of kaon yields	57
6.4	Statistical Model of the Early Stage	59
7	Open charm analysis	61
7.1	Invariant mass analysis	61
7.2	Data samples and cuts	62
7.3	dE/dx selection of kaons	63
7.3.1	Comparison of the different data samples	63
7.3.2	Selection procedure	65
7.4	Rapidity and transverse momentum distribution	66
7.5	Efficiency and acceptance	67
7.6	Decay angle cuts	70
7.7	Efficiency and invariant mass peak shape	70
7.8	Results	72
8	Discussion of the charm result	77
8.1	Comparison to models	77
8.2	Open charm at RHIC	79
9	Conclusion	81
	References	83

Chapter 1

Introduction

The aim of research in the field of high energy nuclear collisions ('Heavy Ion Physics') is to study nuclear matter under conditions of extreme temperature and pressure, which should ultimately lead to the formation of a new state of matter, the Quark Gluon Plasma, where quarks and gluons are deconfined. This state of matter is thought to have existed in the first few microseconds after the Big Bang and possibly still exists in the cores of heavy neutron stars.

It is expected that such a state of matter can be created in the laboratory, albeit briefly, by colliding heavy nuclei at high energies. Such collisions have been studied over the last twenty years at increasingly high energies.

The experiments described in this thesis were performed using the NA49 detector, a large acceptance spectrometer with particle identification capabilities. The detector is situated at CERN, Geneva, where the Super-Proton Synchrotron provides a beam of lead nuclei with energies up to 158 GeV per nucleon, which are collided with a fixed lead target.

The work in this thesis concerns the study of strange and charm quark production in Pb-Pb collisions. These quarks are heavier than the more abundantly produced up and down quarks and it is expected that the fraction of these quarks in the final state is sensitive to whether the relevant degrees of freedom in the collision are quarks and gluons or hadrons.

In the next chapter, several models for strangeness and charm production at SPS energies are discussed.

The experimental setup and the reconstruction software are described in Chapters 3 and 4. Special attention is given to modifications to the experimental procedures which were introduced for the charm measurement.

The measurement of the momentum spectra of kaons, which are the dominant carriers of strange quarks, is presented in Chapter 5. The measurements were performed at three different beam energies and the resulting energy dependence of strangeness production is discussed in Chapter 6.

The search for the D meson, which is much less abundantly produced than the kaon, in a large sample of events at the highest available beam energy is described in Chapter 7 and the result is discussed in Chapter 8.

A brief overview of the general picture emerging from these measurements concludes the thesis.

Chapter 2

Theory

The goal of research in high-energy nuclear collisions is to investigate the dynamics of the strong interaction in large systems at high energy density, when quarks and gluons are expected to be quasi-free. In the following sections an overview of some of the relevant theoretical ideas will be given. We will first explain why we think quarks and gluons behave as free particles if the energy density is high enough. A number of different approaches to the experimental verification of these ideas will be briefly described, followed by a more detailed discussion of strangeness and charm production in high energy nuclear collisions, which is the subject of this thesis.

2.1 Quarks, gluons, and hadrons

According to our present understanding of particle physics, there are two basic types of matter particles: leptons and quarks. The difference between both types of particles is that leptons are only subject to electro-magnetic and weak interactions, while quarks also participate in the strong interaction.

A very specific property of the strong interaction is that it binds quarks into hadrons in such a way that it is impossible to liberate a quark from a hadron. This property is called confinement.

Two different types of hadrons are observed in nature: mesons, which carry the quantum numbers of a quark-anti-quark pair and (anti-)baryons, which carry the quantum numbers of an (anti-)quark triplet.

All known hadrons are formed from the six basic types (flavours) of quarks. The lightest quarks, the up and down quark, form the lightest hadrons. These are the proton and the neutron, with a mass of about 1 GeV, and the π -meson ($m = 0.14$ GeV). Due to their small mass, the pions are the most abundant particles produced in hadronic interactions. The strange and charm quark are somewhat heavier and form heavier mesons, such as the kaon ($m = 0.5$ GeV) and the D meson ($m = 1.9$ GeV). The production of these particles in Pb-Pb collisions is the subject of this thesis. Even heavier are the bottom and top quarks, but their masses are so large (5 and 175 GeV, respectively), that their production can be neglected here.

The theory of the strong interaction is called Quantum Chromodynamics (QCD) and is part of the Standard Model of particle physics. The gauge particle of QCD, which mediates the strong interaction, is the gluon. Both quarks and gluons carry a quantum

number called colour, which is a charge corresponding to the $SU(3)$ symmetry group in the same way as the electric charge corresponds to the $U(1)$ symmetry group. Due to the fact that gluons carry colour, the coupling constant of QCD becomes large for processes at large distance scales or, equivalently, involving small momentum transfers. As a result, perturbation theory can only be used to make quantitative predictions for hard processes, such as jet production, which involve large momentum transfers.

The only way to quantitatively treat soft processes, which take place at a typical scale of 1 fm (10^{-15} m) or 200 MeV, is lattice QCD. In particular, this technique has been used to calculate the deconfinement phase transition, as described in the next sections.

Soft particle production, however, cannot yet be calculated from first principles in QCD. We therefore have to rely on a number of phenomenological models. Here we distinguish microscopic models, which involve QCD-inspired dynamical simulations of the collision process, and thermodynamical models which do not treat the dynamics in detail. Both classes of models are presented in more detail in Sections 2.6.1 and 2.7.

2.2 The Quark Gluon Plasma

Although quarks are normally confined in hadrons, lattice QCD calculations have shown that at high energy densities the quarks behave as if they were free. In a simple picture, one might imagine that this can be achieved by compressing hadrons until such a high density is reached that the hadrons start to overlap in space and quarks are no longer confined to single hadrons but can move freely through the whole system. This state is called the Quark Gluon Plasma (QGP). In the next section, a phenomenological model, the MIT bag model, will be used to estimate the energy density and temperature which are needed to achieve this state.

2.2.1 The MIT bag model

A convenient phenomenological model of hadrons is the MIT bag model [1]. In this model, the quarks move freely inside a bag from which they cannot escape. The size of the bag is determined by an effective pressure, which is exerted on the bag by the vacuum. This pressure is assumed to be a universal constant for all hadrons, the bag constant B , and can, for example, be estimated from the radius of the proton. Using a proton radius of 0.9 fm in a calculation based on the Dirac equation for massless particles, a bag pressure of $B = 234 \text{ MeV fm}^{-3}$ is obtained [2].

In this simple model, a Quark Gluon Plasma would be a state of matter which exerts a pressure on the vacuum which exceeds the bag pressure. Such a state, if it exists, can be arbitrarily large, and can consist of a large number of quarks and gluons. The equilibrium states of the system can then be described using thermodynamics.

In thermodynamics the state of a system is completely specified by a small number of macroscopic parameters. Examples of these quantities are the temperature, pressure, energy density and entropy density. The relation between these quantities is given by the equation of state.

For a non-interacting gas of particles, the energy (density) can be calculated by multiplying the energy by the number (density) of particles in each state and taking a sum

over all possible particle states. The number densities of particles n_k in each state k are given by the Fermi-Dirac (FD) distribution for fermions and the Bose-Einstein (BE) distribution for bosons (see for example [3]):

$$n_k^{FD} = \frac{1}{e^{E_k/T} + 1} \quad \text{and} \quad n_k^{BE} = \frac{1}{e^{E_k/T} - 1} \quad , \quad (2.1)$$

where E_k is the energy of the state and T the temperature.¹

Multiplying the number densities by the energy of each state and taking the continuum limit, the energy density ϵ is obtained:

$$\epsilon = \frac{g}{(2\pi)^3} \int E \frac{1}{e^{E/T} \pm 1} d^3p. \quad (2.2)$$

The integral runs over all possible momenta \vec{p} of the particles. The factor g is the degeneracy of the states due to internal degrees of freedom such as spin, colour, and quark flavour.

The integral can be evaluated analytically for massless particles. We will for the moment only include gluons and the up and down quarks in our calculation and take the quarks to be massless. This is a good approximation at high temperatures, when the typical energies of the quarks are much larger than their masses. The resulting energy density is:

$$\epsilon = \left(\frac{7}{8}g_q + g_g \right) \frac{\pi^2}{30} T^4, \quad (2.3)$$

where g_q is the degeneracy of the quark states and g_g the degeneracy of the gluon states. There are two states of polarisation for each of the eight colour states of gluons, so the degeneracy of the gluon states is 16. Each quark flavour has 6 states, two spin states and three colour states. This leads to a total degeneracy of the quark states of $g_q = 2 \times 2 \times 6 = 24$ for the two flavours, including the anti-quarks.

The pressure P exerted by a gas on its surroundings can be calculated using an equation analogous to Eq. 2.2, but averaging the momentum components perpendicular to a surface. For massless relativistic particles, the resulting pressure P is simply one third of the energy density [3]:

$$P = \frac{1}{3}\epsilon = \left(\frac{7}{8}g_q + g_g \right) \frac{\pi^2}{90} T^4. \quad (2.4)$$

In the bag model, the transition to the Quark Gluon Plasma occurs when the pressure of the quark gluon gas becomes equal to the bag constant. Using $B = 234 \text{ MeV fm}^{-3}$, we obtain $\epsilon = 3B = 702 \text{ MeV fm}^{-3}$ and, from Eq. 2.3, $T = 144 \text{ MeV}$.

Just below the transition, the gas consists mainly of pions which have no spin and three charge states (positive, negative and neutral). The degeneracy of states in a pion gas is therefore only three, approximately ten times less than in the quark gluon gas. The energy density therefore increases by a factor of ten at the transition from a pion gas to the QGP.

¹Note that the temperature is expressed in units of energy by absorbing the Boltzmann constant k in the temperature. This convention will be used throughout this thesis. The conversion factor between MeV and Kelvin is $1/k = 1.2 \times 10^{10} \text{ K/MeV}$.

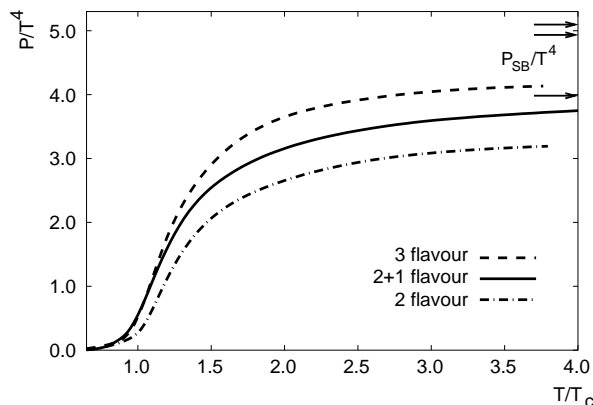


Figure 2.1: Dependence of P/T^4 on the reduced temperature T/T_c as calculated using lattice QCD [4].

2.2.2 Lattice QCD

Numerical calculations starting from the QCD Lagrangian are used to check whether the theory really allows the formation of a state where quarks and gluons are effectively free and to estimate the transition temperature and energy density in more detail. These calculations are performed on a lattice in four-dimensional space-time, with a typical size of 16 cells in each spatial direction and 32 cells in (imaginary) time. Technically, these calculations are very involved and in many cases approximations must be made to reduce the needed computing power.

As an example of the results obtained from lattice QCD, the calculated dependence of P/T^4 on the reduced temperature T/T_c is shown in Figure 2.1 [4]. The different lines indicate calculations with different numbers of quark flavours. The two and three flavour calculations include only light flavours of mass $m/T = 0.4$, while a heavier flavour of mass $m/T = 1$ is included in the 2+1 flavour calculation. The 2+1 flavour calculation has the more realistic quark masses, representing light up and down quarks and a heavier strange quark.

At the critical temperature T_c the ratio P/T^4 suddenly starts to increase, due to the phase transition. The ideal gas limit, which is indicated by arrows in the plot, is never completely reached, even at four times the critical temperature.

Both the critical temperature and the order of the phase transition as calculated with lattice QCD depend on the number of quark flavours in the calculation and their masses. For the critical temperature, values between 150 and 170 MeV are given in the literature, see [5] for instance.

2.3 The Quark Gluon Plasma in the laboratory

Heavy nuclei are collided at high energies to achieve the high energy density which is needed to investigate the Quark Gluon Plasma in the laboratory. Over the last twenty years, high energy collisions of nuclei have been studied in a series of experiments at different accelerators and beam energies. The main sites for these experiments are the

Alternating Gradient Synchrotron (AGS) in Brookhaven, the Super-Proton Synchrotron (SPS) at CERN, and the Relativistic Heavy Ion Collider (RHIC), the new accelerator in Brookhaven. RHIC provides the highest collision energies for nuclei so far, with a maximum centre-of-momentum energy $\sqrt{s} = 200$ GeV per nucleon, approximately ten times the maximum energy at the SPS. The new LHC accelerator which is under construction at CERN will provide lead-lead collisions at $\sqrt{s} = 5.5$ TeV per nucleon, more than twenty times the maximum RHIC energy.

Most of the experimental results obtained so far indicate that, indeed, high energy densities are reached. For example, it is estimated that the initial energy density is $3.2 \text{ GeV}/\text{fm}^3$ in central lead-lead collisions at the highest SPS energy of $\sqrt{s} = 17.3$ GeV per nucleon [6]. This is well above the critical energy density of approximately $1 \text{ GeV}/\text{fm}^3$. The experimental results do not yet have a clear-cut interpretation in terms of whether or not a Quark Gluon Plasma was formed. The main difficulty in the interpretation of the results is that the final state is determined by the full time evolution of the colliding system. In particular, due to our relatively poor theoretical understanding of the hadronisation process, it is difficult to study the initial dynamics in detail by detecting only final state hadrons.

A number of different signals which are sensitive to the initial energy density and the state of matter have been proposed over the years. A brief overview of the present experimental situation and the theoretical understanding of the results is given in the next paragraphs.

Leptons and photons, which are produced much less abundantly than hadrons, are expected to be mainly sensitive to the initial stages of the collision, because they do not participate in the strong interaction and therefore do not have a large probability to interact after their formation. If the early stage is really hot and dense, and has a large enough life-time, one would expect to observe thermal radiation of both photons and electrons. The measurement of their spectra at the SPS has provided a number of interesting observations, but the interpretation of these results is not yet clear [7].

Another probe of Quark Gluon Plasma formation is the production of the J/ψ particle, which is a bound state of a charm and an anti-charm quark. In a QGP, J/ψ production is expected to be suppressed due to the screening of the binding potential between the quark-anti-quark pair by the colour charges in the QGP. Such a suppression has indeed been observed, but a number of alternative explanations exist [8].

A different class of measurements which should be more sensitive to the dynamics in the system, are correlation measurements. Event-by-event fluctuations in a number of variables, such as the mean transverse momentum, the kaon-to-pion ratio and charge ratios, have been studied to search for signs of a first order phase transition (co-existing phases), but no indication of such dynamical fluctuations was found. The measurement of azimuthal correlations, or elliptic flow, has shown that the densities of particles become high enough to build up some pressure in the collision. It is very likely that, at RHIC, this pressure already exists before hadronisation implying collective behaviour or even thermalisation already in the partonic phase. The observed elliptic flow at the SPS is much smaller and it is not yet clear at which point it develops.

The idea that the production of strangeness should be enhanced in a Quark Gluon Plasma is already some 20 years old [9]. It is expected that the strange quark, which has a mass comparable to the expected phase transition temperature, will be as abundantly

produced as the light quarks if a QGP is created in the collision. This represents an enhancement of the strangeness production compared to proton-proton collisions, in which strange quarks are much less abundantly produced than the light quarks. A lot of experimental and theoretical activity has followed the introduction of this idea. A selection of theoretical models is presented in the next sections together with an extension to charm production.

Before going into the more detailed discussion of strangeness production, some relevant kinematic variables are defined in the next section.

2.4 Kinematics

For fixed target experiments, the initial state energy is usually specified as the beam energy per nucleon. The total energy of a 158 A -GeV lead beam is 33 TeV. The collision energy in the centre-of-momentum system \sqrt{s} is usually specified per nucleon pair, giving $\sqrt{s} = 17.3$ GeV for a 158 A -GeV beam colliding with a fixed target.

The final state is fully characterised by the momenta $\vec{p} = (p_x, p_y, p_z)$ and the mass m or the energy E of all particles. The relation between mass, energy and momentum is ²

$$E = \sqrt{m^2 + p^2}, \quad (2.5)$$

where $p = |\vec{p}|$.

Using the (approximate) azimuthal symmetry around the beam direction, and choosing the z -axis along the beam direction, longitudinal and transverse momentum p_z and $p_t = \sqrt{p_x^2 + p_y^2}$ are used to characterise the final state. Alternatively, transverse mass m_t and rapidity y can be used. Rapidity is defined by

$$y = \frac{1}{2} \ln \left(\frac{E + p_z}{E - p_z} \right) \quad (2.6)$$

and has the convenient property that it is additive under Lorentz boosts in the z -direction. The transverse mass

$$m_t = \sqrt{m^2 + p_t^2} \quad (2.7)$$

is obviously invariant under such boosts.

The relations between E , p_z and m_t , y are

$$E = m_t \cosh y \quad \text{and} \quad p_z = m_t \sinh y. \quad (2.8)$$

Particle spectra are distribution functions in momentum space. A Lorentz-invariant distribution function is obtained by multiplying the momentum space distribution function by the energy. The relation between this distribution in longitudinal and transverse momentum and in rapidity- p_t space is

$$E \frac{d^2 N}{p_t dp_t dp_z}(p_t, p_z) = \frac{d^2 N}{p_t dp_t dy}(p_t, y). \quad (2.9)$$

²Throughout this thesis, natural units are used, setting the velocity of light c and Planck's constant \hbar to one. These quantities therefore do not appear in equations.

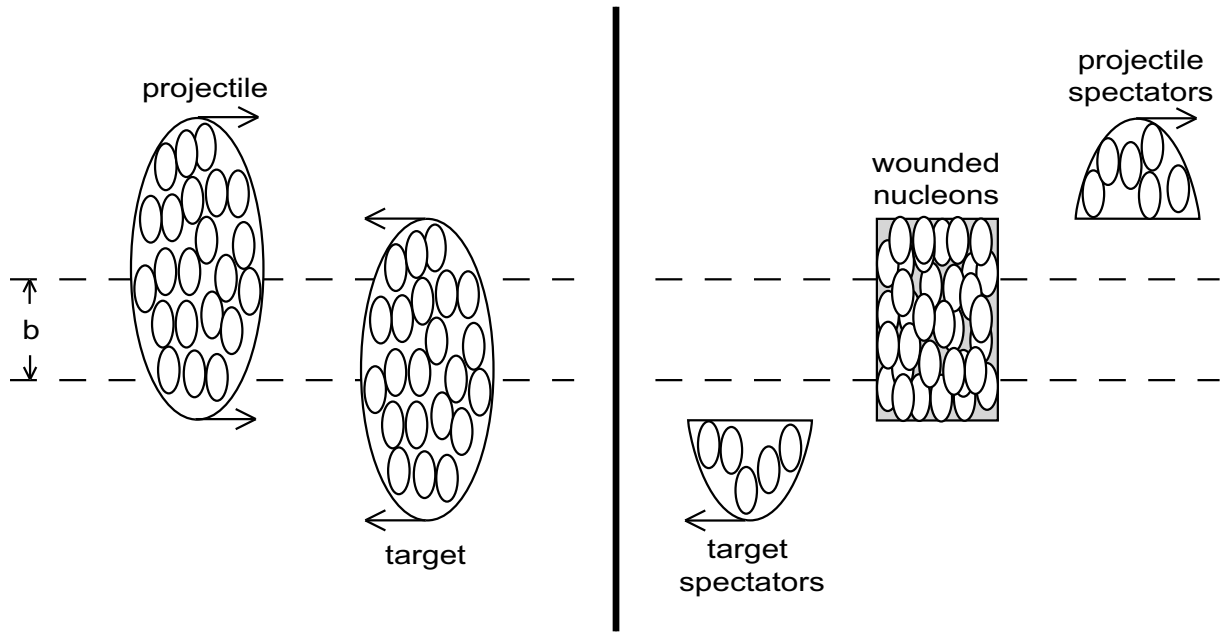


Figure 2.2: *The geometrical picture of the collision (as seen in the centre-of-momentum system) at the basis of Glauber models.*

2.5 Glauber models

In order to recognise QGP formation in nucleus-nucleus collisions, a reference model for nucleus-nucleus events without a QGP is needed. Since soft particle production cannot be calculated from first principles, the reference model must be based on experimental information on nucleon-nucleon cross-sections. Nuclear collisions can then be described as a superposition of more or less independent nucleon-nucleon interactions. Such a superposition model is called a Glauber model [10].

Glauber models start from a geometrical picture of the collision, as sketched in Figure 2.2. The distance between the trajectories of the centres of the nuclei is called the impact parameter b . The size and shape of the region where nucleons of both nuclei collide is determined by this parameter.

In general, when two nucleons meet they can either have an interaction, be it elastic or inelastic, or they can go on without interacting. Since only inelastic interactions contribute to particle production, we will, for the moment, disregard elastic interactions and say that two nucleons collide if and only if they have an inelastic interaction.

Three different ways of counting the number elementary interactions in a nucleus-nucleus event are used in the literature. The first two are based on counting the number of nucleons which participated in the interaction. From the purely geometrical interpretation as illustrated in Figure 2.2, the total number of nucleons which collided with a nucleon from the other nucleus can be computed. We will call this the ‘number of wounded nucleons’ N_w . Using an event generator, one will in addition find nucleons which collided with particles which were produced in the interaction. By including these nucleons, a slightly larger number of ‘participating’ nucleons N_{part} is obtained. Since the probability for a nucleon to collide with a produced particle is relatively small, the distinction between N_w and N_{part} is mainly important for very peripheral collisions (large b), where there are

many spectator nucleons. The maximum number of wounded nucleons and the maximum number of participants are both equal to the total number of nucleons in the colliding nuclei.

Each nucleon, however, may have more than one interaction. The total number of binary collisions N_{coll} is therefore also used to characterise nucleus-nucleus collisions. This number includes all collisions between two nucleons, whether they were already hit by another nucleon or not. It can therefore be much larger than the total number of nucleons in the colliding nuclei.

The simplest geometrical model of a nucleus is the ‘hard sphere’ geometry: a sphere with a uniform density of nucleons, with a radius R_A which depends on the atomic number A like

$$R_A = 1.12 A^{1/3}. \quad (2.10)$$

With this simple geometry, the values of N_w and N_{coll} for central collisions with $b = 0$ can be analytically calculated. In such collisions, all nucleons will be hit, so $N_w = 2A$. The number of elementary collisions in a central collision ($b = 0$) is [11]

$$N_{coll} = \frac{9}{8} \frac{A^2}{\pi R_A^2} \sigma_{coll} = 0.29 \text{ fm}^{-2} A^{4/3} \sigma_{coll}, \quad (2.11)$$

for a process with an interaction cross section σ_{coll} . Using the total inelastic proton-proton cross section of 30 mb, one arrives at $N_{coll} \approx A^{4/3}$ for central collisions.

A more realistic model of the nuclear density is the Woods-Saxon distribution

$$\rho(r) = \frac{\rho_0}{1 + e^{(r-R_A)/d}}, \quad (2.12)$$

where R_A is the radius of the nucleus, as given by Eq. 2.10, ρ_0 a normalisation constant and d the thickness of the region in which the density goes to zero. For ^{208}Pb , these parameters are $R_A = 6.62$ fm ($R_A = 6.64$ fm using Eq. 2.10) and $d = 0.546$ fm [12], as obtained from low-energy electron scattering experiments. The resulting normalisation density is $\rho_0 = 0.160$ fm $^{-3}$. Using this distribution, the dependence of the number of wounded nucleons and the number of binary collisions on the impact parameter b can be numerically calculated.

2.6 Particle production in superposition models

The simplest model for particle production in nucleus-nucleus collisions is a superposition of independent nucleon-nucleon collisions at the same centre-of-momentum energy. More complicated models, which take into account coherence effects or the energy lost by nucleons in subsequent interactions and the interactions between produced particles are implemented in event generators. First, the most simple, analytically calculable models are discussed.

The first is the wounded nucleon model [13], which was inspired by measurements of the total multiplicity in proton-nucleus interactions. The assumption here is that the yields in nucleus-nucleus collisions are simply N_w times the yields in nucleon-nucleon collisions. This would imply that nucleons which undergo several collisions produce the same final state as nucleons which are hit only once.

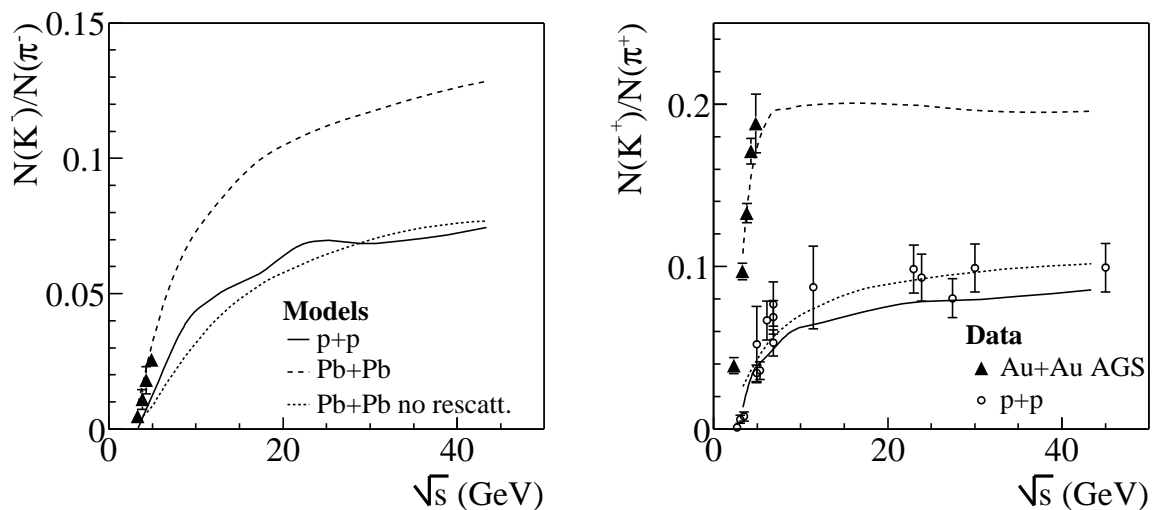


Figure 2.3: Energy dependence of the kaon to pion ratio in proton-proton (full line) and nucleus-nucleus (dashed line) collisions in RQMD. The left panel shows the ratio for negative particles, the right panel for positives. The predictions are compared to experimental results on nucleus-nucleus collisions at the AGS (triangles) and collected data on proton-proton collisions (circles). Also shown is the prediction for nucleus-nucleus collisions by RQMD without rescattering of hadrons and colour rope formation (dotted line), which are specific to nuclear collisions.

It is, however, also reasonable to assume that particle production scales with the number of binary collisions N_{coll} . This is in particular expected for rare processes, where the probability for the process to occur in a nucleon-nucleon collision is small. For instance, it has experimentally been shown that muon pair production in the Drell-Yan process is proportional to N_{coll} [14].

More detailed extrapolation from nucleon-nucleon collisions to nucleus-nucleus collisions are implemented in a number of event generators. A large number of generators is available, based on a variety of assumptions. In particular, there is a class of models which does take into account scattering between produced particles, and a group of models which does not do this. Models such as FRITIOF [15], LEXUS [16] and HIJING [16] fall in the last category, while VENUS [17], RQMD [18], UrQMD [19] and HSD [20] belong to the first category. These models will not be discussed in detail, but we will use RQMD as an example to illustrate the implications of scattering between produced particles for strangeness production in Pb-Pb collisions.

Not all of the mentioned event generators calculate charm production and those which do (HIJING, FRITIOF), are based on older versions of PYTHIA. Instead of these generators, a recent version of PYTHIA is used to generate proton-proton events and the result is scaled by N_{coll} to obtain predictions for Pb-Pb collisions.

2.6.1 RQMD

The RQMD (Relativistic Quantum Molecular Dynamics) event generator [18] is based on a Glauber model calculation in which excited strings are formed when two nucleons meet in a nucleus-nucleus collision. These strings subsequently decay into hadrons. In the

model, the momentum transfer between the interacting nucleons is absorbed by one quark in each nucleon, which causes a quark-anti-quark pair to be polarized out of the sea. A string is formed between the interacting valence quark and the anti-quark from the sea, and another string stretches between the spectator di-quark and the quark from the sea. This process is repeated in subsequent interactions and several strings can be formed from each nucleon in a nuclear collision. In RQMD therefore, all particle production scales with the number of binary proton-proton collisions N_{coll} in the high energy limit. At the SPS, however, the scaling is close to wounded nucleon scaling due to energy loss in subsequent collisions.

The formation of hadrons from strings in RQMD is based on the Lund string fragmentation scheme [21]. The probability to form a light quark-anti-quark pair in this scheme is approximately three times higher than the probability to form a strange-anti-strange pair. These probabilities do not depend on the total string energy, but are determined by the local energy density in the string and by the quark masses. The ratio between strange and non-strange quark production in string fragmentation is the main parameter which determines the kaon to pion ratio in the final state. This is demonstrated in Figure 2.3, where it is seen that the kaon to pion ratio for proton-proton collisions (solid line) is similar to the ratio in nucleus-nucleus collisions without colour rope formation (see below) and rescattering (dotted line). This observation holds for the negative particles (left panel) as well as for the positive particles (right panel).

In the full RQMD model, the kaon to pion ratio for nuclear collisions is higher due to colour rope formation and rescattering of produced particles. Colour ropes are formed when two strings overlap in space and time. A colour rope is similar to a string but has higher colour charges at its ends. As a result, the colour field in the rope is stronger and the probability to form a strange-anti-strange quark pair is larger.

Scattering between produced particles is treated in detail by tracking all produced particles through space. When particles come close enough, they have a certain probability to interact. The cross-sections for rescattering used in RQMD are based on relatively simple resonance models, which have been verified using experimental data when available (e.g. data on pion-nucleon and kaon-pion scattering).

The decay of heavy resonances which can be formed by subsequent inelastic collisions in dense systems leads to an increase of kaon production. The kaon to pion ratios as calculated using RQMD, including effects of rescattering and colour rope formation are in good agreement with experimental results at the AGS, as shown in Figure 2.3. In Chapter 6, the RQMD calculations will be compared to the results of the kaon analysis as described in this thesis.

2.6.2 Open charm production in PYTHIA

The PYTHIA [24] event generator calculates charm production using leading order perturbative QCD calculations and subsequent string fragmentation for the hadronisation. In Figure 2.4 the total cross section for D^0 and \bar{D}^0 production in proton-proton collisions as predicted by PYTHIA is compared to experimental results [22]. Note that all measurements are at energies above the maximum SPS energy ($\sqrt{s} = 17.3$ GeV for lead nuclei). The PYTHIA calculation is taken from [23], where the calculated leading order cross-section was multiplied by a factor 3.5 (K-factor) to reproduce the experimental data.

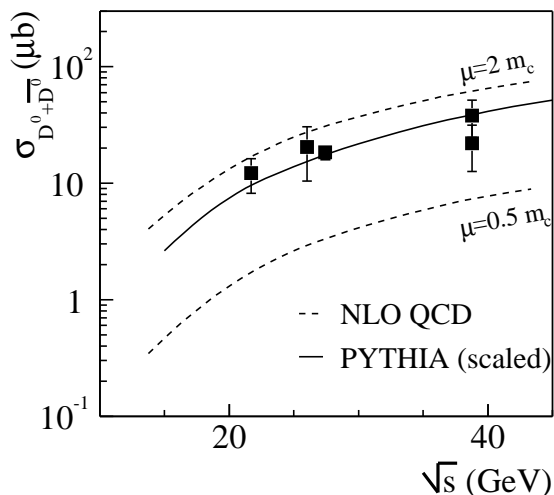


Figure 2.4: Energy dependence of the neutral D meson production cross section. Experimental data are compared to a NLO QCD calculation [22] (dashed curve) and a scaled (see text) PYTHIA calculation [23] (full curve).

This curve will be used to extrapolate the open charm production cross-section to SPS energies.

For comparison, the result of a next-to-leading order (NLO) perturbative QCD calculation [22] is indicated by dashed lines in Figure 2.4. Two results using different values for the renormalisation scale μ_r are shown to indicate the theoretical uncertainty. A simple hadronisation scenario was used to convert the calculated total charm production cross-section into a neutral D meson cross-section. Based on measurements at 350 GeV beam energy [25], it was assumed that the yields of Λ_c^+ and D_s are 50% of the non-strange open charm yield. The charged D yield is 30% of the neutral D yield, because most of the D mesons are produced in decays of D resonances. These resonances ($D^*(2007)^0$ and $D^*(2010)^+$), are close in mass to the D mesons but have three polarisation states, and will therefore be approximately three times more abundant. The resonances preferably decay into D^0 . These ratios between the different charmed particles, which are approximately reproduced by PYTHIA, are assumed to be independent of beam energy. For a more detailed discussion, see [22]. It can be seen in Figure 2.4 that when the measured open charm yields are used to normalise the NLO calculation, the expected cross section at SPS energies will be very close to the values from PYTHIA calculation.

The total neutral D meson cross-section extrapolated to 158 $A \cdot \text{GeV}$ is $4.4 \mu\text{b}$ in proton-proton events leading to a multiplicity of (using a total inelastic cross-section of 30 mb) $1.5 \cdot 10^{-4} D^0 + \bar{D}^0$ per event. From Eq. 2.11 we find that the expected multiplicity in central Pb+Pb events is 0.18 per event. In this calculation, it is assumed that the charm production mechanism in nucleus-nucleus collisions is exactly the same as in proton-proton collisions. The experimentally observed J/ψ suppression (see Section 2.3), for example, is relative to this expectation.

In the previous section it was shown that collisions between produced particles contribute significantly to the kaon yield in RQMD. It is not expected that these processes will contribute much to the open charm yield, because the energy available in final state

collisions is too small to produce D mesons. Colour rope formation might increase the open charm yield similarly to the strangeness yield, but this cannot be verified quantitatively, since a calculation of charm production is not available in the RQMD model.

2.7 Thermodynamical models

A completely different approach to the description of heavy ion collisions are thermodynamical models. These models do not treat the collisions between particles in detail, like RQMD and PYTHIA, but assume that the final state is that with the largest entropy. This idea was originally brought forward by Fermi [26] and Landau [27]. Later on, Hagedorn [28] revived interest in this model. Their work is the basis of what is now known as the thermodynamical Hadron Gas Model, which is widely applied to describe hadron production in nucleus-nucleus collisions. A number of slightly different formulations exist, some of which will be explained in the next section.

The Hadron Gas Model gives a reasonable description of the yields of all particles produced in nucleus-nucleus collisions, as well as in elementary collisions (e^+e^- and $p\bar{p}$), in terms of only a few parameters. This should be contrasted with microscopic models which have a large number of free parameters. Even if these parameters are tuned on proton-proton collisions, it is by no means clear how to extend the models to nucleus-nucleus collisions.

A different type of thermodynamical model is the Statistical Model of the Early Stage (SMES). In this model it is assumed that the quarks and gluons which dominate the early stage of the collision are already thermalised, forming a QGP as described in Section 2.2.1. A more detailed description of the model will follow in Section 2.7.2.

2.7.1 Hadron Gas Model

The basic idea of the Hadron Gas Model is to describe the final state of a collision as a gas of hadrons and resonances. In such a description, the number densities and momentum distributions of particles are determined by the list of available states, which is completely determined by the existing types of hadrons and resonances, and by the number density of particles in each state, which for each state depends on its energy and the temperature. For simplicity, the Boltzmann distribution

$$n_k^B = e^{-E/T} \quad (2.13)$$

is often used for these calculations. The Boltzmann distribution is a good approximation of both the Fermi-Dirac and Bose-Einstein distributions of Eq. 2.1, when the energies of most occupied states are larger than the temperature, which is true for all particles at the relevant temperatures. The resulting particle density n_i for a species of particles i with mass m_i and degeneracy g_i is [29]

$$n_i = g_i \int \frac{d^3p}{(2\pi)^3} e^{-(E_i - \mu_i)/T} = \frac{g_i m_i^2 T}{2\pi^2} K_2(m_i/T) e^{\mu_i/T}, \quad (2.14)$$

where K_2 is the modified Bessel function and the chemical potential μ_i is introduced. From Eq. 2.14 it is clear that the chemical potential effectively shifts the energies of all states. It

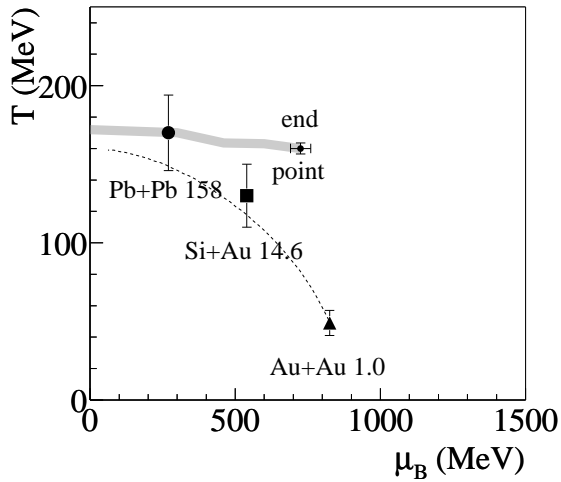


Figure 2.5: The values of temperature T and baryon chemical potential μ_B from hadron gas fits to experimental data at different energies (indicated at each point in $A \cdot \text{GeV}$). Also shown is the phase boundary from a recent lattice QCD calculation [30], and a parametrization of the relation between T and μ_B from the data [29] (see text for details).

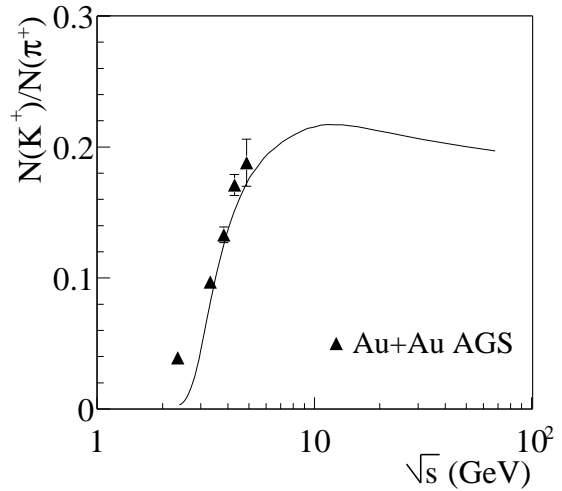


Figure 2.6: Predicted K^+/π^+ ratio as a function of \sqrt{s} , using the hadron gas model, assuming that T and μ_B evolve smoothly with energy [31]. The points are calculated from total kaon and pion yields measured at the AGS.

can be interpreted as the minimum energy which is needed to add a particle to the system. In the Hadron Gas Model, the chemical potential is used to impose the conservation of the baryon number of the incoming particles and to ensure that the produced particles carry no net strangeness or charm. This is achieved by making the chemical potential for each particle species depend on the baryon number b_i and the strange and charm quantum numbers s_i and c_i . Each quantum number has a corresponding chemical potential:

$$\mu_i = b_i\mu_B + s_i\mu_S + c_i\mu_C. \quad (2.15)$$

Since the strangeness and charm chemical potentials μ_S and μ_C are determined from the requirement that the final state has zero net strangeness and charm content, the number densities of the different particles are completely determined by the temperature T and the baryon chemical potential μ_B . The measured particle yields can therefore be used to determine these parameters and a normalisation volume V . The values of T and μ_B , the so-called freeze-out points, as obtained from fits to the particle yields measured in a number of experiments at different energies [29] are shown in Figure 2.5. The grey band indicates the phase boundary from recent lattice QCD calculations [30]. According to these calculations the phase transition at $\mu_B = 0$ is neither first- nor second-order but a cross-over transition. The phase boundary was only calculated up to the end-point, where the nature of the transition changes, probably to a first-order phase transition. The continuation of the phase boundary beyond the end-point is not well known.

The temperature obtained from the fits of the Hadron Gas Model to the experimental data clearly increases with beam energy, while the baryon chemical potential decreases.

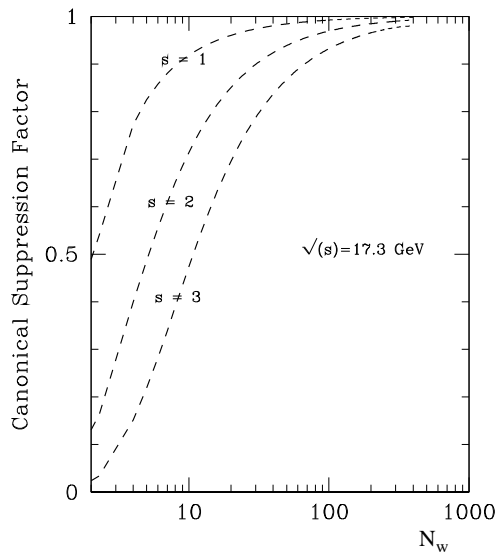


Figure 2.7: *Dependence of the canonical suppression factor on the number of wounded nucleons, at a beam energy of 158 A·GeV. [33]*

The dashed line in Figure 2.5 is a parametrisation of the freeze-out curve, which is defined by imposing the requirement that the average energy of the produced particles is 1 GeV [29]. At low beam energies, the freeze-out points are far from the phase boundary, indicating that the system has probably not been dense enough for QGP formation. For 158 A·GeV Pb-Pb collisions, the temperature is close to the transition temperature as obtained from lattice QCD. Note that due to the phase transition, a hadron gas can never reach a temperature above the critical temperature. It is therefore not excluded that at the highest SPS energy the system has reached higher temperatures during its time evolution, thereby crossing the phase transition.

The Hadron Gas Model was recently extended by parametrising the dependence of the temperature and baryon chemical potential on the collision energy and using the parametrisation to calculate particle yields as a function of energy. The resulting energy dependence of the K^+/π^+ ratio [29] is shown in Figure 2.6 and compared to AGS data (see references in [32]).

Introducing a chemical potential such as Eq. 2.15 is a convenient way to impose conservation laws. Strictly speaking, however, this is an approximation which is only valid when the system contains a large number of particles carrying the conserved quantum numbers, because the calculation of the Boltzmann distribution includes states of the system which violate the conservation laws. It can be shown that if a system contains a large number of particles with the conserved quantum number, the contribution of states which violate the conservation laws is small, and the approximate treatment is valid. If, however, the number of particles carrying the conserved quantum number is small, the conservation laws must be explicitly taken into account, using the canonical formalism. As an example, we quote the kaon yield N_K , as obtained from the canonical calculation [33]

$$N_K = N_K^{GC} \frac{N_{S=1}}{\sqrt{N_{S=1}N_{S=-1}}} \frac{I_1(x_1)}{I_0(x_1)}, \quad (2.16)$$

where $N_{S=1}$ is the total number of particles with strangeness 1 (mainly anti-lambdas

and kaons) and $N_{S=-1}$ is the total number of particles with strangeness -1 (mainly lambdas and anti-kaons), calculated using the grand canonical approach (using Eq. 2.14). The difference between the yield N_K^{GC} in the grand canonical and N_K in the canonical calculation is determined by the ratio of the modified Bessel functions I_0 and I_1 . This ratio is therefore called the ‘canonical suppression factor’. The canonical suppression factor depends on the system size through the arguments $x_1 \equiv 2\sqrt{N_{S=1}N_{S=-1}}$ of the modified Bessel functions.

The general expression for the canonical suppression is $I_s(x_1)/I_0(x_1)$ for particles with strangeness content s . In Figure 2.7, the dependence of the canonical suppression factor on the number of wounded nucleons N_w for nuclear collisions at 158 A-GeV is shown for particles with one, two and three strange quarks. At large numbers of participants the canonical suppression factor approaches 1, indicating that the difference between the canonical calculation and the grand-canonical calculation vanishes. The deviation from the grand-canonical limit for kaons is already below 10% at approximately 20 participants. For proton-proton collisions, with 2 wounded nucleons the strangeness suppression factor is 0.5. Within this model, the production of kaons in proton-proton collisions is suppressed due to strangeness conservation. This explains, at least qualitatively, the difference between the kaon to pion ratio in proton-proton and nucleus-nucleus collisions as seen in Figure 2.3.

Some authors introduce a strangeness suppression parameter γ_s , allowing the strangeness yield to deviate from the equilibrium value. The yields of particles containing one strange quark are lower by a factor γ_s than calculated from Eq. 2.16 (or Eq. 2.14) and particles with two strange quarks are suppressed by γ_s^2 . A similar approach can be used to describe charm production. Using the J/ψ yields as measured by NA50 as input, charm enhancement factors of $\gamma_c = 1.3$ – 1.9 have been calculated [34], leading to total charm pair yields of 0.5–0.6 per event in central 158 A-GeV Pb-Pb collisions.

2.7.2 Statistical Model of the Early Stage

Since the Hadron Gas Model only describes the collision in terms of the hadronic degrees of freedom, it does not give much insight into the question whether a Quark Gluon Plasma is formed. In this section a model will be described which explicitly introduces a QGP state, much along the lines of the discussion in Section 2.2.1. This ‘Statistical Model of the Early Stage’ (SMES) [35] is based on a thermodynamical treatment of the initial state in the collision, using quarks and gluons as the degrees of freedom.

A basic assumption in the model is that the total energy E in the collision area is a fixed fraction η of the available energy, which is the centre of mass energy of the colliding nuclei minus the energy carried away by the participating baryons (i.e. their mass m_N):

$$E = \eta(\sqrt{s} - 2m_N)N_w. \quad (2.17)$$

The energy is deposited in the Lorentz contracted volume of the nuclei. Assuming that the non-contracted volume is proportional to the number of wounded nucleons N_w , the contracted volume is proportional to N_w/γ . The resulting energy density ϵ is then

$$\epsilon \propto (\sqrt{s} - 2m_N)\gamma = \frac{(\sqrt{s} - 2m_N)\sqrt{s}}{m_N}. \quad (2.18)$$

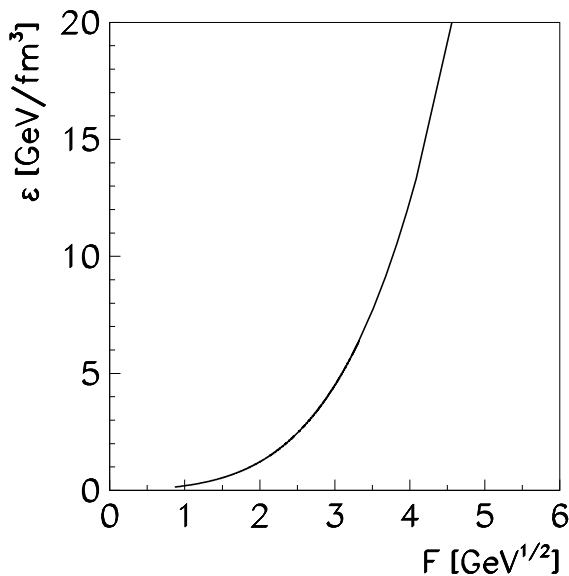


Figure 2.8: *The energy density ϵ in the early stage as function of the collision energy [35].*

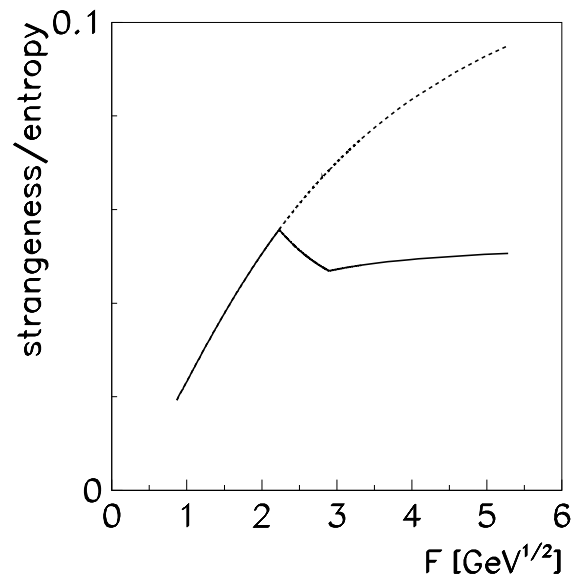


Figure 2.9: *The strangeness to entropy ratio in the statistical model of the early stage. The full line is the expected dependence on the collision energy for a phase transition at a temperature of 200 MeV. The dotted line is the continuation of the behaviour of the hadron phase [35].*

The relation between the calculated energy density and the collision energy expressed using Fermi's collision energy variable

$$F = \frac{(\sqrt{s} - 2m_N)^{3/4}}{(\sqrt{s})^{1/4}} \approx s^{1/4} \quad (2.19)$$

is shown in Figure 2.8. The particle content at the early stage can be calculated from the energy density using the equation of state. At high initial energy density, the 'bag equation of state' is used, meaning that the energy density is the sum of the energy density of an ideal quark-gluon gas and the bag constant B . At lower energies, the equation of state is based on a calculation with effective degrees of freedom. Since the equilibrium state at each temperature is the state with the highest entropy, the transition between both states occurs at the temperature where the entropy in the low-energy state is equal to the entropy in the QGP-state. This temperature is fixed at 200 MeV in the model, by using a bag constant B of 600 MeV/fm³. The resulting phase transition is first-order, because the energy density in the different states is different at the transition temperature.

Finally, to calculate the yields of hadrons, it is assumed in the SMES that the total number of strange and charm quarks and the total entropy are the same before and after hadronisation.

In an ideal gas of massless particles, each particle carries approximately 4 units of entropy [2]. The model therefore assumes that the entropy in the final state is proportional to the total number of pions. The pion multiplicity per wounded nucleon is then

proportional to the entropy density σ , divided by γ due to the Lorentz contraction of the initial volume. Using the thermodynamical relation $\sigma \propto g^{1/4}\epsilon^{3/4}$, the simple relation

$$\frac{N(\pi)}{N_w} \propto \frac{\sigma}{\gamma} \propto \frac{g^{1/4}\epsilon^{3/4}}{\gamma} \propto g^{1/4} \frac{(\sqrt{s} - 2m_N)^{3/4}}{(\sqrt{s})^{1/4}} = g^{1/4}F, \quad (2.20)$$

is obtained. The pion multiplicity per wounded nucleon is proportional to F , with a constant of proportionality which depends on the number of degrees of freedom g in the early stage.

The energy dependence of the ratio of the total number of strange and anti-strange quarks $N_{s\bar{s}}$ to the total entropy S as calculated in the full model [35] is shown in Figure 2.9. The full model calculation involves the numerical evaluation of integrals over Fermi-Dirac and Bose-Einstein distributions (see Eq. 2.1), including the effects of the masses of the strange degrees of freedom. At low energies the model uses 16 effective massless non-strange degrees of freedom and 14 effective massive ($m = 500$ MeV) strange degrees of freedom. Due to the large mass of the strange degrees of freedom, the strangeness to entropy ratio increases rapidly with collision energy at low energies.

When the phase transition temperature of $T = 200$ MeV is reached, at $F \approx 2$ GeV^{1/2}, a mixed phase is formed with an increasing fraction of QGP, which causes the drop in the strangeness to entropy ratio. The masses of the strange and charm quarks in this phase are $m_s = 175$ MeV and $m_c = 1.5$ GeV respectively. Above $F \approx 2.7$ GeV^{1/2}, the initial state is purely QGP. In the model, the initial temperature keeps increasing with beam energy. At high temperature and energy density, when the strange degrees of freedom become effectively massless, the strangeness to entropy ratio $N_{s\bar{s}}/S$ saturates at a value of

$$\frac{N_{s\bar{s}}}{S} = \frac{1}{4} \frac{g_s}{g}, \quad (2.21)$$

where g and g_s are the total and strange numbers of degrees of freedom and the factor 1/4 stems from the fact that each massless quark carries 4 units of entropy. Note that Eq. 2.21 is almost model-free, the only assumption being that the quarks and gluons in the initial state form a thermalised QGP.

The sharp peak in the strangeness to entropy ratio, which is due to the phase transition, is a characteristic feature of this model. Other models expect a smoother evolution of this quantity. The energy dependence of the strangeness to entropy ratio will be compared to experimental data in Chapter 9.

The initial temperature of 264 MeV for 158 A-GeV collisions at the SPS gives an estimated yield of a total of 17 charm quarks and anti-quarks in a central Pb-Pb collision [35]. Due to the large mass of the charm quark, this yield is strongly dependent on the initial temperature.

The expected charm yield within the SMES is much higher than the expected yields from the Hadron Gas Model and the value obtained by scaling the expected multiplicity in proton-proton collisions by the number of binary collisions N_{coll} . The result of charm analysis presented in Chapter 7 is confronted with these expectations in Chapter 8.

Chapter 3

Experiment

The measurements described in this thesis are part of the experimental program of the NA49 collaboration. The NA49 detector is located in the North Area of the European Centre for Nuclear Research (CERN) in Geneva. The experiment uses beams from the Super Proton Synchrotron (SPS), a circular accelerator with a circumference of 6.9 km.

The detector has been designed to measure a large fraction of the approximately two thousand charged particles produced in lead-lead collisions. The experimental setup consists of a large acceptance magnetic spectrometer, using large Time Projection Chambers (TPCs) which combine a momentum measurement with particle identification capabilities through a measurement of the ionisation energy loss. Additional detectors provide a measurement of the incoming beam, the centrality, and of the time-of-flight of produced particles. The different detector components will be briefly described in this chapter, with some emphasis on the special configuration of the detector read-out which was used to increase the event rate for the search for open charm in the year 2000. A detailed description of the detector can be found in [36].

3.1 Accelerator and beams

The SPS accelerator delivers beams to several experiments in the North and West experimental Areas at CERN. During normal operation with proton or ion beams, a beam is received from the Proton Synchrotron and accelerated to the desired energy every 15–20 seconds. During the last 2–5 seconds of the machine cycle the beam is gradually extracted and delivered to the experiments.

The maximum attainable energy, which is determined by the magnetic field in the bending magnets, is 400 GeV for protons. The maximum energy per nucleon for ions scales with the charge-to-mass ratio Z/A and thus depends on the type of nucleus. Most of the data were taken with a lead beam at the maximum energy of 158 $A\cdot\text{GeV}$. Part of the data were taken with lower beam energies of 40 and 80 $A\cdot\text{GeV}$. Even lower energies, of 20 and 30 $A\cdot\text{GeV}$, were delivered in the year 2002. The analysis of these data is presently in progress.

NA49 has also taken data with beams of protons, pions, deuterons, carbon and silicon. These beams are obtained by fragmenting the primary beam from the accelerator (400 GeV protons or 158 $A\cdot\text{GeV}$ lead nuclei) in a target which is placed in the beam line,

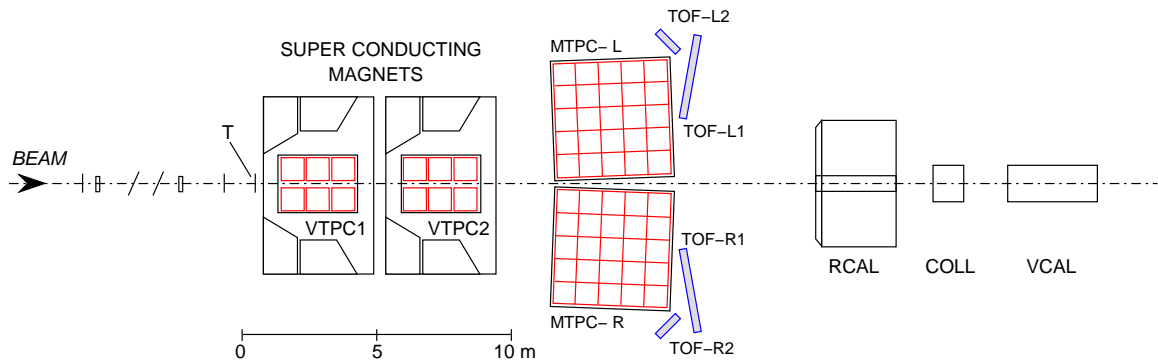


Figure 3.1: *Schematic overview of the NA49 experimental setup.*

between the accelerator and the experiment. Results obtained with these beams can be found in [37].

3.2 Detector overview

The NA49 experimental setup is shown in Figure 3.1 (top view) and Figure 3.2 (perspective view). The main detectors which are depicted in the figures are two main TPCs (MTPC-L and MTPC-R) and the two super-conducting magnets which contain the two vertex TPCs (VTPC-1 and VTPC-2). Both VTPCs consist of two separate sensitive volumes, which are positioned left and right of the beam. Two large time-of-flight (TOF) detector arrays provide additional information for particle identification in a restricted acceptance. In addition, there are several detectors in the beam-line to measure the beam position and composition. The veto calorimeter (VCAL), which is placed further downstream in the beam trajectory, is used for centrality selection. The different detectors are described in more detail in the next sections.

The ring calorimeter (RCAL), which is also shown in Figure 3.1, will not be discussed in this thesis. It has been used to measure transverse energy production at mid-rapidity in lead-lead interactions in a dedicated run [6]. Nowadays it is used to detect neutrons in proton-proton collisions.

The general NA49 coordinate system is indicated in Figure 3.2. The z -axis is along the beam direction. When looking downstream, the x -axis points to the left and the y -axis upwards. The origin of the coordinate system lies approximately on the beam trajectory, in the middle of VTPC-2.

3.3 Beam detectors and trigger

Before arriving at the target, the beam passes through three beam position detectors (BPDs), which are small wire chamber detectors at distances of up to 30 m upstream of the target. These detectors accurately determine the trajectory of each beam particle. The intersection point of the extrapolated beam trajectory with the target is used as

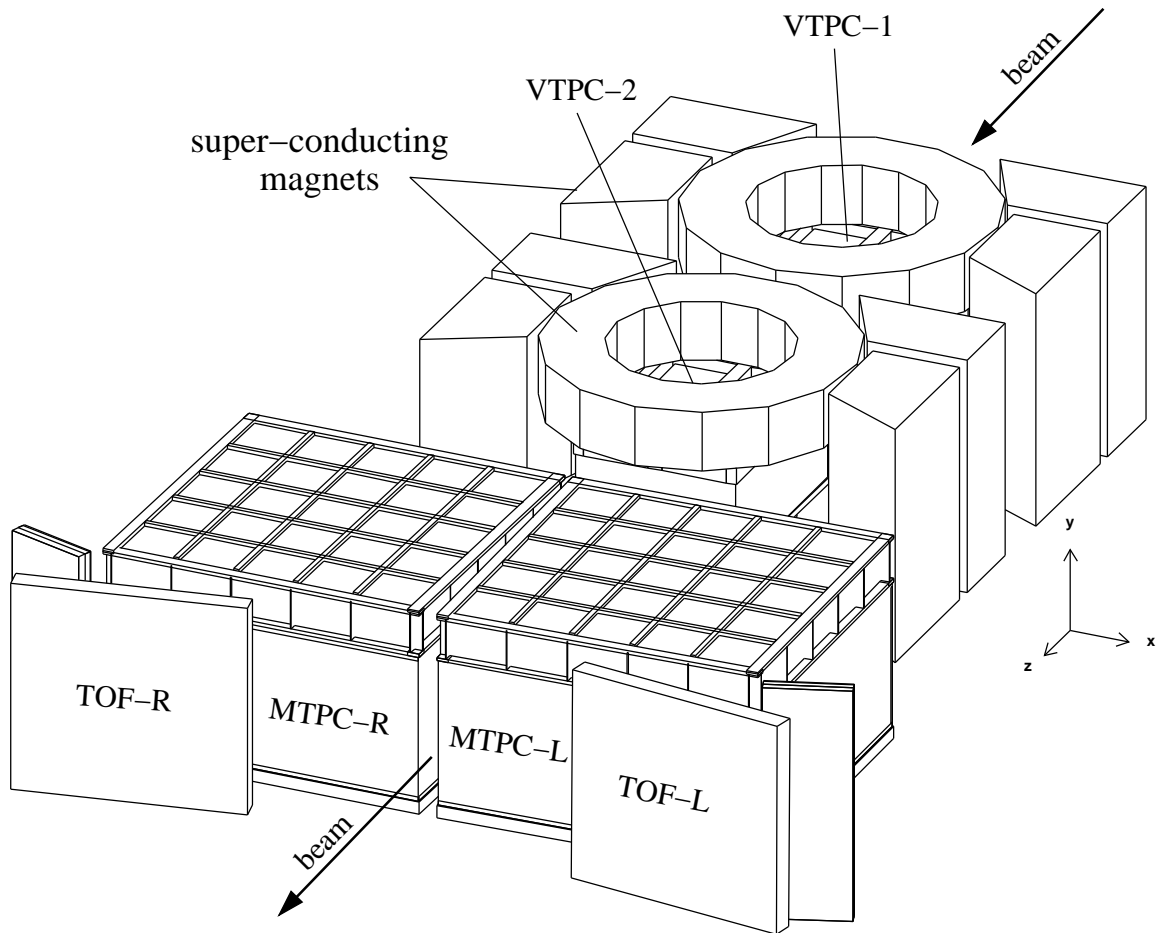


Figure 3.2: *Perspective view of the NA49 detector. Clearly visible are the TOF detectors, main TPCs and the super-conducting magnets around the vertex TPCs. The general NA49 coordinate system is also indicated.*

the primary event vertex in the reconstruction. The accuracy of the vertex position determination with these detectors is $40 \mu\text{m}$ [36].

The target is a lead foil of natural isotopic composition (52.4% ^{208}Pb). The target thickness is $200 \mu\text{m}$ (224 mg/cm^2), which corresponds to a 0.5% interaction probability for lead nuclei.

For trigger purposes, the presence of a beam particle is also detected by a helium gas Cherenkov counter which is placed in the beam upstream of the target (not shown). This detector has a charge resolution of a few times the elementary charge and is used to reject contamination of the beam with lighter nuclei. The interaction trigger requires an anti-coincidence of this detector with another gas Cherenkov detector placed behind the target. The beam detector also provides the start-signal for the time measurement in the TPCs. And additional quartz Cherenkov detector provides the start-signal for the time-of-flight measurement.

The energy measured in the veto calorimeter (VCAL) is used by the trigger system to select central events.

3.4 Veto calorimeter and centrality selection

The Veto Calorimeter is used to determine the centrality of the lead-lead collisions in the target. It is placed in the beam trajectory approximately 14 m downstream of the target and measures the total energy of the projectile spectators. These spectator particles are a mix of protons, neutrons and nuclei, with an energy per nucleon close to the beam energy. There is some intrinsic spread in the energies (several hundred MeV) due to the Fermi motion of the nucleons in the nucleus. Due to the magnetic field, the protons and neutrons are separated in space when entering the calorimeter. A collimator (COLL) is placed in front of the calorimeter to reject particles which are produced in the reaction by the participants. The aperture of the collimator is adjusted at each beam energy and magnetic field setting to accept most of the spectator particles. For very central events, there is a significant contamination of the calorimeter signal with particles produced by the participants in the interaction. A detailed study of this contamination and the centrality determination with the Veto Calorimeter is described in [38].

To illustrate that the energy measured in the Veto Calorimeter is indeed a measure of the centrality of the events, the relation between the Veto Calorimeter energy E_{veto} and the reconstructed track multiplicity for minimum bias 158 A·GeV Pb+Pb events is shown in Figure 3.3. There is a clear anti-correlation between both quantities. The (almost) linear dependence between the veto calorimeter signal and the event multiplicity suggests that both quantities are linearly dependent on the number of wounded nucleons.

The determination of the impact parameter b from the energy measured in the Veto Calorimeter requires the use of a model. As an example, the relation between the energy measured in the Veto Calorimeter E_{veto} and the impact parameter b as calculated using the VENUS event generator [17] is shown in Figure 3.4. The correlation between the impact parameter and the Veto Calorimeter energy is mainly determined by the Woods-Saxon nuclear density profile which is used in VENUS.

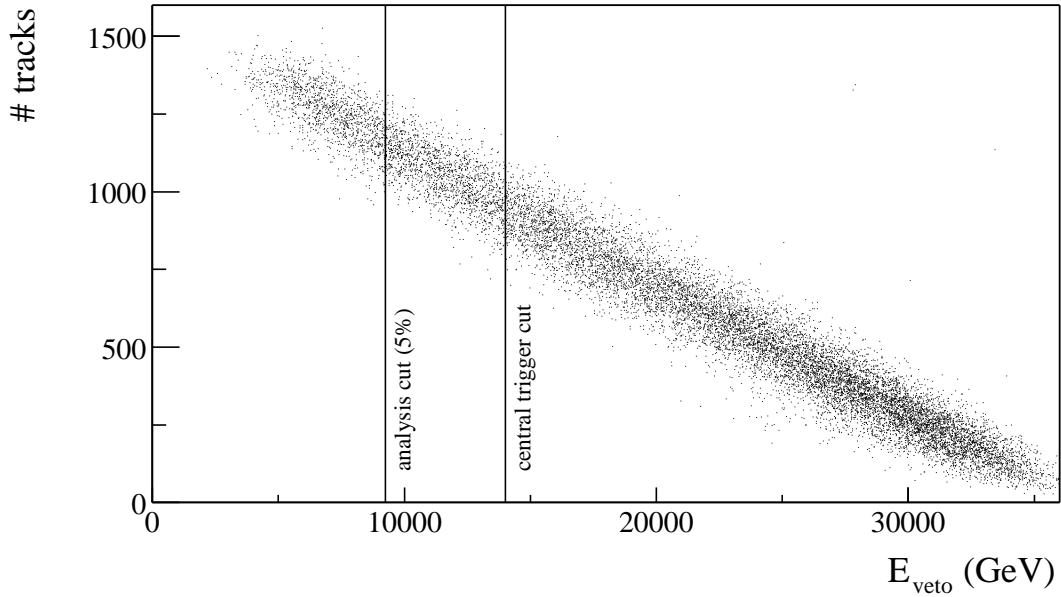


Figure 3.3: Correlation between event multiplicity and energy measured in the veto calorimeter for minimum bias Pb+Pb events at 158 A·GeV. Indicated are the on-line cut for the central trigger and the 5% cross-section cut used in the analysis.

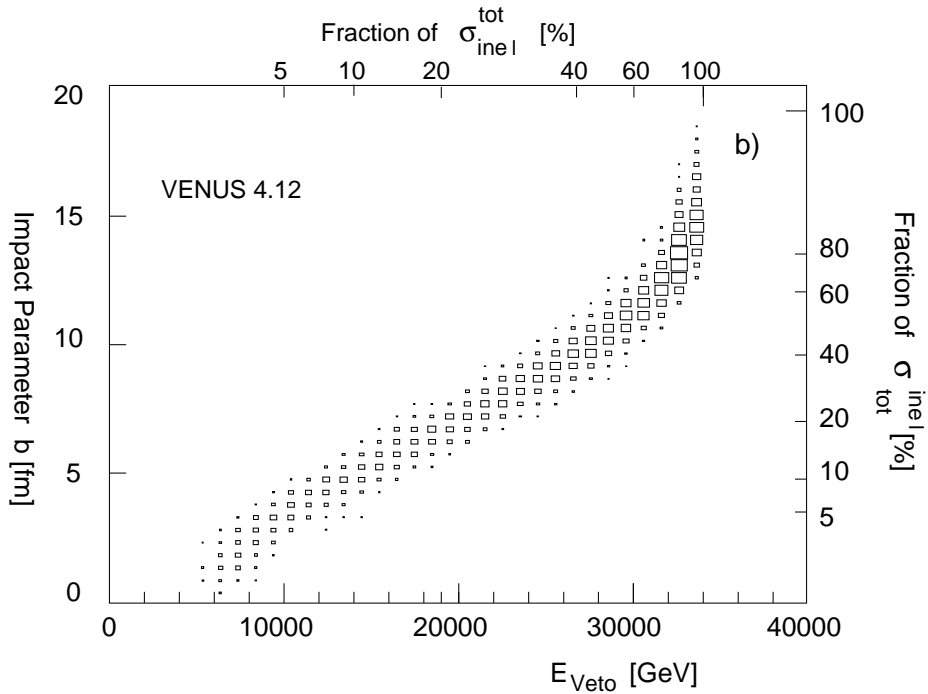


Figure 3.4: Correlation between the measured energy in the veto calorimeter E_{veto} and the impact parameter b as calculated in [36] using Venus 4.12.

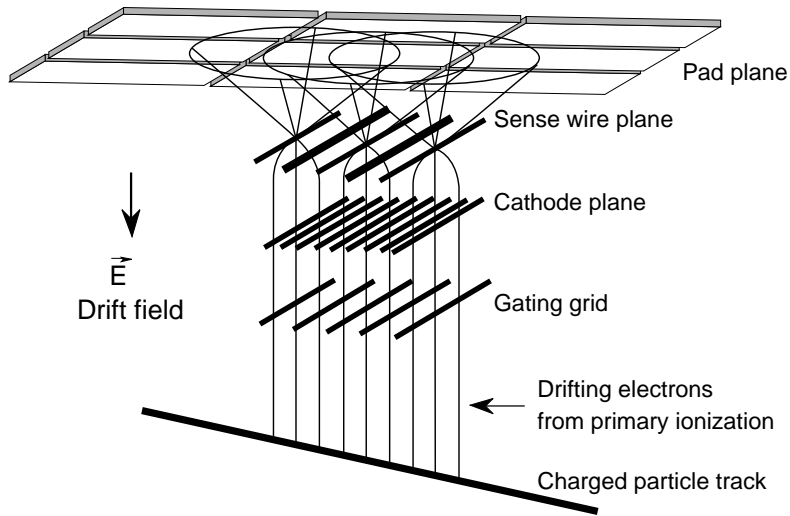


Figure 3.5: *Schematic drawing of the read-out chambers of the TPCs.*

3.5 Magnetic field

The magnetic field is produced by two super-conducting dipole magnets which have combined maximum bending power of 9 Tm. In the standard configuration, the field is directed downwards, bending positive particles to the $+x$ direction (left) and negatives to $-x$ (right). The magnetic field is homogeneous in the central parts of both vertex TPCs, but inhomogeneities at the edges of the vertex TPCs result in non-vertical orientations of the field lines. The strongest inhomogeneities are experienced by tracks which go through VTPC-1 and one of the MTPCs, since these pass through the second magnet far from its centre.

The magnetic field map which is used in the reconstruction was measured on a $4 \times 4 \times 4$ cm lattice using Hall probes before installation of the detector elements. The measured field agrees with results from detailed magnetic field calculations to within 0.5% [36]. The calculated map is used to extend the field map into unmeasured regions.

To maintain a constant magnetic field throughout each data-taking period, the current in the magnets is kept stable to approximately 0.01%. In addition, the field is monitored by Hall-probe measurements, which also indicate that the field is stable to 0.01%.

At 158 A·GeV beam energy the magnetic field is set to 1.5 T in the magnet surrounding VTPC-1 and to 1.1 T in the VTPC-2 magnet. At lower beam energies, the magnetic field is scaled down proportional to the energy, to ensure a comparable acceptance of tracks at the different energies. Because the field map was not measured at the lower energies, the field was calibrated using the reconstructed masses of the Λ and K_s^0 to a precision of better than 1%.

3.6 Time projection chambers

The four Time Projection Chambers (TPCs) provide a momentum measurement through particle tracking and a measurement of the ionisation energy loss for particle identification. The two VTTPCs, which have a gas volume of $200 \times 250 \times 67$ cm each, provide tracking information throughout the magnetic volume of the experiment. The MTTPCs are much larger ($390 \times 390 \times 112$ cm) and provide most of the sensitivity for the ionisation energy loss measurement in the relativistic rise.

The most important constraint in the design of the TPCs is the large number of tracks in central lead-lead events. The very high track density of up to 0.6 particles per cm^2 requires a design which is optimised for two-track separation. This was achieved by selecting a drift-gas and a design of the read-out planes which minimise the width of the measured charge clusters. In addition, a minimum amount of material surrounds the active volume of the detectors, to minimise the production of secondary particles in the detector material.

The detectors consist of a top plate supporting the read-out planes, the electronics, and the frames for the field cage and the surrounding gas box. The gas box consists of two layers of mylar foil supported by a fibreglass-epoxy frame. The space between the two foils is flushed with nitrogen to minimise contaminations of the detector gas. The field cage, which provides the uniform drift field inside the gas envelope is made of strips of aluminised mylar foil which are supported by ceramic rods at the corners. Each VTTPC contains two separate field cages, left and right of the beam. The highly-charged lead ions do not pass through the sensitive volume of the detector.

The detector gases have been selected for their low charge diffusion coefficients, providing narrow cluster charge distributions at the read-out plane. The gas of choice for the VTTPCs is a mixture of 90% Ne and 10% CO_2 , while for the MTTPCs a mixture of 90% Ar, 5% CH_4 and 5% CO_2 has been used. Drift fields of 200 V/m (175 V/m) in the vertex (main) TPCs result in a drift velocity of 1.4 cm/ μs (2.4 cm/ μs) and charge distributions with a 5 mm FWHM in all TPCs. The drift velocities are such that the maximum drift times in the VTTPC and MTTPC are approximately equal.

The read-out planes, depicted in Figure 3.5, are mounted on the support plate at the top of the TPCs. The drifting charge is amplified in a proportional chamber which is formed by the cathode wires, the pad-plane and the sense-wires. The gating grid only allows the drifting charges to reach the read-out chambers when a trigger was received. The distance between the sense-wires and the pads was kept relatively small (down to 2 mm) to ensure narrow induced charge distributions on the pads. Due to the high track density, it is necessary to read out all the pads, instead of the more customary wire read-out.

The pad read-out is organised in sectors, which each have separate sets of wires. Each sector contains several rows of pads, which are parallel to the entrance window of the TPCs. The distance between the rows of pads is typically 2.8 cm in the VTTPCs and 3.95 cm in the MTTPCs. Each row contains 128 or 192 pads, depending on the expected track density, with a width between 3.5 and 5.45 mm. To ensure optimum two-track separation, the pads are tilted to be aligned to the tracks passing over them. The tilt angles vary between 0 and 55 degrees, with the largest angles in VTTPC-1. The width of the pads is such that each track leaves a signal in more than one pad. The resulting space

point resolution is of the order of a few hundred microns in the direction perpendicular to the track. The total number of pads in the TPCs is slightly over 182 000.

The TPCs operate in the regime where the drift velocity and gas gain are strongly dependent on the temperature and pressure. In order to minimise temperature variations, the TPCs are placed inside a thermally insulated room, where the temperature is stabilised to better than 0.1 °C. The temperature and air pressure are continuously monitored and the measured values are used to calculate the drift velocity for the reconstruction. An independent measurement of the drift velocity has shown that the precision of the calculated drift velocity is better than 0.1% [36].

The charge signal on each pad is first fed through an amplifier and shaper and then stored in an analog memory which samples the signal each 100 ns and holds 512 samples per event. These electronics are mounted on the TPC, together with the 8-bit analog-to-digital converter (ADC) which digitises the charge measurement. The half-time of the shaper is such that each track occupies a number of time samples, for an accurate determination of the position in the drift direction. The electronics on the TPC could be reconfigured to only digitise every second sample in the analog memory. This option has been used to reduce the event size and increase the event rate during the data-taking period in the year 2000 when large statistics were accumulated to measure rare signals such as charm production.

3.7 TOF detectors

The experimental setup includes time-of-flight (TOF) detectors to extend the particle identification capabilities at low momenta. There are several sets of TOF detectors in the experiment, but only the two main TOF arrays which are indicated by TOF-L1 and TOF-R1 in Figure 3.1 are used in the analysis presented in this thesis. Each of the two TOF arrays contains about 1000 scintillator detectors which are read out by two photomultiplier tubes each. The detector measures the arrival time of particles at the wall relative to a start-counter which measures the passage of the beam particle. The time-of-flight measurement has a resolution of approximately 60 ps. The total deposited charge is also measured to distinguish double hits. The measured hits are assigned to the closest track measured in the main TPCs. The acceptance of the TOF detector is limited to mid-rapidity for kaons at the three different beam energies.

3.8 Data acquisition and event rates

The data taking rate is determined by a number of factors. First of all, the spill structure of the SPS accelerator. The SPS delivers spills of 5 s for 158 A·GeV lead beams. The time between spills is 10–15 s depending on the exact configuration of the accelerator complex. During each spill some 150k lead ions pass through the target. The total interaction probability in the target of 0.5% and the centrality trigger at 10% of the total cross section provide about 75 potential triggers per spill. Increasing the beam intensity to beyond 300k per spill leads to a large contamination of events by δ -electrons which are produced by the beam when it passes through the gas volumes in the experiment. The probability to have two interactions in the target during the drift time also increases

with beam intensity. The TPC electronics take about 60 ms to digitise a single event and transfer it to the receiver boards, where it is stored. This amounts to a maximum of 80 events per spill. Both effects together, the maximum number of triggers delivered by the beam and the maximum acceptable number of events due to dead-time, result in 40–60 usable events per spill.

The receiver boards in the counting-house have buffers which can hold 32 raw events. The input buffers are read out by a digital signal processor (DSP) which applies a zero suppression algorithm. The buffers are not accessible for the DSP when data is transferred from the TPC electronics. As a result, the number of events which are treated by the DSP and sent to tape during the spill is limited and most of the processing of the events takes place in the 10–15 second period between spills. For normal central lead-lead data taking the resulting data rate is 28–30 events per spill. This number increases with decreasing event size and/or increasing spill length.

During the year 2000 data-taking period, the detector was operated with 256 time sample read-out to decrease the event size, and increase the event rates to accumulate as many events as possible to study rare observables. The electronics on the detector were reconfigured to only digitise and send every second time sample to the receiver boards. This reduces the dead-time of the TPC read-out by a factor of two. Moreover, the reduction of the total raw event size by a factor of two allowed to configure the input buffers on the receiver boards to store a maximum of 64 events per spill. In order to furthermore reduce the data stream to the tape, a compression algorithm was programmed into the DSPs, reducing the event size from 8 to 3 Mb. In order to saturate the data-acquisition in this configuration, the beam intensity was slightly increased, the target thickness was increased to 300 μm and the centrality trigger was set to approximately 20%. The total result of these measures is to increase the event rate to 48 events per spill. The main reasons for not reaching the maximum of 64 events per spill are the transfer speeds between the receiver boards and the tape drive and the dead-times of other detector systems, which vary between 30 and 50 ms.

3.9 Data samples

The data samples which are used in the analyses were collected over the course of several years (1996–2000).

For the measurement of the energy dependence of kaon production, data were taken at 40, 80 and 158 $A\cdot\text{GeV}$. The target thickness was 200 μm , leading to an interaction probability of 0.5% for a lead nucleus. The on-line centrality trigger was set at 7.2% of the total inelastic cross section for the 40 and 80 $A\cdot\text{GeV}$ data and 10% for the 158 $A\cdot\text{GeV}$ data sample. At each energy, 200–400k events were used for the analysis. At 40 and 158 $A\cdot\text{GeV}$ additional data samples were taken with reversed magnetic field polarity. These data samples also consist of 200–400k events and were partly analysed to check for systematic errors.

In 2002 a large sample of 3 million central Pb+Pb events was collected to study rare observables such as open charm production. The running conditions were adapted to maximise the number of events, as described in Section 3.8.

Chapter 4

Reconstruction procedure

The reconstruction software performs the task of track recognition, momentum determination by track fitting, the calculation of the ionisation energy loss dE/dx and the calculation of the particle masses from the time-of-flight measurements. The different steps in the reconstruction procedure are described in the following sections.

4.1 Track reconstruction

The three main steps in the track reconstruction are cluster finding, track finding and track fitting. A description of the procedures implemented in the reconstruction software is given in the next sections. As an example, a typical reconstructed lead-lead event is shown in Figure 4.1. The figure shows all points and the reconstructed particle trajectories for a thin horizontal slice through the event.

4.1.1 Cluster finding

The first step in the reconstruction is the cluster finding. Signals in adjacent pads and time slices are collected into clusters. The cluster finder requires that the cluster is not too elongated in the pad or the time direction and has the maximum measured charge close to its geometrical centre. These requirements are imposed to suppress noise. In the vertex TPCs, where the track density is higher, merged clusters, i.e. clusters with two distinct maxima, are identified and split in two by the clustering algorithm. For each cluster the average time and pad position is calculated. These coordinates define the points which are used by the tracking algorithm. The position of the points in space is calculated using the known geometry and the pressure and temperature dependent drift velocity. The total deposited charge is also calculated for each point and used for the dE/dx measurement.

The main force exerted on the drifting electrons is due to the uniform electric drift field, which makes them drift upwards in the TPC. When the magnetic and electric field lines are not completely parallel, however, the force on the drifting electrons will not be completely vertical. This leads to deflections of the drifting clusters, most notably at the edges of the VTPC where the magnetic field is not uniform and close to the sense-wires where the electric field is not uniform. The measured cluster positions are corrected for these deflections.

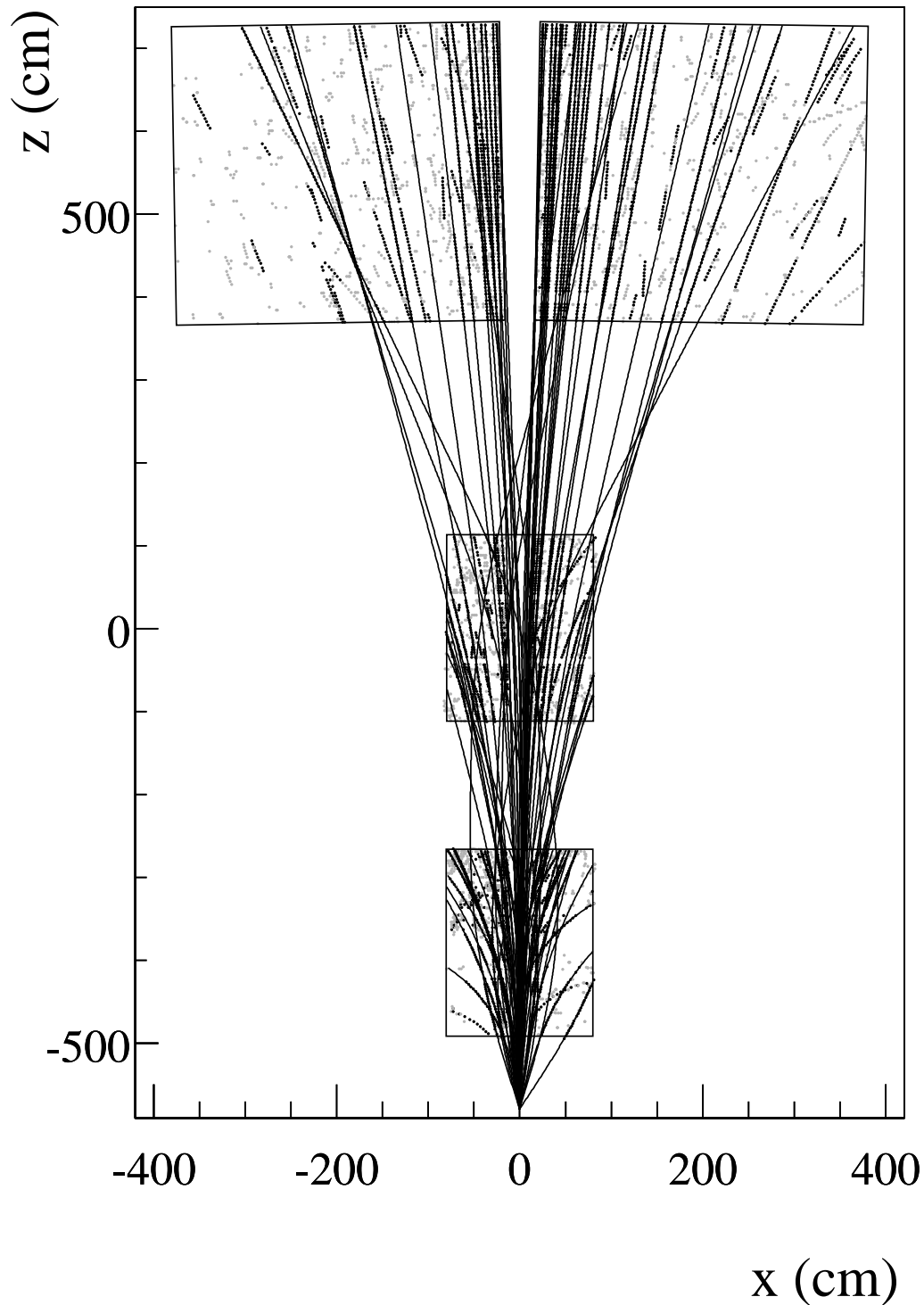


Figure 4.1: A horizontal slice through a single central lead-lead event, in all TPCs. All clusters within 1 cm from the horizontal plane at $y = 0$ are shown for the vertex TPCs. For the main TPCs the range is ± 2 cm from the central plane. Grey points indicate clusters which are not assigned to tracks, mostly noise. The lines indicate the trajectories of tracks fitted to the main vertex.

After these corrections, it was found that the points still systematically deviate from the ideal track trajectories. These deviations are generally small, of the order of $100\ \mu\text{m}$, but can reach values of up to $500\ \mu\text{m}$ at the edges of the sectors. The deviations are probably due to the imperfect correction for the deflection of the clusters due to the non-uniform fields and possibly some additional effects due to truncation of the clusters close to sector edges. A correction is determined from the observed deviations in the data and applied in the reconstruction.

4.1.2 Tracking

The next step in the track reconstruction is the pattern recognition to find the trajectories of the particles. The tracking algorithm is organised in several steps, starting with the simplest track geometries, removing the points from the list of available points, and ending with the more complicated geometries which are easier to recognise in the remaining set of points. The first step is therefore to find tracks in the MTPCs, where the track density is relatively low and the tracks are straight.

The tracks from the MTPC are extrapolated to the target plane, using the magnetic field map. Points in VTPC-2 which are close to the extrapolated track trajectory are assigned to the track, provided the extrapolated track trajectory is close enough to the main vertex. MTPC tracks with no corresponding track segment in VTPC-2 are released for use in later stages of the tracking.

The remaining points in VTPC-2 are used to form tracks in this TPC only. These tracks are extrapolated to the main TPC and points are assigned if found. All MTPC and VTPC-2 tracks are then extrapolated to the main vertex and points in VTPC-1 along the extrapolated trajectories are collected. Again, if points are expected in VTPC-1 and none are found, the clusters on the MTPC track are released.

The remaining clusters in VTPC-1 are used for tracking in this TPC and the found tracks are extrapolated to collect points in the MTPC. The final step of the tracking procedure is to find all remaining tracks in the MTPCs, including tracks of particles which have a kink in their trajectory due to a decay.

4.1.3 Track fitting

All found track trajectories are fitted to determine the momentum. The momenta which are used in the analyses are determined assuming that each track starts from the main vertex, which is accurately determined by the beam position detectors and the known z -coordinate of the target. In Figure 4.1 a small sample of the resulting tracks for a single event, with points within 1 (in the VTPC) or 2 cm (in the MTPC) above or below the beam trajectory are shown. The thickness of this slice corresponds to approximately 16 time slices.

The reconstruction software also recognises tracks which do not come from the main vertex, such as those from weak decays of strange particles. A fraction of the tracks in the main TPC also results from conversions of photons and from hadronic interactions in the detector material (mainly in the ceramic rods at the exit planes of the VTPCs).

Each track is also fitted without assuming that it comes from the main vertex. The distances in the horizontal x -direction and vertical y -direction between the extrapolation

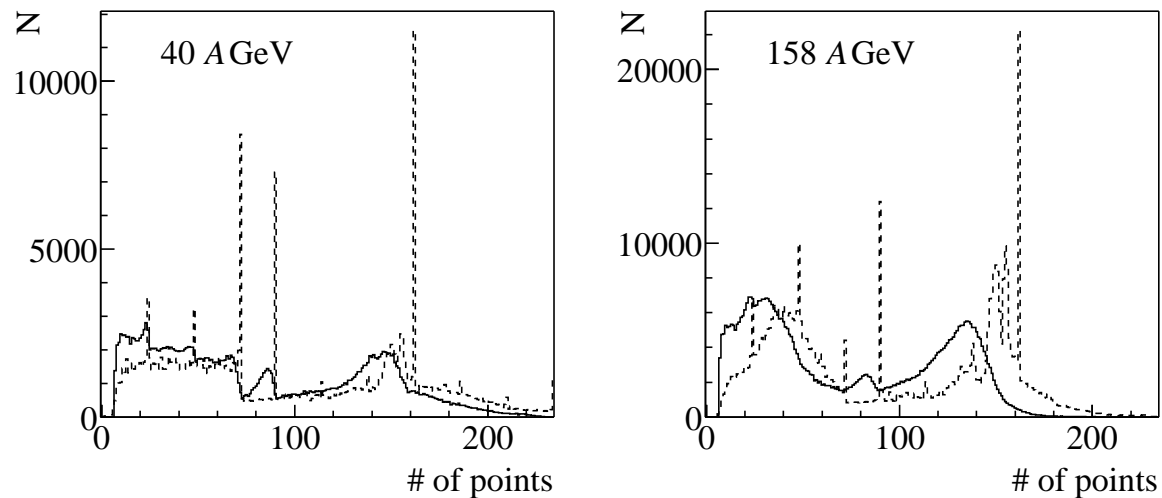


Figure 4.2: *Distribution of the number of points on reconstructed tracks (full histograms) and the maximum number of points (dashed histograms) on each track for central 40 A·GeV data on the left and 158 A·GeV data in the right panel.*

of the track to the target and the position of the main vertex are the so-called track impact parameters b_x and b_y . The overall resolution on those parameters is of the order of a few millimeters, which is not accurate enough to identify secondary vertices from decays of charmed particles. The impact parameter determination can in principle be used to reject tracks which originate from weak decays of strange particles, but this requires a detailed treatment of the dependence of the impact parameter resolution on the track topology. Since the expected fraction of kaons originating from such decays is very small, such a cut was not applied in the analysis.

In Figure 4.2 the distribution of the number of points on reconstructed tracks (full line) is compared to the distribution of the potential number of points on each track (dashed line). The potential number of points is calculated for each track during the reconstruction, using the fitted track trajectory and the detector geometry. The distribution of the number of potential points has sharp peaks at 72, 90, and 162 points. This corresponds to tracks traversing only VTPC-1 (72 points), only MTPC (90 points) and tracks going through VTPC-2 and MTPC (162 points). Only a small fraction of tracks traverse all three TPCs and have a maximum of 234 points.

From Figure 4.2 it is seen that in central collisions at 158 A·GeV most reconstructed tracks have less points than the expected number, due to the high occupation of the detector. This effect is less pronounced at 40 A·GeV.

4.2 Ionisation energy loss measurement

The ionisation energy loss per unit length traveled in the detector gas (dE/dx) depends on the velocity of the particle rather than the momentum and therefore provides an indirect measurement of the particle mass. The relation between the average ionisation energy

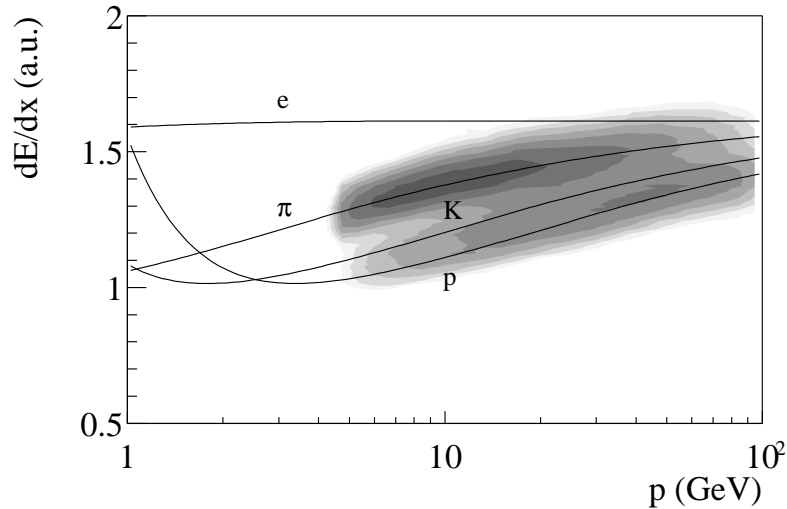


Figure 4.3: Ionisation energy loss versus total momentum for positive tracks with more than 30 points in 158 A·GeV central events.

loss $\langle dE/dx \rangle$ and the velocity $\beta = v/c$ of a particle is given by

$$\left\langle \frac{dE}{dx} \right\rangle = \frac{4\pi N e^4}{m_e \beta^2} \left[\ln \frac{2m_e \beta^2}{I(1-\beta^2)} - \beta^2 - \delta(\beta) \right], \quad (4.1)$$

where e is the charge of the electron, m_e its mass, N is the number density of electrons in the detector gas and I the mean excitation potential. The first two terms are the original Bethe-Bloch formula [39]. The first term, however, goes to infinity when $\beta \rightarrow 1$, which is not observed in reality. The reduction of the ionisation at large velocities, due to coherent polarisation of the surrounding atoms which shields the field of the traversing particle, is parametrised by the function δ [40]:

$$\delta = \begin{cases} 0 & \beta\gamma < a_1 \\ 2(\ln \beta\gamma - b) + c(\ln a_2 - \ln \beta\gamma)^d & a_1 < \beta\gamma < a_2 \\ 2(\ln \beta\gamma - b) & \beta\gamma > a_2 \end{cases} \quad (4.2)$$

The parameters b , c and d in this equation are tabulated for many materials, but will be fitted to the data in our case. The values of a_1 and a_2 are calculated to make δ a continuous function of β .

The measured ionisation energy loss for central 158 A·GeV lead-lead events is shown in Figure 4.3. Also shown is a fit of Eq. 4.1 to the data. Because most of the measured tracks are in the ‘relativistic rise’ region ($p \gtrsim 10$ GeV) where the ionisation energy loss of kaons, pions and protons are relatively close together it is very important to achieve the best possible resolution on the dE/dx measurement by applying a number of corrections and performing accurate calibrations.

4.2.1 Corrections and calibrations

A brief description of the corrections which are applied to the measured cluster charges in the reconstruction software is presented in the next paragraphs. A more extensive

discussion can be found in [41].

Pad gain calibration

The TPCs are calibrated pad-by-pad using radioactive ^{83}Kr which is injected in the detector gas during dedicated calibration runs (without beam). This method was developed by the ALEPH collaboration [42]. The Krypton isotope has a half life of 1.9 h and emits a well-known spectrum of electrons with energies up to 41.6 keV. The pad gain is determined for each pad separately to obtain a uniform response to this signal.

Since the krypton calibration is done with different voltages on the sense wires of the readout chambers than the actual data taking, an additional calibration constant is determined for each sector individually. These constants are adjusted such that the measured dE/dx for pions follows the Bethe Bloch formula (Eq. 4.1) with a fixed set of parameters.

Hardware corrections

Each measured cluster gives rise to a pattern of undershoots and overshoots and a baseline drop due to the electronics response and the late arrival of the ions at the bottom plate of the TPC. For high track densities, such as in 158 A·GeV central collisions, this leads to a significant dependence of the measured dE/dx signal on the local track-density. In addition there are cross-talk effects on the read-out. These effects were determined using laser tracks [41] and the resulting response functions are used to correct the measured charge.

Threshold correction

To suppress noise in the TPCs and to reduce the data volume written to tape, a threshold cut of 5 ADC counts is applied to the digitised data.¹ The threshold does not only suppress noise, but it also removes the tails of the charge clusters. The resulting charge loss depends on the total measured charge and the shape of the clusters, which is determined by the angles of the track with respect to the pads. The width of the clusters also depends on the vertical coordinate in the TPC due to diffusion effects. To correct for the losses, the measured clusters are fitted with a cluster shape which is a product of a Gaussian in the time direction and a Gaussian in the direction along the pad-row. The widths of the fitted Gaussians are calculated from the track angles and the y -coordinate as described in [41]. In this way, the only free parameter in the fit is the total charge of the cluster.

The procedure is adequate for the main TPCs, where the angles between the tracks and the pads are relatively small, and the cluster shape is well described as a product of two Gaussians. In the vertex TPCs, the angles between the tracks and the pads can be large, leading to broad clusters, with a non-Gaussian shape. The correction using the cluster fit was therefore only applied in the main TPCs and no correction is applied in the vertex TPCs.

For the data taken with the reduced sampling frequency (256 instead of 512 time slices), the number of measured charges is reduced by about a factor of two, which makes

¹In fact a simple filtering algorithm is applied, but the details are not essential here.

it more difficult to apply the Gaussian fit to these data. Instead, the average charge loss was determined by a simple simulation of the effect of the threshold on the measured charge. The cluster shape in this simulation was based on a sum of three Gaussians in both the time and pad direction, which include the effect of the undershoot immediately after the cluster arrives at the read-out plane. The product of both sets of three Gaussians represents the cluster shape in a very thin slice of the detector. Due to the finite length of the read-out pads, the cluster is smeared out. The final shape therefore depends on the angles of the cluster with respect to the read-out plane and the depth in the TPC (due to diffusion effects). The charge loss due to the threshold cut was calculated using this shape for a number of different track angles and y -coordinates and the result was stored in a lookup table. This table is then used to correct the measured cluster charges for the charge loss due to the ADC threshold in all TPCs. The development of this procedure for application in events recorded with proton and pion beams, where the hardware corrections are not applied, is described in [43]. The procedure was adapted for use in the nucleus-nucleus data with the 256 time slice read-out including the hardware corrections.

Drift length dependence

The measured total cluster charge after corrections still depends on the distance between the track and the read-out plane. This is partly due to capture of electrons by the detector gas (approximately 2% charge loss per metre [41]). The combined effect of broadening of the clusters due to diffusion and the ADC threshold also gives rise to a drift-length dependent charge loss. The y -dependence of the cluster charges in the data is used to determine the charge loss per unit drift length and the cluster charges are corrected for this effect.

4.2.2 Truncated mean calculation

The cluster charge distribution in a main TPC sector along a track is shown in Fig. 4.4 for tracks with momenta between 10 and 11 GeV. The distribution contains charge measurements from different types of particles, but most of the tracks (about 90%) are pions. The distribution of cluster charges has a long tail to high charge losses. This is an intrinsic property of the ionisation process, as has been calculated by Landau [44]. In order to reduce the tail of the distribution of average track dE/dx , a truncated mean is calculated from the lowest 65% of the cluster charges. To illustrate the effect of this procedure, tracks were generated with 80 charge measurements, distributed according to Figure 4.4. The resulting distributions of the mean and truncated mean charge per track are shown in Figure 4.5. The distributions are fitted with an asymmetric Gaussian:

$$f(x; C, x_0, \sigma, \delta) = \begin{cases} \frac{C}{\sigma\sqrt{2\pi}} \exp -\frac{1}{2} \left(\frac{x - x_0}{(1 + \delta)\sigma} \right)^2 & \text{for } x \geq x_0 \\ \frac{C}{\sigma\sqrt{2\pi}} \exp -\frac{1}{2} \left(\frac{x - x_0}{(1 - \delta)\sigma} \right)^2 & \text{for } x < x_0 \end{cases}. \quad (4.3)$$

The asymmetry parameter δ determines the difference between the width of the right half and left halves of the Gaussian. The relative width $\sigma_{rel} = \sigma/x_0$ is much smaller for

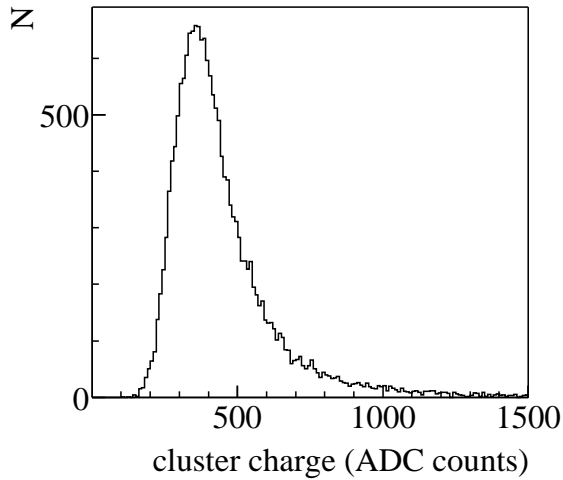


Figure 4.4: *Measured distribution of cluster charges for tracks between 10 and 11 GeV.*

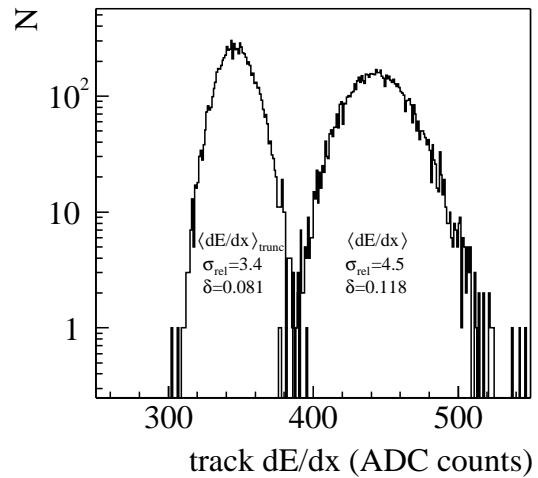


Figure 4.5: *Distributions of mean charge and truncated mean charge as produced using the distribution in the left panel, for tracks of 80 hits.*

the truncated mean than for the mean of all measured charges. The asymmetry δ is also smaller for the truncated mean.

4.2.3 Global dE/dx

Most NA49 analyses using dE/dx for particle identification are based on the measurement of the ionisation energy loss in the MTPC only. The reason is that the dE/dx measurement in the MTPC is superior, because of the 4 m track-length, compared to the 2 m in the VTPC. As a result, the MTPC performance is well-studied and the corrections are optimised for performance in the MTPCs.

To further optimise the dE/dx resolution, it is possible to combine the measurements in the different TPCs to a single dE/dx value for each track. The dependence of the ionisation energy loss on the particle momentum, however, is different in the main and vertex TPCs, due to the different gas-composition. To combine the measurements in the different TPCs, the measured dE/dx in the VTPC is therefore scaled to be comparable to the MTPC dE/dx , using the ratio of the parametrised dE/dx (using Eq. 4.1) in the vertex and main TPCs. The weighted average of the measurements in the different TPCs is used as the global dE/dx .

Global dE/dx (MTPC and VTPC combined) has not often been used in NA49 because important corrections, such as the threshold correction, were not routinely applied for the VTPCs. A more uniform treatment of the dE/dx measurements in all TPCs was introduced along with the modifications of the reconstruction software for the 256 time slice data. The procedure includes the removal of points close to track crossings from the dE/dx calculation, which is especially important in the high track density environment of the VTPCs. The effect of these modifications on the dE/dx measurements in the MTPCs, VTPCs, and the global dE/dx is further illustrated in Section 7.3.1.

Chapter 5

Kaon spectra at 40, 80 and 158 $A\cdot\text{GeV}$

In this chapter the measurement of kaon production in central lead-lead collisions at 40, 80 and 158 $A\cdot\text{GeV}$ will be presented. At SPS energies, kaons are the dominant carriers of (anti-)strange quarks in the final state of nuclear collisions. As discussed in Chapter 2, the production of strangeness is expected to be influenced by the formation of a QGP in the early stage of the collision. The measured energy dependence of strangeness production will test our understanding of strangeness production and might show signs of the onset of deconfinement with increasing beam energy.

The analysis presented here uses the measured ionisation energy loss dE/dx of the tracks in the main TPCs to identify kaons. For this purpose, the tracks are divided in bins of total and transverse momentum and the kaon yield is obtained in each bin from a fit to the dE/dx distribution. These yields are then corrected for acceptance and efficiency. The total yields of kaons are calculated by integrating the measured momentum distributions and applying a relatively small extrapolation to unmeasured regions.

The procedure for obtaining the spectra and the total yields, including the fits to the dE/dx distributions and the corrections for acceptance and efficiency are described in this chapter. A comparison of the results with the different models described in Chapter 2 is presented in Chapter 6.

5.1 Event cuts

For a small fraction of events (less than 1%) it is not possible to properly determine the main vertex position, mainly due to noise in the beam position detectors, or a problem with the raw event information. These events were rejected from the analysis. The reconstruction software also performs a vertex fit using the reconstructed tracks and the beam trajectory as measured by the beam position detectors. The vertex position as determined in this way is used to identify events which have the main vertex outside the target (beam-gas interactions). The contamination of the central event sample with these non-target events is found to be negligible (below 0.1%).

For the 158 $A\cdot\text{GeV}$ data sample an additional cut on the energy measured in the Veto Calorimeter was applied to select the 5% most central events (approximately half of the total central event sample at this energy).

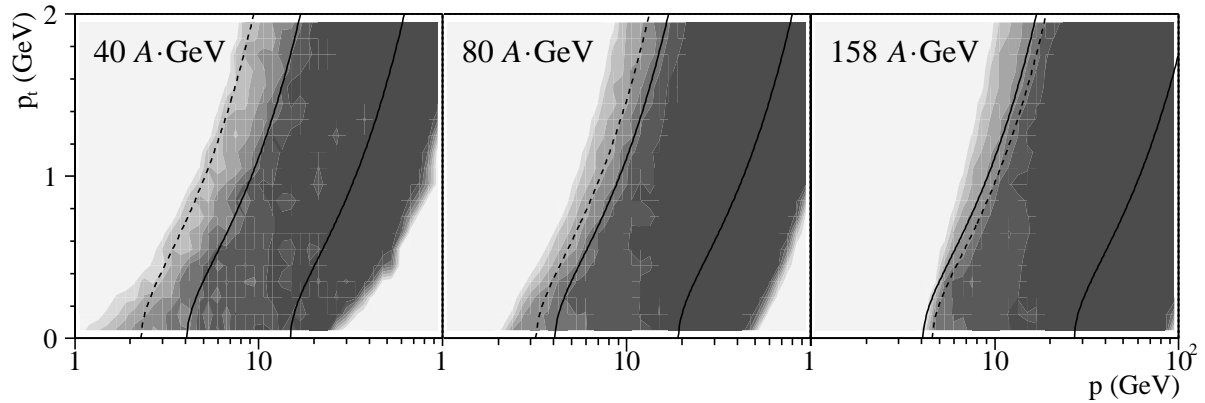


Figure 5.1: *Geometrical acceptance after analysis cuts for the three analysed energies. Also included are losses due to in-flight decay of kaons. The acceptance scale is color-coded using eight different grey levels, ranging between 0 and 10% acceptance. The dashed line indicates mid-rapidity for kaons at each energy and the full lines indicate the lowest and highest rapidity used in the analysis.*

5.2 Track cuts

The main motivation for selecting the track cuts is not to maximise the acceptance but to optimise the track finding efficiency and the dE/dx resolution. The cuts used in the analysis are therefore:

- Each track must have at least 50 potential points in the main TPC. This excludes short tracks which go through a corner of the detector.
- Tracks were required to have at least 50% of their potential points found in the MTPC. This cut removes possible noise tracks and kaons which decay before traversing half the MTPC.
- Tracks which have more than 10 potential points in one of the VTPCs must have some points found in these TPCs. This cut removes tracks resulting from photon conversions in the detector material upstream of the main TPCs.
- Only ‘right-side’ tracks which leave the main vertex at an azimuthal angle ϕ of less than 30° with the horizontal plane have been used. These right-side tracks are tracks which leave the primary vertex in the direction in which they are bent by the magnetic field (for the normal magnetic field this means $p_x > 0$ for positive tracks $p_x < 0$ for negatives). The TPCs are designed to have the pads approximately parallel to the trajectories of these tracks, resulting in relatively narrow clusters and small threshold corrections. Furthermore, the cut on ϕ excludes most of the tracks which leave the detector at the top and bottom planes.

The acceptance after application of these cuts is shown in Figure 5.1. The figure shows the accepted fraction of tracks in each bin, including losses due to in-flight kaon decay. The acceptance was determined using a Monte Carlo simulation with an accurate

description of the detector geometry, as further described in Section 5.5. The dashed lines in the figure indicate mid-rapidity for kaons at each energy. The full lines indicate the region in which the analysis was performed. The lower boundary for this region is set at $y = 2.9$ for all three energies. At lower rapidities the number of kaons cannot be accurately determined using the dE/dx measurement, because the difference in energy loss of pions, kaons and protons becomes small (see Figure 4.3). For this same reason, no reliable results could be obtained for $y > 4.7$. At 40 and 80 $A\cdot\text{GeV}$, the highest rapidity value for the analysis is limited by statistics.

The geometrical acceptance is mainly determined by the requirement to have 50 or more potential points in the MTPC. Low momentum tracks do not reach the MTPC, because their trajectories in the magnetic field are strongly curved, while most very high momentum particles escape along the beam-line, undetected by the two MTPCs. An additional reduction of the acceptance by up to 30% is seen in Figure 5.1 at low momenta due to in-flight decay of the kaons.

5.3 Combined TOF- dE/dx measurement

In part of the detector acceptance (close to mid-rapidity), both the energy loss and the time-of-flight (TOF) are measured to identify particles. In Figure 5.2, the two-dimensional TOF- dE/dx distribution and projections on the TOF and dE/dx axes are shown for tracks with momenta close to mid-rapidity ($0.85 < \log_{10} p/\text{GeV} < 0.90$) and $0.4 < p_t < 0.5$ GeV. It is clearly impossible to separate kaons and protons using only dE/dx or TOF information. The combined measurement does allow this separation and was used to determine the width of the proton and pion dE/dx distributions separately.

The relation between the position and width of the dE/dx peaks was parametrised as

$$\sigma_i = \sigma x_i^\alpha, \quad (5.1)$$

where σ_i is the width of the peak of particle species i and x_i the position of the peak. The value of the scaling parameter α for NA49 is determined by fitting the two-dimensional TOF- dE/dx distributions with a product of Gaussians in m^2 and asymmetric Gaussians of Eq. 4.3 in dE/dx , assuming scaling of the widths according to Eq. 5.1. The results on α of these fits for 40, 80 and 158 $A\cdot\text{GeV}$ data are shown in Figure 5.3. There is no indication that α depends on momentum, transverse momentum, or beam energy. For the analysis, $\alpha = 0.625$ was used and the sensitivity to changes in α of ± 0.125 (dashed lines in Figure 5.3) is described in Section 5.7.

5.4 Spectra analysis

The data were divided in bins of the logarithm of total and transverse momentum, as shown in Figure 5.1. In each bin the dE/dx distribution was fitted to obtain the yields of the different particle species (protons, kaons, pions and electrons). These measured values were corrected for acceptance, decays and efficiency, as described in the next section. An interpolation procedure is used to determine the yields as a function of transverse momentum and rapidity.

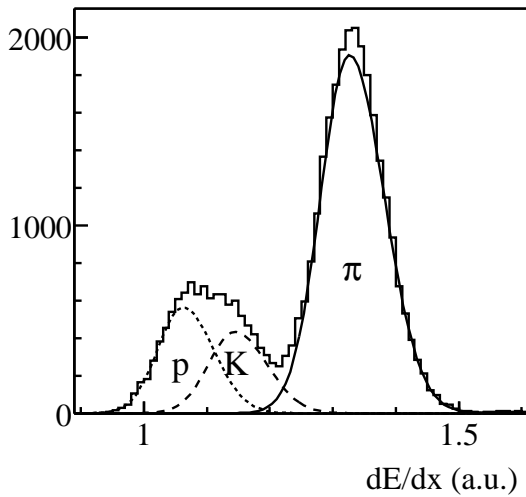
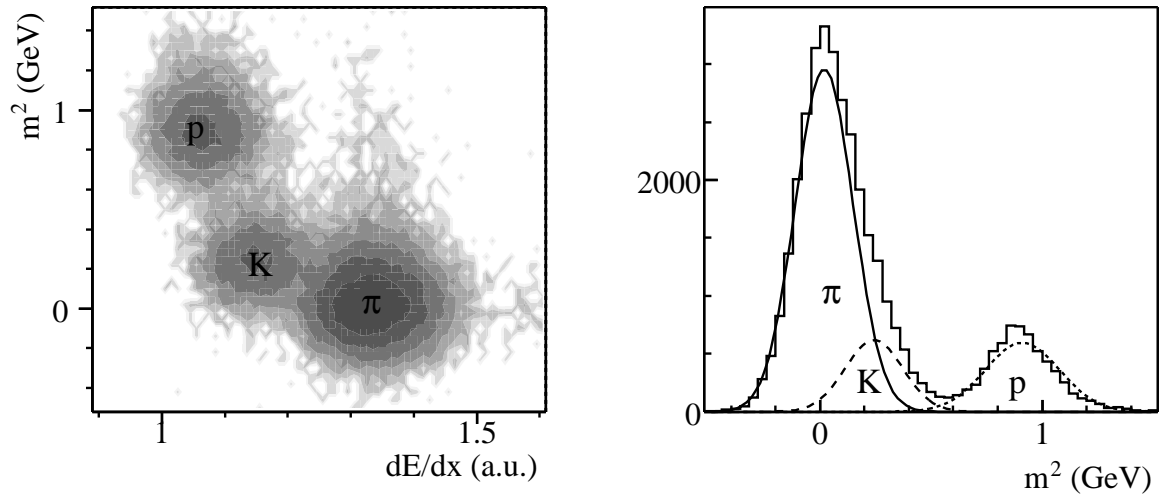


Figure 5.2: (upper left) Distribution of the m^2 measurement from TOF and the dE/dx measurement in the MTPCs for positive tracks close to mid-rapidity with transverse momenta close to 0.5 GeV. (lower left) Projection of the two-dimensional histogram on the dE/dx axis. (upper right) Projection of the two-dimensional histogram on the m^2 axis. In each projected histogram, a projection of the two-dimensional fit is also shown. Indicated are the pion, kaon and proton peaks.

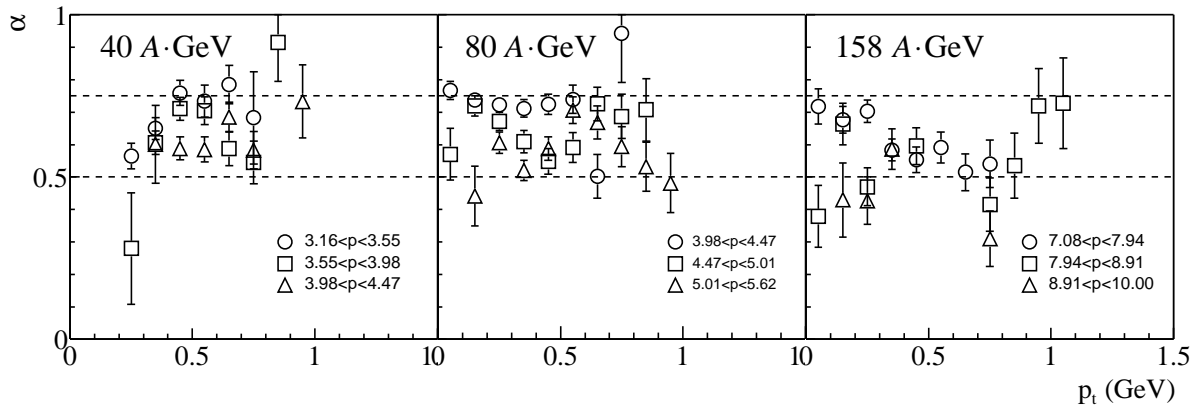


Figure 5.3: Value of the scaling parameter α for the width of the dE/dx peaks as a function of the position, as determined in different bins of total momentum and p_t . The different panels show results at the three different beam energies.

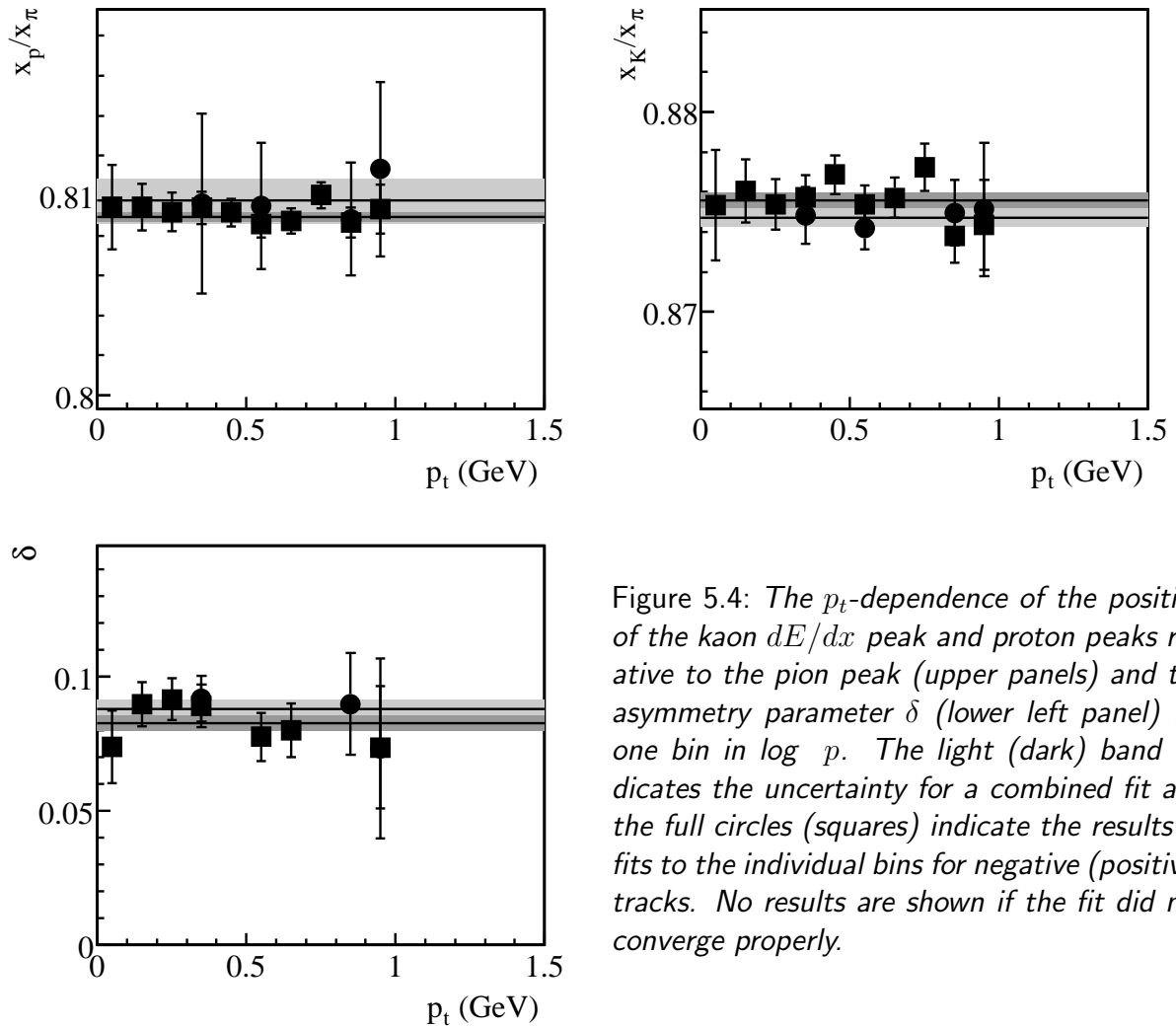


Figure 5.4: The p_t -dependence of the position of the kaon dE/dx peak and proton peaks relative to the pion peak (upper panels) and the asymmetry parameter δ (lower left panel) for one bin in $\log p$. The light (dark) band indicates the uncertainty for a combined fit and the full circles (squares) indicate the results of fits to the individual bins for negative (positive) tracks. No results are shown if the fit did not converge properly.

The function which is fitted to the dE/dx distributions to extract the yields is a sum of four asymmetric Gaussians (see Eq. 4.3); one for each particle species. The asymmetry parameter δ is taken to be the same for all species. The width of the dE/dx -peak for each species depends on the position as defined Eq. 5.1, with $\alpha = 0.625$. Since the width is also dependent on the number of clusters on each track, a sum was taken over the track-length distribution in each bin. It was assumed that the width scales with the square root of the number of samples l on a track, leading to the following function for a single peak:

$$g_i(x; A_i, x_i, \delta, \sigma, \alpha) = A_i \sum_l \frac{n_l}{N_{tot}} \exp -\frac{1}{2} \left(\frac{x - x_i}{(1 \pm \delta)\sigma_{i,l}} \right)^2, \text{ with } \sigma_{i,l} = \frac{\sigma x_i^\alpha}{\sqrt{l}} \quad (5.2)$$

In the sum, each Gaussian is weighted with the fraction of tracks with length l : n_l/N_{tot} .

The parametrisation of the dE/dx distribution has in total 10 parameters: 4 amplitudes, 4 positions, the width σ and the asymmetry parameter δ . It is impossible to determine all of these parameters reliably in each bin because some particle species are rare in certain bins. To constrain the fits, it was assumed that ratios of the positions of the proton and kaon peaks to the positions of the pion peak does not depend on p_t and also

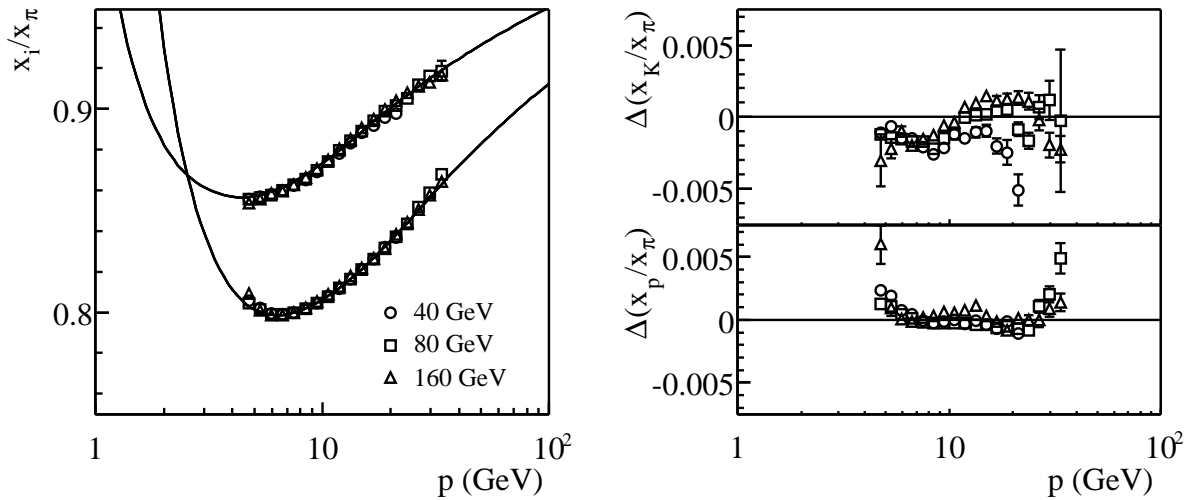


Figure 5.5: Momentum dependence of the fitted peak positions of the kaon and proton dE/dx peaks at the three beam energies. Also shown is a fit of the Bethe-Bloch parametrisation Eq. 4.1 to the obtained positions. The right panel shows the difference between the fitted kaon and proton positions and the Bethe-Bloch parametrisation.

that the asymmetry parameter is independent of p_t . These parameters are also assumed to be equal for positive and negative particles. To test these assumptions, separate fits were performed to the bins with the highest numbers of tracks and the results are compared to the combined fit. The result of this procedure is shown for a single momentum bin ($1 < \log_{10}p/ \text{GeV} < 1.05$) at 158 A·GeV in Figure 5.4. It can be seen that the parameters of the fits in the single p_t -bins are compatible with the result of the combined fits and that the parameters for negative and positive particles are also compatible.

The resulting values of the proton and kaon peak positions relative to the pion peak and the asymmetry parameter as determined by the fit in each momentum bin are shown in Figures 5.5 and 5.6. The peak positions are well described by the Bethe Bloch formula (Eq. 4.1) as shown in the left panel of Figure 5.5. The differences between the fitted positions and the Bethe-Bloch formula which are shown in the right panel of Figure 5.5 are below 0.2% for most momentum bins. The differences between results at the different energies are of similar size.

For completeness, the asymmetry parameters δ as obtained from the fits are also shown, in Figure 5.6. A somewhat different dependence of δ on the total momentum is found for the different beam energies, probably due to the different track-lengths resulting from the scaling of the magnetic field.

5.5 Acceptance and efficiency

The kaon yields as determined from the fits to the dE/dx spectra were corrected for geometrical acceptance, decay losses and reconstruction efficiency. The correction for geometrical acceptance and kaon decays is purely determined by the detector geometry and the magnetic field, while the reconstruction efficiency also depends on the track

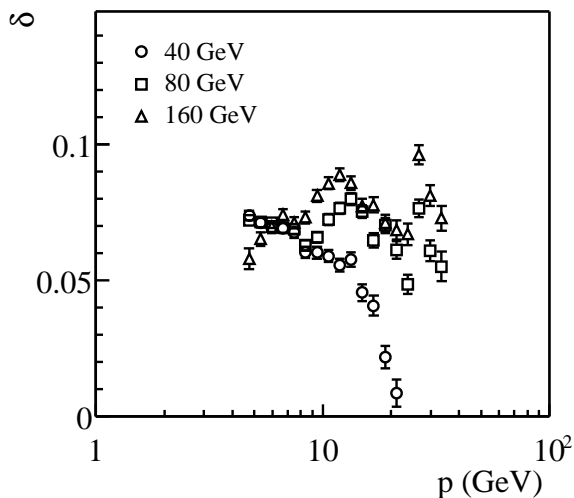


Figure 5.6: *The asymmetry parameters δ as obtained from the fits at the three energies.*

density.

The correction for acceptance and kaon decay losses was determined using a large sample of tracks in a purely geometrical simulation. The efficiency correction was determined separately, using a smaller sample of simulated tracks which were combined with real events to obtain a realistic track density; the so-called embedding procedure. In order to reduce the number of tracks needed for the efficiency calculation, the tracks were pre-selected by a geometrical cuts which are somewhat less restrictive than the cuts in the analysis.

The acceptance and decay corrections were calculated by generating a sample of tracks which are distributed uniformly in $\log p$ and p_t in an area which is larger than the MTPC acceptance within the 30° ϕ -cut used in the analysis. The generated tracks are tracked through the magnetic field using GEANT [45] and the number of hits in each of the TPCs is counted. A track is accepted if it leaves 50 or more points in the MTPC. Decaying kaons are also rejected if they decay before reaching half of their potential track-length in the MTPC. The ratio of accepted and generated tracks in each $\log p, p_t$ bin is calculated and used to correct the measured kaon yields. Up to one million tracks were used in this procedure at each energy. The calculated acceptance is shown in Figure 5.1.

For the efficiency calculation, events were generated containing up to three K^+ and K^- . Only tracks with 30 or more points in the main TPC and well separated trajectories were used. The generated tracks are tracked through the TPCs using GEANT and the hits as generated by GEANT are converted into raw NA49 data using a program which simulates the response of the TPC [38, 46]. The generated raw data are then combined with a real event and the combined event is reconstructed using the normal reconstruction procedure. This procedure ensures a realistic track density including possible noise hits, but does not take into account correlations between the tracks in the event. Some correlations are known to exist in lead-lead events (Bose-Einstein correlations and elliptic flow) but the effect of these correlations on the overall efficiency is expected to be small. Note also that for every six simulated tracks a full event is reconstructed (containing approximately 1500 charged particles). Between 20 and 30 thousand of these events

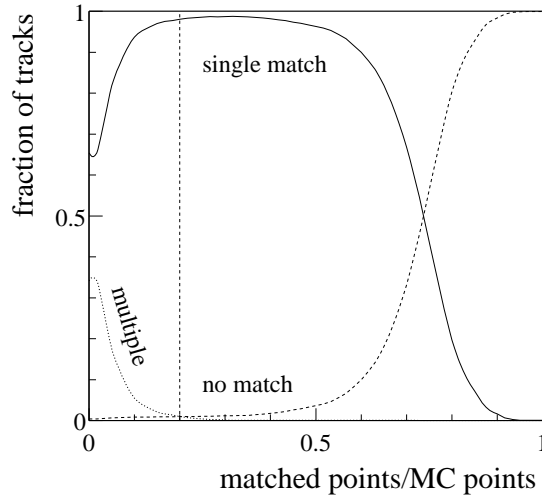


Figure 5.7: *Dependence of the reconstruction efficiency on the cut on the fraction of generated points which were matched to a reconstructed point on the matching track(s). Shown are the fraction of tracks with exactly one (full line) and zero matches (dashed line) and the fraction with multiple matches (dotted line).*

were processed at both 40 and 158 $A\cdot\text{GeV}$. The efficiency corrections at 80 $A\cdot\text{GeV}$ were determined using an interpolation procedure.

To determine which of the generated tracks were properly reconstructed, all reconstructed tracks are compared to generated tracks on a point-by-point basis. Due to the high track density, a single generated track can have a number of matching reconstructed tracks. In the analysis of the embedded events, a cut is applied on the fraction of generated points which is assigned to the reconstructed track. In Figure 5.7 the dependence of the overall inefficiency on this cut is indicated by the dashed line. The fraction of generated tracks with a single match (full line) and with multiple matches (dotted line) are separately indicated. The efficiency is stable up to a cut value of 0.4. A value of 0.2 was used in the further analysis.

The efficiency was calculated in each analysis bin by dividing the number of tracks with at least one match which satisfies the analysis cuts by the number of generated tracks, which have enough points to be accepted in the analysis. The efficiency depends on the track density, and is therefore higher at 40 than at 158 $A\cdot\text{GeV}$. For the 158 $A\cdot\text{GeV}$ data the efficiency was found to be between 95 and 100% in all bins. About half of the bins have an efficiency above 98%. For the 40 $A\cdot\text{GeV}$ data the efficiency is better than 98% in all bins.

5.6 Results

The measured yields as a function of $\log p$ and p_t are corrected for acceptance and efficiency losses. The resulting corrected yields are still on a rectangular grid in $\log p$ and p_t . This grid was transformed to a grid of rapidity and transverse momentum, using the following

equation:

$$\frac{d^2 N}{dp_t dy} = E \frac{d^2 N}{dp_t dp_z} = E \frac{p_z}{p} \frac{d^2 N}{dp_t dp}, \quad (5.3)$$

where $d^2 N/(dp_t dp)$ is the corrected yield as determined from the fits in each bin. Since lines of equal rapidity are curved in the p, p_t -plane (see Figure 5.1), the rectangular grid in p, p_t is transformed into a non-rectangular grid. A linear interpolation in rapidity was used to obtain p_t spectra at different rapidities. To avoid correlations between the p_t -spectra, they were determined at intervals of 0.2 units of rapidity, corresponding to approximately twice the width of the $\log p$ -bins. The systematic error associated with the interpolation is expected to be negligible.

The measured transverse momentum distributions are shown in Figure 5.8. The spectra are parametrised using an exponential distribution in m_t

$$\frac{d^2 N}{p_t dp_t dy} = \frac{dN/dy}{T_{eff}(m + T_{eff})} e^{-(m_t - m)/T_{eff}}, \quad (5.4)$$

where T_{eff} is the inverse slope parameter ('effective temperature', see section 6.1) and $m_t = \sqrt{m^2 + p_t^2}$.

The inverse slope parameters as obtained from the fits are shown in Figure 5.9. For comparison, the result of the combined TOF- dE/dx analysis, which is a separate analysis, not described in this thesis, is also shown (open symbols). The slope parameters for the K^- are systematically lower than for K^+ , but the differences are small. At 80 and 158 A·GeV, the slope parameters are approximately constant in a region of up to more than one unit of rapidity around mid-rapidity. The slope parameters decrease slightly (less than 25%) at higher rapidities. At 40 A·GeV, the slope parameter is almost constant in the region from mid-rapidity (the TOF- dE/dx analysis result) to the first rapidity point of the dE/dx -only analysis, at $y \approx 0.7$, and decreases to higher rapidities.

To obtain rapidity distributions, the measured points of the p_t distribution were summed and the spectra were extrapolated into the unmeasured range using the exponential fits. The extrapolation represents less than 5% of the yield in most bins, but reaches up to 20% at the edges of the measured rapidity interval. The rapidity distributions for K^+ and K^- at the three different energies are shown in Figure 5.10. The results of the separately performed TOF- dE/dx analysis at mid-rapidity are indicated by full circles.

The total yields of kaons at the different energies were obtained by fitting the measured rapidity distributions with a double Gaussian (curves in Figure 5.10):

$$\frac{dN}{dy} = \frac{N}{2\sigma\sqrt{2\pi}} \cdot \left[\exp\left(-\frac{(y - y_0)^2}{2\sigma^2}\right) + \exp\left(-\frac{(y + y_0)^2}{2\sigma^2}\right) \right]. \quad (5.5)$$

The total yields $N(K^+)$, $N(K^-)$ and widths of the spectra are given in Table 5.1. The width of the fitted spectra is determined by both y_0 and σ in Eq. 5.5 and is given in terms of the full width at half the maximum (FWHM) in Table 5.1. Clearly, the widths of the spectra increase with beam energy, the K^- distribution being somewhat narrower than the K^+ distribution at each energy. Both the K^+ and the K^- multiplicity increase with energy.

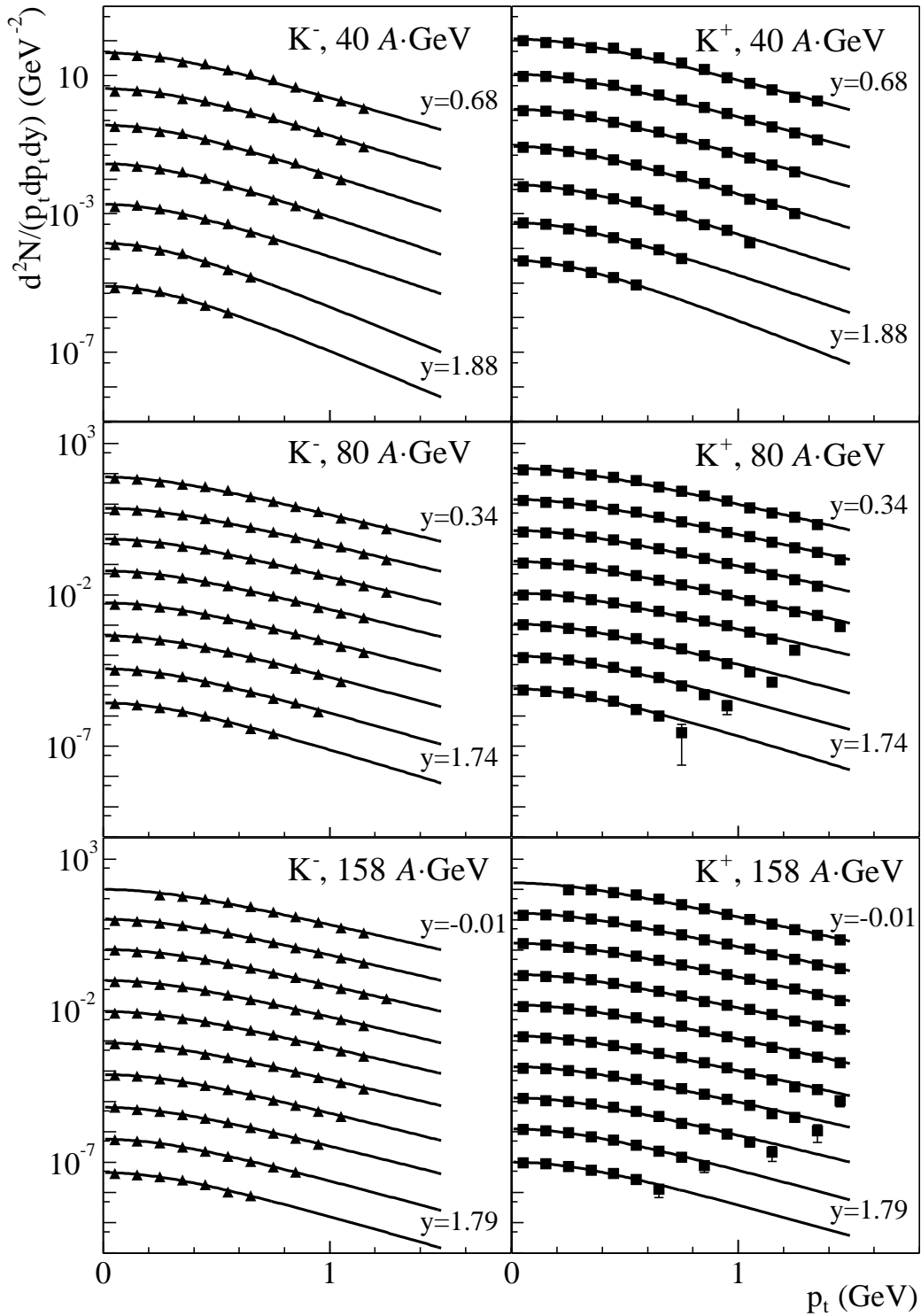


Figure 5.8: Transverse momentum distributions for kaons at the three different beam energies. The results are given for K^- in the left panels and K^+ in the right panels. Also shown are fits to the spectra according to Eq. 5.4. The spectra were scaled down by subsequent factors of 10 for display purposes.

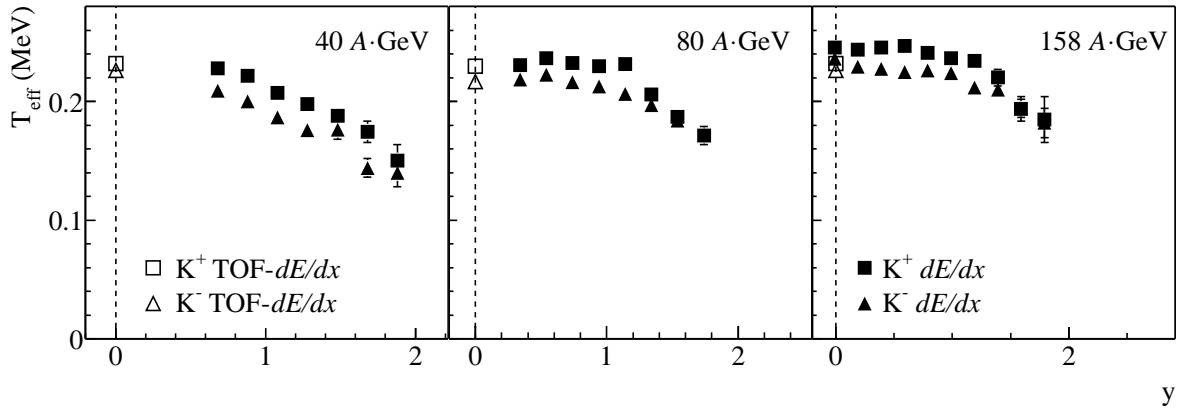


Figure 5.9: The inverse slope parameters as obtained from fits to the p_t -spectra in all rapidity bins. The values obtained from the fit to the spectra obtained by the combined TOF- dE/dx analysis are also shown (open symbols).

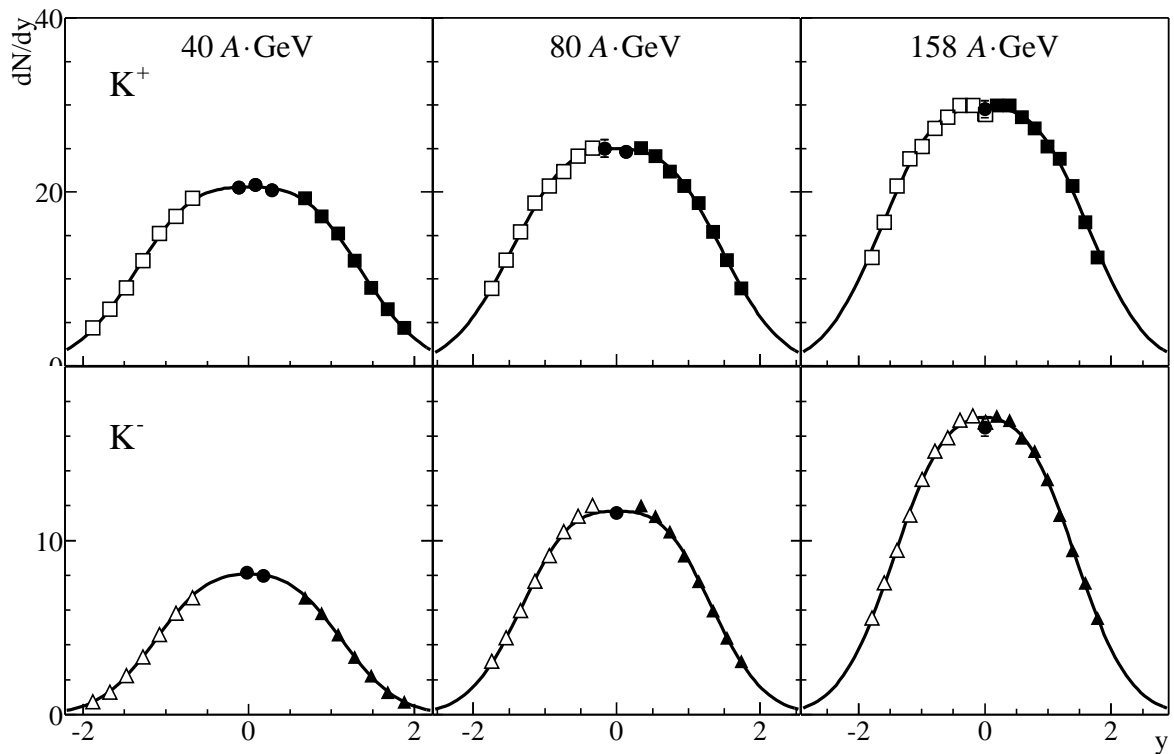


Figure 5.10: Rapidity spectra of positive and negative kaons at 40, 80 and 158 A·GeV. The closed squares and triangles are the result of the dE/dx analysis, while the open point are reflected at mid-rapidity. The full circles at mid-rapidity indicate the results from the TOF- dE/dx analysis. The drawn line is the result of a double Gaussian fit.

	40 $A\cdot\text{GeV}$	80 $A\cdot\text{GeV}$	158 $A\cdot\text{GeV}$
$N(K^+)$	59.1 ± 1.9	76.9 ± 2	103.0 ± 5
FWHM (K^+)	2.8	3.0	3.4
$N(K^-)$	19.2 ± 0.5	32.4 ± 0.6	51.9 ± 1.9
FWHM (K^-)	2.3	2.7	3.0

Table 5.1: Total yields and width of the rapidity distribution for positive and negative kaons at all three energies. The quoted errors only include statistical errors.

5.7 Systematic errors

In this section a number of sources of systematic uncertainties is described and an estimate is given of the magnitude of resulting uncertainties.

General checks

An important check for the general analysis procedure is the comparison between the results from the dE/dx -only analysis, as presented in this chapter and the results from the TOF- dE/dx analysis, which is a separate analysis, using different cuts and separately calculated corrections for acceptance and decays. Both the yields (see Figure 5.10) and the inverse slope parameters (see Figure 5.9) from both analyses agree to within 5% at 158 $A\cdot\text{GeV}$, where the acceptance for the dE/dx analysis and the combined analysis overlap.

In addition, the data taken with reverse field polarity were analysed and the raw yields from the dE/dx fits were compared. Again, the results agree to better than 5% and there are no indications of systematic deviations.

The efficiency corrections using the embedding procedure were checked by applying a cut on the track impact parameters b_x and b_y . This resulted in a relatively large decrease of the calculated efficiencies of up to 7%, but the corrected yields stayed within the statistical errors.

Fitting procedure

One of the sources of systematic uncertainty are the assumptions which go into the fit of the dE/dx spectra, such as the value of α and the assumption that certain fit parameters are independent of p_t . It has been shown in Section 5.4 that the assumptions are reasonable within the statistical accuracy we can achieve. The largest uncertainty is in the value of α . To investigate the effect of this uncertainty, the value of α used in the analysis was varied by ± 0.125 , resulting in changes of the fitted yields of 2% or less.

Acceptance and kaon decay correction

The acceptance as shown in Figure 5.1 is independent of total and transverse momentum in most of the analysed bins and close to 100%. The edges of the detectors where the acceptance drops are excluded from the analysis by appropriate cuts. The remaining correction for the decay of kaons reaches values up to 30% at low momenta. The associated

uncertainty, however, is much smaller, since the kaon life time is very well known ($\tau = (1.2386 \pm 0.002) \times 10^{-8}$ s [47]).

The main uncertainty in the decay losses is to determine when exactly a decaying kaon is lost for the analysis. If the kink in the track trajectory at the decay point is recognised by the reconstruction software, the reconstructed kaon track ends at the decay point. As a result, kaons which decay during the first half of their trajectory through the MTPC are rejected from the analysis by the cut on the ratio of reconstructed and potential points in the MTPC. Simulations using the embedding procedure have shown that the efficiency to recognise kinks occurring inside the MTPC is above 95%. If the decay kink is not recognised, but the decay occurs before the track reaches the MTPC, the measured dE/dx value is close to the pion dE/dx , and the track will not be counted as a kaon track either.

We conclude that only for tracks which decay in the second half of their trajectory through the MTPC, it is not completely certain whether they are accepted in the analysis. The fraction of tracks which decays in the second half of their MTPC trajectory is negligible in most bins, but reaches up to 4% in a few bins at low momentum. The uncertainty in the kaon decay correction is certainly below this value for all bins.

Tracking efficiency correction

The correction for tracking efficiency was determined using the embedding method, which ensured a realistic track density in the simulation. The obtained efficiency is above 95% in all bins. It is difficult to quantitatively estimate the associated error, but we assume that it is of the order of 2% or less.

Extrapolation errors

To obtain the rapidity spectra, the transverse momentum spectra were extrapolated using a fit to the measured points. The statistical error on these extrapolations was taken into account in the total statistical error. The extrapolation amounts to less than 5% in most of the bins. It can be seen from Figure 5.8 that there is not much freedom in choosing an alternative extrapolation procedure. The associated systematic error is therefore estimated to be very small (below 1% for most bins).

The extrapolation in rapidity represents less than 10% of the total yield in all cases. Since the measurements extend relatively close to the kinematic limit (which is just beyond beam rapidity for proton-proton collisions), there is again not much freedom in the extrapolation. Using a linear extrapolation, for instance, we observed that the differences are within 5%.

Taking into account the above systematic errors, the total systematic error is estimated to be approximately 5% on each point. The systematic error on the total yield is of similar size.

Chapter 6

Discussion of the kaon analysis results

6.1 Shapes of the spectra

In this section, the shapes of the measured kaon spectra are compared to the expectations for a thermalised hadron gas, the Boltzmann distribution of Eq. 2.13. The Boltzmann distribution can be rewritten in terms of rapidity y and m_t , using the relation $E = m_t \cosh y$

$$\frac{d^2N}{m_t dm_t dy} = E \frac{d^3N}{dp^3} \propto E e^{-E/T} = m_t \cosh y \exp -\frac{m_t \cosh y}{T}. \quad (6.1)$$

Clearly, the expected m_t -distributions at different values of y are exponential in m_t . In Figure 5.8 it was already shown that the measured p_t -spectra are well described by the exponential parametrisation of Eq. 5.4. From Eq. 6.1, however, we not only expect the exponential shape of the m_t -spectra, but a specific relation between the inverse slope parameter or effective temperature T_{eff} and the temperature T of the hadron gas:¹

$$T_{eff} \approx T / \cosh y. \quad (6.2)$$

In Figure 5.9 it is seen that the measured inverse slope parameters do not decrease as $1/\cosh y$, but are almost independent of rapidity within ± 1 unit around mid-rapidity (slightly less at 40 A·GeV). We can conclude that the momentum distribution of produced particles is not spherically symmetric, like the Boltzmann distribution, but is rather elongated. This implies that either the hadrons are not thermalised, or they are thermalised but experience a collective velocity along the beam direction.

By integrating Eq. 6.1 over m_t , the rapidity distribution for a Boltzmann gas is obtained:

$$\frac{dN}{dy} \propto T^3 \left(\frac{m^2}{T^2} + \frac{2m}{T \cosh y} + \frac{2}{\cosh^2 y} \right) \exp \left(-\frac{m}{T} \cosh y \right). \quad (6.3)$$

This distribution was calculated using $T = 220$ MeV for K^- and $T = 230$ MeV for K^+ , which are consistent with the fits to the m_t -spectra in Figure 5.8. The resulting distributions are indicated by the dashed curves in Figure 6.1, where they are compared to the experimental data at 158 A·GeV. Clearly, the Boltzmann distribution is much narrower

¹Comparing Eq. 6.1 and Eq. 5.4 shows that one power of m_t is missing in Eq. 5.4, but this only results in a small offset in the slope parameters.

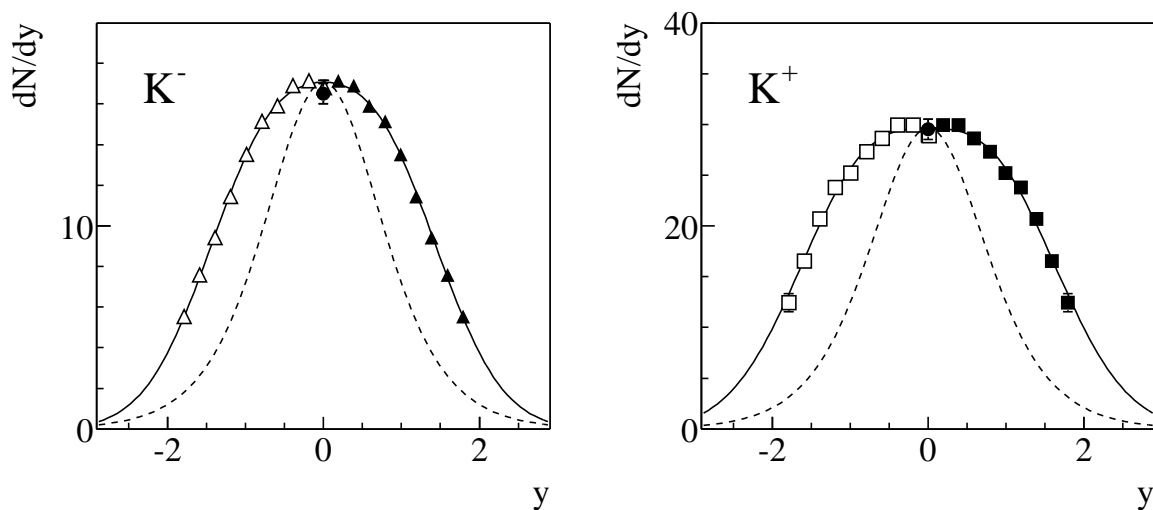


Figure 6.1: Rapidity spectra of kaons at 158 A·GeV, compared to the thermal distribution of Eq. 6.3 (dashed curve).

than the measured distributions. This again implies that the momentum (and velocity) distribution of produced particles is not spherically symmetric, but rather elongated along the beam direction. Again, we conclude that if the hadrons are thermalised, they experience a collective flow velocity along the beam direction.

By using some simplifying assumptions, it is possible to analytically solve hydrodynamical transport equations to quantify collective flow in the transverse direction. The main assumption in the calculation is that particle production is boost-invariant, meaning that the spectral shapes and yields are independent of rapidity. This is of course not exactly true, but it is generally considered a reasonable approximation, because the spectral shapes as characterised by the inverse slope parameter are almost constant in a rather large region around mid-rapidity. Using a boost-invariant superposition of Boltzmann spectra, with the Cooper-Frye freeze-out condition [48], one arrives at [49]

$$\frac{d^2 N}{m_t dm_t dy} \propto m_t K_1 \left(\frac{m_t \cosh \rho}{T} \right) I_0 \left(\frac{p_t \sinh \rho}{T} \right), \quad (6.4)$$

for a radially symmetric expanding source, with expansion velocity β_T and $\rho = \text{atanh } \beta_T$. K_1 and I_0 are modified Bessel functions. The function of Eq. 6.4 is fitted to the measured transverse momentum spectra to determine the temperature T and transverse flow velocity β_T . Only a simultaneous fit to the m_t -distributions of different particle species allows to reliably determine both T and β_T , since a fit to a single species leads to a large correlation between T and β_T . A simultaneous fit to several species also tests whether all spectra give the same values of T and β_T .

The fit was therefore performed using as many species as possible at each of the three beam energies and the result is shown in Figure 6.2. Data from many different analyses performed by the NA49 collaboration are collected in this figure. Most of the spectra are measured in a narrow region around mid-rapidity, but some are integrated over a larger rapidity interval. For details, see [50]. The pion spectra shown in the figure were not used in the fit, because a large fraction of pions is not directly produced but originates from

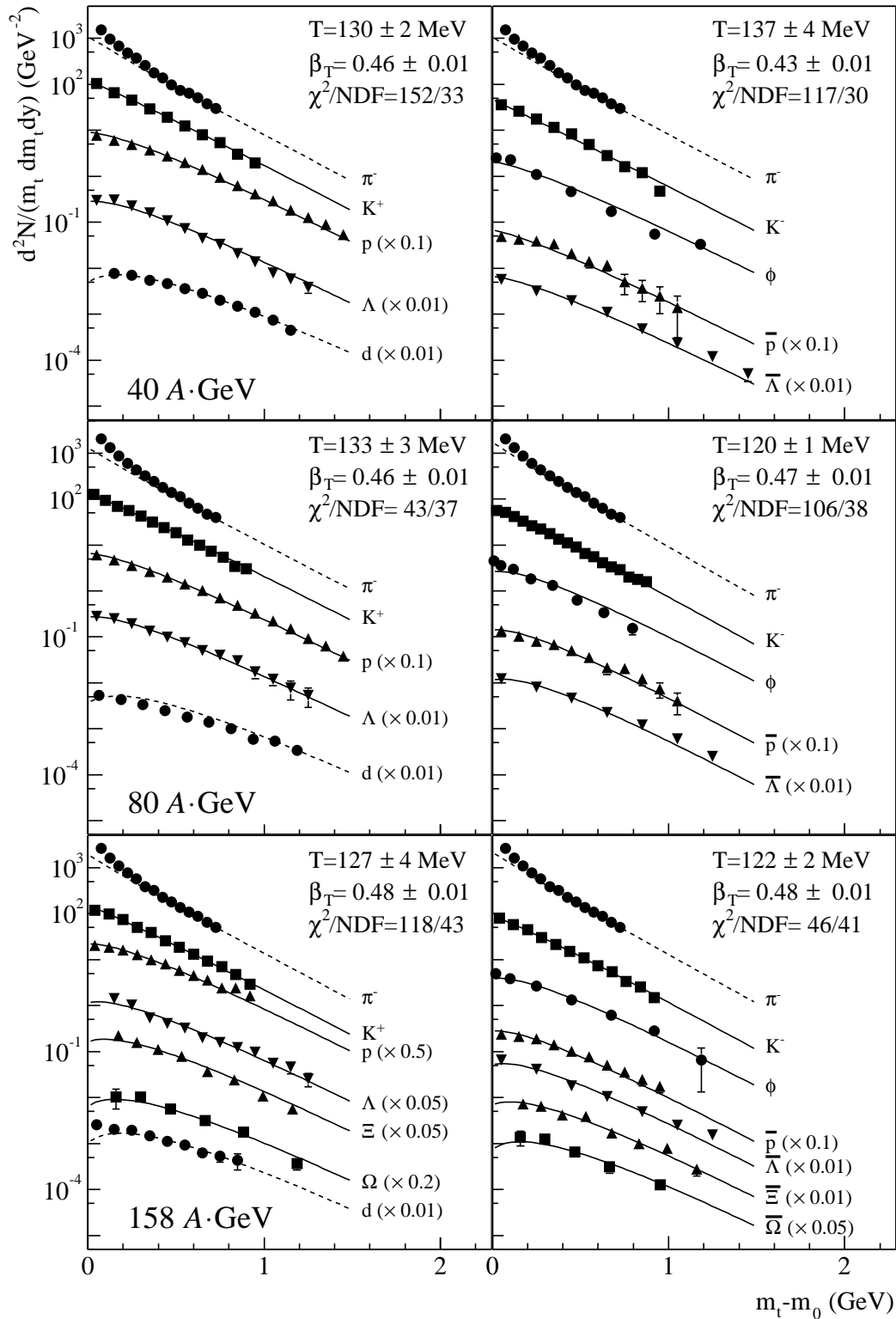


Figure 6.2: *Compilation of all transverse momentum spectra measured by NA49 in 40, 80, and 158 A-GeV central lead-lead collisions. The lines indicate the result of a simultaneous fit of Eq. 6.4 to the spectra. The fits were performed separately in each panel and the values obtained for T and β_T are given.*

resonance decays. The deuterons were also excluded from the fit since these are probably formed by coalescence of a proton and a neutron instead of being produced directly at hadronisation.

According to Eq. 6.4, the spectral shapes of particles and anti-particles are identical, since they have the same mass. To investigate this, the spectra of particles and anti-particles were fitted separately (left and right panels).

Only statistical errors were used in the fit and the resulting errors on the parameters are thus statistical only. Obviously, the model is too simple to expect a perfect fit to the data, but the overall agreement between the data and the fits is striking. No single particle species deviates from the fits in a systematic way (except pions and deuterons which were not included in the fit, see above). The obtained values are in the range $T = 120 - 140$ MeV, $\beta_T = 0.45 - 0.5$, with reasonable agreement between the parameters for the particles and anti-particles and no large energy dependence.

The success of the fit in describing the data could indicate that the particle densities are so large that the dynamics are approximately described by hydrodynamics, and all particles develop a common transverse flow velocity.

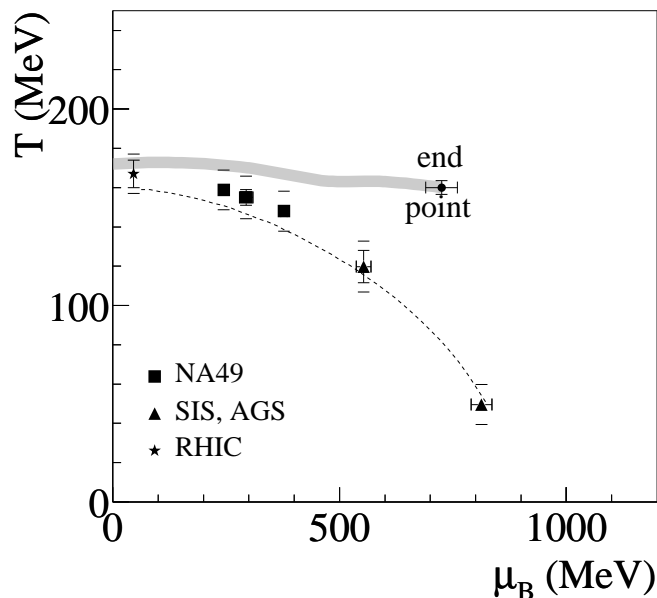


Figure 6.3: Freeze-out points from Hadron Gas Model fits to particle yields at several beam energies, including the three SPS energies [51]. Also shown is the phase boundary from lattice QCD [30] and a parametrisation of the freeze-out curve [29].

6.2 Hadron Gas Model fit

The measured kaon yields were used to also determine the temperature T and baryon chemical potential μ_B from a Hadron Gas Model fit as outlined in Section 2.7. This fit was performed by Becattini [52], using the canonical formalism for strangeness production

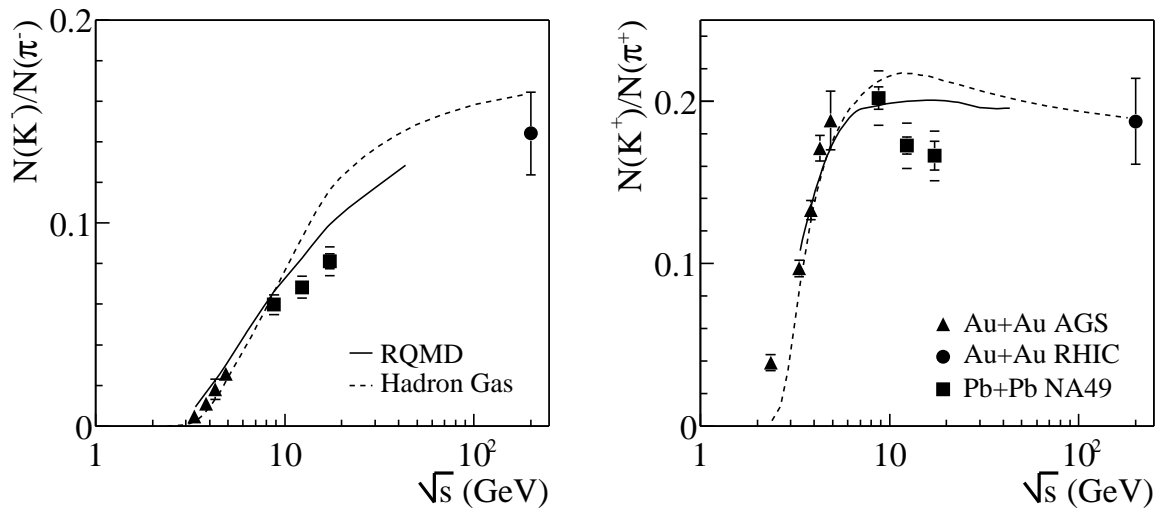


Figure 6.4: Ratios of the total negative (left panel) and positive (right panel) kaon and pion yields. The results from Chapter 5 are indicated by squares. The statistical errors are indicated by an error bar, which is smaller than the marker size in some cases, while the horizontal lines represent the systematic and statistical errors, added in quadrature. The AGS results are given by triangles and the preliminary BRAHMS result is indicated by a full circle.

and a strangeness suppression factor γ_s , as described in [51]. The resulting T and μ_B are compared to the parameters obtained at other energies in Figure 6.3 and to the parametrised freeze-out curve from [29]. It can be seen that the temperature increases only slightly, from $T \approx 150$ MeV at $40 A \cdot \text{GeV}$ to $T \approx 160$ MeV at $158 A \cdot \text{GeV}$, while the baryon chemical potential strongly decreases with beam energy. The freeze-out points are close to the phase-boundary from lattice QCD at all three energies.

It is often argued that the temperatures obtained from these fits are expected to be higher than the temperatures obtained from radial flow fits as described in the previous section, since the particle yields can only be changed by inelastic collisions while the spectra are also changed by elastic collisions. Below a certain temperature, most of the collisions will be elastic, allowing the spectral shapes to stay in equilibrium, while the particle yields are already frozen-out.

6.3 Energy dependence of kaon yields

In Figure 6.4 the energy dependence of the K/π ratio is presented. The squares indicate the results on total K^+ (right panel) and K^- (left panel) production from Chapter 5, normalised by the NA49 results on pion yields. The data are compared to results from the AGS at lower energies and a preliminary result from BRAHMS at $\sqrt{s} = 200$ GeV. The pion yields from NA49 are published together with the kaon results in [32], where references to AGS results can also be found. For BRAHMS, the total yields were determined by fitting their measured points [53] with a Gaussian as shown in Figure 6.5 and taking the area under the curve in the range $|y| < 5.32$.

The most striking feature of the data is that the K^-/π^- ratio increases monotonically

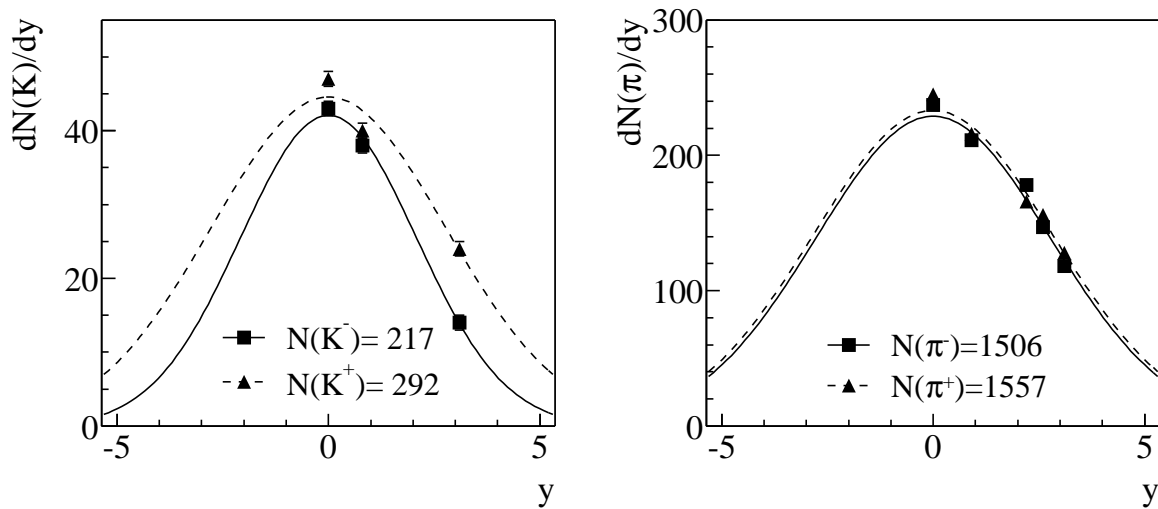


Figure 6.5: Rapidity spectra for kaons (left) and pions (right) as measured by BRAHMS for $\sqrt{s} = 200$ A·GeV Au-Au collisions. The curves indicate Gaussian fits to the measured spectra which were used to determine the total multiplicities.

with collision energy up to RHIC energies, while the K^+/π^+ ratio becomes approximately constant above $\sqrt{s} = 10$ GeV. In fact, the highest K^+/π^+ ratios are measured at the highest AGS energy and the lowest SPS energy (10.74 and 40 A·GeV beam energy, respectively).

Also shown in Figure 6.4 are the expected kaon to pion ratios from RQMD, with colour ropes and rescattering included (see Section 2.6.1) and the Hadron Gas Model (Section 2.7) using the parametrised energy dependence of the temperature and baryon chemical potential, as indicated in Figure 6.3. Both models correctly reproduce the overall behaviour of the data (constant rise of the K^-/π^- ratio and the flattening energy dependence of the K^+/π^+ ratio), but the sudden drop in the K^+/π^+ ratio between 40 and 80 A·GeV is not reproduced. At the moment, it is impossible to quantify the significance of this drop, since the largest contribution to the uncertainties are the systematic errors (indicated by the horizontal lines in Figure 6.4), which are expected to be strongly correlated between the different NA49 points. The drop in the K^+/π^+ ratio is much larger than the statistical uncertainties, which are indicated by the (inner) error bars.

Comparing Figure 6.4 to Figure 2.3 shows that the kaon to pion ratio in nucleus-nucleus collisions is considerably higher than in nucleon-nucleon collisions. This enhancement of the strangeness production in nucleus-nucleus collisions compared to nucleon-nucleon collisions is observed down to the lowest AGS energies, where the initial energy density is not high enough to create a QGP.

Thus strangeness enhancement by itself cannot be a signal of QGP formation as has often been advocated [9]. The observation of strangeness enhancement, however does imply that nucleus-nucleus collisions are not a superposition of independent nucleon-nucleon collisions. In RQMD this is modelled by rescattering of produced particles and colour rope formation, while in the Hadron Gas Model it is the result of the vanishing canonical suppression in large systems. The disappearance of canonical suppression implies that the system is in equilibrium over volumes much larger than the size of a proton. In other

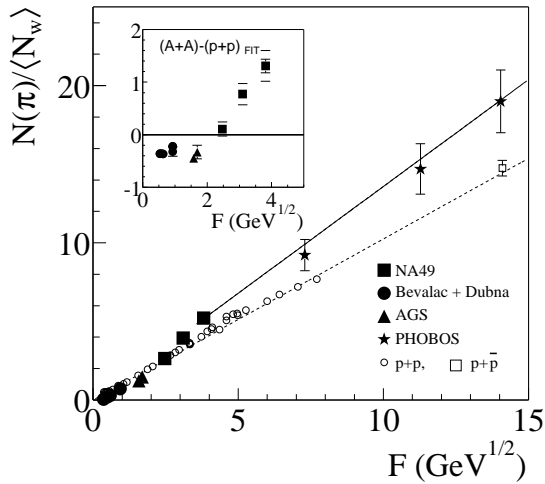


Figure 6.6: Measured pion multiplicities per wounded nucleon in nucleus-nucleus and proton-proton collisions. The lines indicate increase proportional to F as expected in the Statistical Model of the Early Stage.

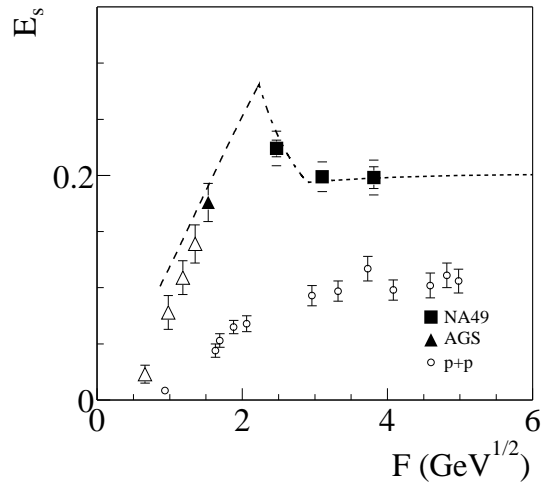


Figure 6.7: Measured values of the strangeness per entropy ratio E_s . Also indicated is the expectation in the SMES with a hadronic phase below $F \approx 2$ (dashed line) and a Quark Gluon Plasma phase above $F \approx 3$ (dotted line). The dash-dotted line indicates the mixed phase.

words, this indicates that a hot and dense system is formed, but it does not exclude that hadrons are still the relevant degrees of freedom, not quarks.

6.4 Statistical Model of the Early Stage

In the Statistical Model of the Early Stage (SMES, see Section 2.7.2) the pion multiplicity is a measure of the initial entropy density. In Figure 6.6 measurements of the pion multiplicity in nucleus-nucleus collisions at AGS, SPS and RHIC are compared to measurements in proton-proton collisions. The inset shows the differences between the measured pion production in nucleus-nucleus collisions and the parametrised energy dependence in proton-proton collisions. Above a certain energy, close to 40 A -GeV, the pion multiplicity per wounded nucleon increases faster with the collision energy than in proton-proton interactions. Within the SMES, this is interpreted as a change of the number of degrees of freedom in the early stage, see Eq. 2.20. At lower energies, the energy dependence of pion production in proton-proton and nucleus-nucleus collisions are similar, with a constant difference between the two. This difference might be due to entropy being carried by baryons instead of pions.

The other observable in the model is the ratio of the total number of strange and anti-strange quarks to the total entropy. A phenomenological correction is used to calculate the total strangeness yield from the yields of kaons, which are the dominant carriers of strange quarks. The total strangeness is calculated as:

$$N_{s\bar{s}} = 2(K^+ + K^-) + (K^+ - K^-)/0.8,$$

where the factor of 2 multiplying the K^+ and K^- yields takes the production of neutral kaons into account and $(K^+ - K^-)/0.8$ is an estimate for the hyperon yield (mostly Λ). The ratio of the total strangeness and total pion yields $E_s = N_{s\bar{s}}/N(\pi)$ is compared to the strangeness to entropy ratio as calculated in the SMES in Figure 6.7. The peak value in the model curve is caused by a phase transition at $T = 200$ MeV, just below 40 $A\cdot\text{GeV}$ beam energy. The measured values of E_s at the two highest energies (80 and 158 $A\cdot\text{GeV}$) correspond to the strangeness to entropy ratio for an ideal gas of (effectively) massless quarks and gluons.

Comparing the curves in Figure 6.7 and Figure 6.4 we conclude that at beam energies of 158 $A\cdot\text{GeV}$ and above, the expected kaon to pion ratios from the Hadron Gas Model and the strangeness to pion ratio as expected from a thermalised Quark Gluon Plasma are in approximate agreement, making it difficult to decide whether quarks or hadrons are the relevant degrees of freedom at the early stage. The sharp peak in the strangeness to entropy ratio at $F \approx 2.1$, or a beam energy of 25 $A\cdot\text{GeV}$, however, is a distinguishing feature of the Statistical Model of the Early Stage. The NA49 data taken at 20 and 30 $A\cdot\text{GeV}$ will allow to detect the peak if it exists.

Chapter 7

Open charm analysis

Due to their larger mass, charm quarks are much less abundantly produced than strange quarks in hadronic collisions. Like strange quarks, however, the production of charm quarks is expected to be enhanced by the high energy densities in a Quark Gluon Plasma. In this chapter the search for D mesons in central Pb-Pb events at 158 A -GeV is presented. The D meson, which carries one charm quark, is often called the ‘open charm’ meson to distinguish it from the ‘hidden charm’ J/ψ which consists of a charm-anti-charm pair.

The D meson lifetime is so short that most of them decay within a few millimeters from the target. This distance is too short to reconstruct the decay point from the tracking information from the TPCs. All tracks were therefore used in an invariant mass analysis. The large multiplicity in central lead-lead events causes a large combinatorial background, which was reduced as much as possible by suitable cuts.

7.1 Invariant mass analysis

The D decay channel which was selected for the analysis

$$\begin{aligned} D^0 &\rightarrow K^- + \pi^+ \\ \bar{D}^0 &\rightarrow K^+ + \pi^- \end{aligned} \tag{7.1}$$

is the decay channel with the largest branching fraction into two charged particles. The branching fraction is 3.83% [47]. Other decay channels with a large branching fraction, but three particles in the final state, for example the widely used $D^* \rightarrow D\pi \rightarrow K\pi\pi$, have also been considered but the increase in combinatorial background is such that the overall sensitivity in these channels is smaller than in the selected channel (7.1).

The invariant mass m is calculated using all pairs of positive and negative tracks in the event, from

$$m^2 = m_1^2 + m_2^2 + 2E_1E_2 - 2\vec{p}_1 \cdot \vec{p}_2 \tag{7.2}$$

where \vec{p}_1 and \vec{p}_2 are the momentum vectors, m_1, m_2 the masses and E_1, E_2 the energies of the decay particles. The masses are not measured directly in the experiment, but the kaon and pion mass are assigned to the negative and positive track respectively for the D^0 decay and vice versa for the \bar{D}^0 candidates. The mass distribution of pairs which originate from a true D decay peaks at the D mass of 1.8646 GeV [47].

The approximately 1400 charged particles which are reconstructed in each event lead to a total of 49 000 D^0 candidate pairs and an equal amount of \bar{D}^0 candidate pairs, while the expected signal is between 0.1 and 10 total neutral D mesons per event (see Chapter 2), of which only 4% decay in the $K\pi$ channel. A major issue in the analysis is therefore to optimise the sensitivity by using as many events as possible and by applying suitable cuts.

The sensitivity ζ of the measurement can be expressed as the ratio of the expected signal N_{sig} and the error on the background (the square root of N_{bkg} , the number of background pairs below the mass peak):

$$\zeta = \frac{N_{sig}}{\sqrt{N_{bkg}}}. \quad (7.3)$$

Both the number of expected signal pairs and the number of background pairs are proportional to the number of events N_{evt} used in the analysis, so that the sensitivity will increase like $\sqrt{N_{evt}}$.

From Eq. 7.3 it is obvious that if a cut reduces signal and background by similar amounts, the sensitivity decreases. It is therefore very important not to reduce the acceptance of the detector by any cuts. This consideration also restricts the possible choices of cuts to reduce the background.

In the analysis, a dE/dx particle identification cut is applied to select kaons. The dE/dx resolution for short low momentum tracks, however, is not sufficient to select kaons. Rejecting all these tracks from the analysis would represent a large acceptance loss, greatly reducing the sensitivity. These tracks are therefore separately analysed and the results of both samples are combined.

7.2 Data samples and cuts

In order to maximise the sensitivity of the analysis, all available samples of central lead-lead events at 158 A-GeV, mentioned in Section 3.9, were used in the analysis.

The large data sample of 3M Pb-Pb events which were taken in the year 2000, with a reduced number of time samples in the TPCs (256 instead of 512), constitutes the main event sample for the analysis. An on-line centrality selection at approximately 20% of the inelastic cross section was applied.

The 800k central Pb-Pb events which were recorded in 1996 at the two different field polarities are also included in the analysis. These data were taken using the standard read-out with 512 time bins and a centrality selection at 10% of the total inelastic cross section.

The data samples were used with the centrality cut as defined by the trigger and no off-line cut was applied on the energy in the Veto Calorimeter. Like in the kaon analysis, the standard event cut requiring that the main vertex could be determined from the beam position detector information was applied.

A minimal set of track cuts was applied, to only remove tracks which have a large probability of either being non-vertex tracks or not being correctly reconstructed. The main requirement is that a track should have a total of 30 or more points in the TPC. Shorter tracks were rejected, because they contain a large fraction of noise hits and have

a worse momentum resolution. To remove tracks which result from hadronic interactions and photon conversions in the detector material downstream of the MTPC, the difference between the potential and the reconstructed number of points was required to be 20 or less in VTPC-1. This cut does not much reduce the reconstruction efficiency for tracks which originate from the main vertex, but gives a significant suppression (10–20%) of tracks in the regions of the detector which contain many conversion tracks.

The remaining sample of kaon candidates was divided in two separate sets as explained in the next section.

7.3 dE/dx selection of kaons

As discussed in Section 4.2.1, the calculation of the the track dE/dx has been modified for the data taken in the year 2000 to accommodate the change of the read-out from the standard 512 time slices to 256 time slices (see Section 3.8). The most important changes concern the threshold loss correction, which was adapted from a procedure based on a two-dimensional fit to each cluster to a procedure using a lookup table and a more complicated cluster shape. The cluster-fit procedure used in the 1996 data is not suitable for the VTPCs and the correction was only applied in the MTPCs. The threshold correction based on the lookup tables, as used in the reconstruction of the 2000 data, was applied for all TPCs.

To demonstrate the effect of these changes, a brief comparison of the dE/dx resolution in the different data sets is presented.

7.3.1 Comparison of the different data samples

In Figure 7.1, the dE/dx measurements for a selected track sample of data taken in 1996 and 2000 are compared. An off-line centrality selection was applied to the 2000 data to reproduce the centrality selection of the 1996 data. From left to right, three panels show the dE/dx measurement in the VTPCs, MTPCs and the combined measurement. The different rows show the distribution for the 512 time slice data taken in 1996 (upper two rows) and the 256 time slice data taken in 2000 (lower rows). The tracks in the plots have total momenta between 8 and 12 GeV, transverse momenta between 0.6 and 0.9 GeV, an angle $\phi < 30^\circ$ with the horizontal plane and 30 or more points in the MTPC. Separate distributions are given for right side tracks ($|\phi| < 30^\circ$), which leave the main vertex in the direction in which they are bent by the magnetic field, and wrong side tracks ($150^\circ < \phi < 210^\circ$). The pads in the TPCs are tilted to be approximately parallel to the right side tracks which leads to relatively small corrections for charge loss due to the threshold in the digitisation. These corrections are larger for wrong side tracks.

For a quantitative comparison, the widths of the dE/dx distributions are characterised by a track length averaged width $\langle\sigma\rangle$ which is calculated from the track-length dependent widths $\sigma_l = \sigma/\sqrt{l}$ as

$$\langle\sigma\rangle = \frac{1}{\sum n_l} \sum_l n_l \frac{\sigma}{\sqrt{l}}, \quad (7.4)$$

where l is the number of points on the track and n_l is the number of tracks with length l . The value of σ is determined by fitting the spectra with the parametrisation of Eq. 5.2.

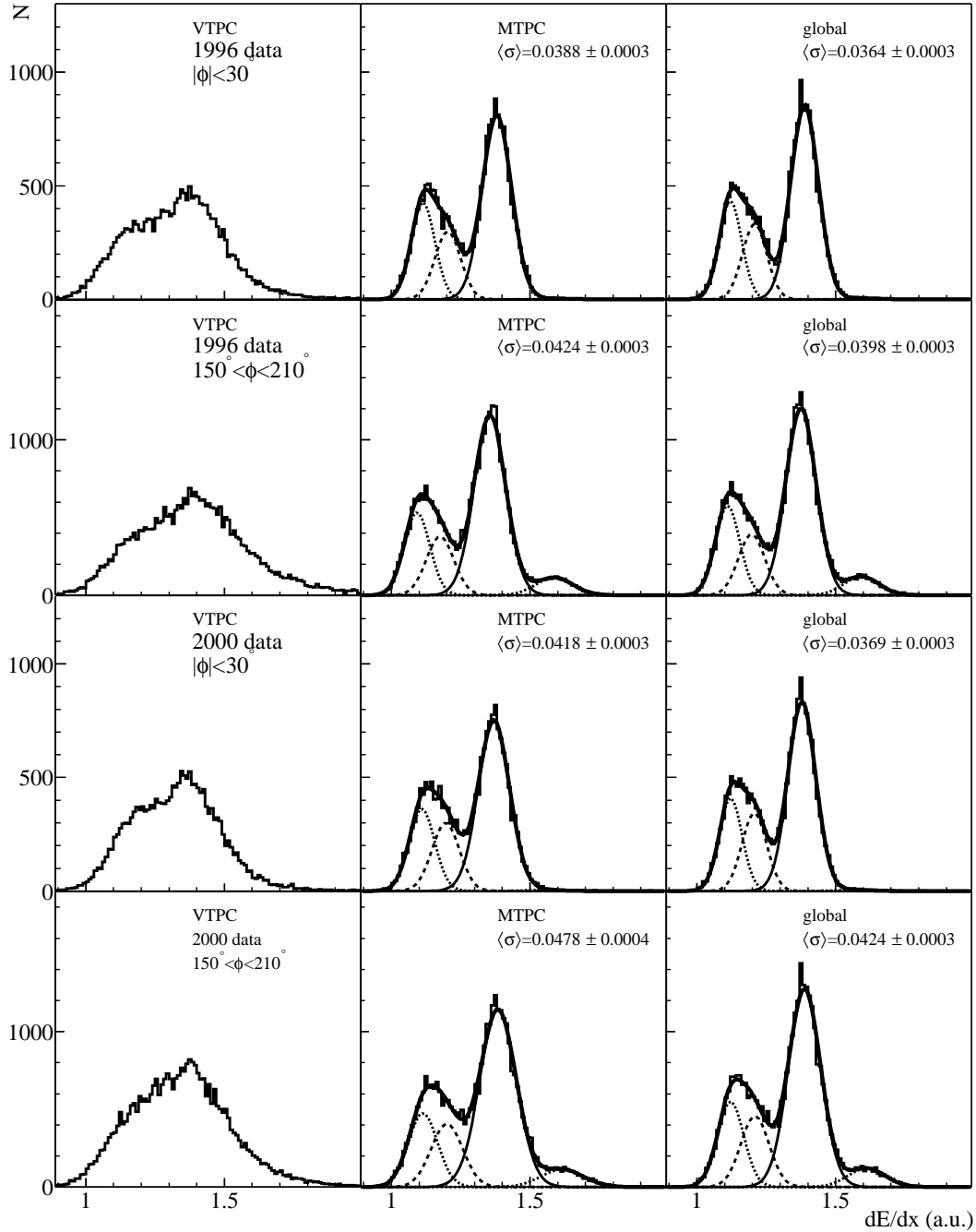


Figure 7.1: Comparison of the dE/dx performance in the 2000 data with 256 time slices (lower panels) and the 1996 data with 512 time slices (upper panels). Shown are the measured dE/dx in the VTPCs (left), the measured dE/dx in the MTPC (middle) and the combined dE/dx (right), for positive tracks with $8 < p < 12$ GeV, $0.6 < p_t < 0.9$ GeV and 30 or more points in the main TPC. The distributions for tracks with azimuthal angles $|\phi| < 30^\circ$ (right side tracks) and $150^\circ < \phi < 210^\circ$ (wrong side tracks) are shown separately. Also indicated are fits to the spectra and average resolution $\langle\sigma\rangle$ as defined in the text.

Figure 7.1 shows that in all four cases, the average resolution using global dE/dx is better than the resolution for main TPC dE/dx only. The increase in resolution when using global dE/dx instead of MTPC dE/dx is much larger in the 2000 data than in the 1996 data. This is due to the better resolution of the vertex TPC dE/dx in the new data sample. The difference in resolution for the VTPC dE/dx can be seen in the left panels of Figure 7.1. Since the tracks in the VTPCs are relatively short, it is impossible to reliably fit the dE/dx distribution to quantify this difference. The better resolution in the VTPC dE/dx is probably due to the application of the threshold loss correction (see Section 4.2.1) to the cluster charges.

The VTPC dE/dx distribution for wrong side tracks in the 1996 data has a tail to high dE/dx values. This is probably due to the merging of clusters at track crossings. In the 2000 data these clusters are not used in the dE/dx calculation and the tail is less pronounced.

It is also visible in Figure 7.1 that the resolution of the MTPC dE/dx measurement in the 512 time slice (1996) data is slightly better than in the 256 time slice (2000) data. This is probably due to the fact that the hardware corrections were optimised for the data with 512 time slices.

7.3.2 Selection procedure

In view of the differences between the dE/dx calculation in the different data samples, we have chosen to use global dE/dx for the 256 time slice data taken in the year 2000 and main TPC dE/dx for the 512 time slice (1996) data.

The tracks were divided in bins of charge, total momentum, transverse momentum and azimuthal angle ϕ at the main vertex. The dE/dx distributions were fitted with Eq. 5.2 in each bin separately. This choice of binning ensures that the track sample is sufficiently uniform with respect to the track angles and the number of points on the tracks in each bin. Possible residual effects of the track angles and number of points on the dE/dx distributions can therefore be absorbed in the fitted parameters. To make the fit more robust, the asymmetry parameter δ in Eq. 5.2 was fixed at 5%. Separate fits were performed for the different datasets (two field polarities in 1996 and the 2000 sample), and the relative proton and kaon positions were taken to be independent of p_t .

Inspection of the fitted parameters showed that the less strict track cuts in this analysis as compared to the kaon analysis, especially the inclusion of wrong side tracks, lead to unreliable fits of the dE/dx distributions for tracks with momenta above 30–35 GeV. The dE/dx particle selection will therefore only be applied to tracks with less than 30 GeV total momentum. The lower limit of the applicability of the dE/dx cuts is taken to be $y = 2.9$, as in the kaon analysis. The tracks outside this interval, and tracks with less than 30 points in the MTPC, were separately analysed, without using the dE/dx information.

In the sample where the dE/dx cuts were applied, only tracks within $[-2(1-\delta)\sigma_l, 2(1+\delta)\sigma_l]$ of the kaon peak position were used. The dE/dx resolution $\sigma_l = \sigma/\sqrt{l}$ for each track was calculated taking into account the track length l (see Eq. 5.2). Less than 1% of the kaon tracks fall outside this window and the corresponding inefficiency is neglected.

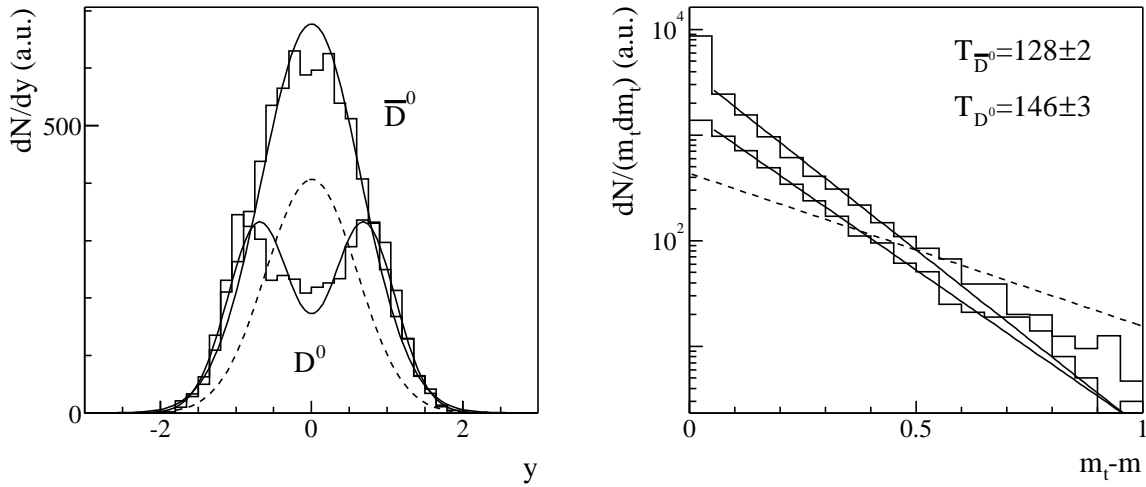


Figure 7.2: Rapidity and transverse mass distribution as generated using PYTHIA [24] for D^0 and \bar{D}^0 . The full lines indicate a double Gaussian fit for the rapidity spectra and an exponential fit for the m_t -spectra. Also indicated (dashed line) is the expectation from a thermal production process.

7.4 Rapidity and transverse momentum distribution

To calculate the acceptance and efficiency for D meson detection, the momentum distribution of the produced D meson must be known. Since this distribution cannot, with the present statistics, be determined from the data it is calculated using PYTHIA 6.131 [24]. The resulting rapidity and m_t distributions of D^0 and \bar{D}^0 mesons are shown in Figure 7.2. The generated distributions are well described by a double Gaussian in rapidity and an exponential m_t distribution as indicated by the full curves in Figure 7.2.

The most striking feature of the distributions generated by PYTHIA is that the D^0 rapidity distribution has maxima at forward and backward rapidities, while the \bar{D}^0 distribution is peaked at mid-rapidity. The difference between the D^0 and \bar{D}^0 rapidity distributions arises because charmed quarks form strings with valence di-quarks, which carry a large fraction of the beam momentum, while charm anti-quarks form strings with single valence quarks, which have smaller momenta [23].

These distributions from PYTHIA cannot be checked against measurements, because no data exist for proton-proton collisions at this energy. Moreover, the momentum distributions could be different in nucleus-nucleus collisions and in proton-proton collisions. In order to investigate the sensitivity of the efficiency correction to the momentum distributions of the D mesons, the corrections will also be evaluated using a ‘thermal’ distribution. The choice of this distribution is motivated from the observation that the width of the rapidity distribution generally decreases with particle mass, while the inverse slope parameter increases with mass. A Gaussian rapidity distribution with a width $\sigma = 0.6$ is a reasonable estimate for the rapidity distribution of particles with a mass of almost 2 GeV. For the inverse slope parameter a value of $T = 300$ MeV is taken. These distributions are indicated by a dashed line in Figure 7.2.

All distributions are parametrised as the product of a double Gaussian in rapidity and

	Δy	σ_y	T (MeV)
\bar{D}^0 PYTHIA	0.443	0.486	128
D^0 PYTHIA	0.688	0.419	146
thermal	0	0.6	300

Table 7.1: Parameters of the different expected momentum distributions for D mesons.

an exponential in m_t :

$$\frac{d^2 N}{dy m_t dm_t} = \left[\exp -\frac{1}{2} \left(\frac{y - \Delta y}{\sigma_y} \right)^2 + \exp -\frac{1}{2} \left(\frac{y + \Delta y}{\sigma_y} \right)^2 \right] \exp \left(-\frac{m_t}{T} \right) \quad (7.5)$$

with parameters Δy , σ_y and T as presented in Table 7.1.

7.5 Efficiency and acceptance

In the charm analysis, the acceptance and efficiency were not determined separately but calculated together using the embedding procedure which is described in Section 5.5. To increase the number of simulated D , up to 5 D meson decays were embedded in each event. The D mesons were generated with a flat distribution in rapidity and a thermal p_t distribution with a slope of 300 MeV. In order to make sure that the generated tracks do not contribute significantly to the track density, decay pairs were removed from the sample when one of the decay tracks came closer than 5 cm to the decay track of another D meson inside the sensitive volume of the detector.

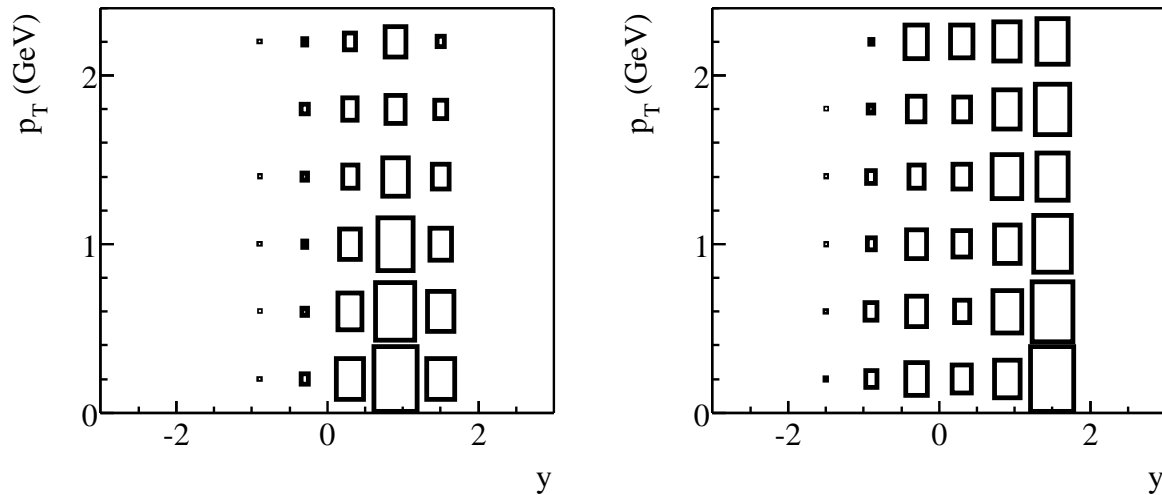


Figure 7.3: Dependence of the product of acceptance and efficiency on rapidity and p_t . The generated distribution was flat in rapidity between -1.6 and 1.6 , and exponential in m_t . The left panel shows the result for decay pairs where the kaon could be selected by dE/dx and the right panel shows the result for decay pairs where dE/dx particle identification could not be used.

The generated tracks were matched to reconstructed tracks and the efficiency was determined using the same cuts as in the analysis. The dependence of the efficiency on rapidity and transverse momentum is shown in Figure 7.3. The left panel shows the efficiency for decay pairs with dE/dx selected kaons and the right panel shows the efficiency for pairs where the dE/dx measurement could not be used to identify kaons. Clearly, the pairs for which the kaon could be identified using the dE/dx measurements occupy a relatively narrow range in rapidity, just forward of mid-rapidity, while the pairs for which no dE/dx cut could be applied have a rather flat distribution, with a peak at very forward rapidities (due to the inclusion of all particles with $p > 30$ GeV in this sample).

Separate samples of embedded events were generated using data taken in 1996 and in 2000, with the reduced number of time slices. All histograms which are shown in the following are produced using the events embedded in 256 time slice data, but the results using the 512 time slice data are similar. The generated events contain mainly \bar{D}^0 decays, but it was checked that the efficiencies for D^0 and \bar{D}^0 are equal within errors, due to the left-right symmetry of the experimental setup.

To determine the total efficiency for the different momentum distributions as shown in Figure 7.2 the distributions used for the embedding procedure were reweighted. The generated D s were divided in bins of rapidity and p_t . For each bin, a weight $w(y, p_t)$ was calculated by dividing the integral of the parametrised momentum distribution (Eq. 7.5) by the number of generated D mesons in that bin. The overall efficiency ϵ is calculated as

$$\epsilon = \frac{\sum_{\text{accepted pairs}} w(y, p_t)}{\sum_{\text{generated pairs}} w(y, p_t)}. \quad (7.6)$$

The error on the calculated efficiency σ_ϵ is given by

$$\sigma_\epsilon = \frac{\sqrt{\sum_{\text{accepted pairs}} w(y, p_t)^2}}{\sum_{\text{generated pairs}} w(y, p_t)}, \quad (7.7)$$

assuming Poisson statistics for the number of accepted pairs in each bin. The obtained efficiencies after all cuts are given in Table 7.2.

In Figure 7.4, the expected rapidity and p_t distributions of produced D^0 (open histograms) are compared to background distributions obtained from the data (shaded histograms). The expected signal distributions were obtained by reweighting the embedded D decays with the thermal distribution. The background distributions contain all pairs with an invariant mass ± 50 MeV from the D mass in a small sample of data events and were scaled down to allow a comparison of the shapes with the simulated distributions. Again the sample with dE/dx selected kaons (dotted line, dark shaded histogram) is shown separately from the sample where the dE/dx information could not be used (dashed line, light shaded histogram).

It is clear from Figure 7.4 that the shapes of the rapidity and p_t distribution in the data are comparable to the expected distributions from true D decays. It is therefore impossible to separate signal and background using these variables.

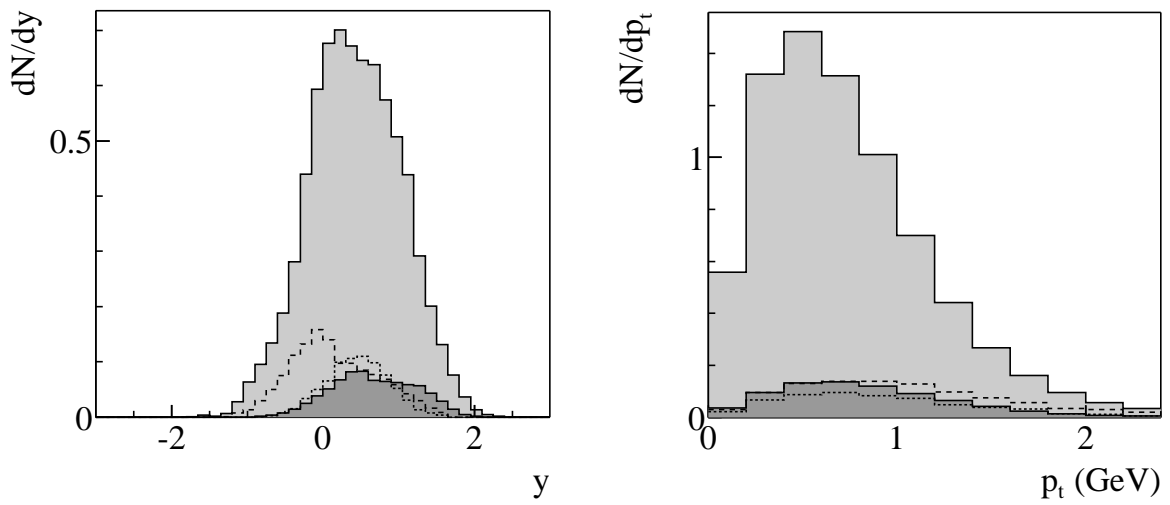


Figure 7.4: Distribution of y and p_t for D^0 candidates. The open histograms represent the expected signal for a single D -meson decaying to a kaon and a pion. These distributions were calculated using the embedding procedure and reweighting the efficiencies with the thermal distribution (dashed line in Figure 7.2). The samples with the kaon in the main TPC (dotted) and with the kaon not reaching the main TPC (dashed) are drawn separately. The filled histograms are the corresponding distributions observed in the data (mostly background). These have been scaled to be comparable to the simulated distributions. The relative amounts of pairs with particle identification for the kaon (light shaded) and without particle identification (dark shaded) are correctly represented.

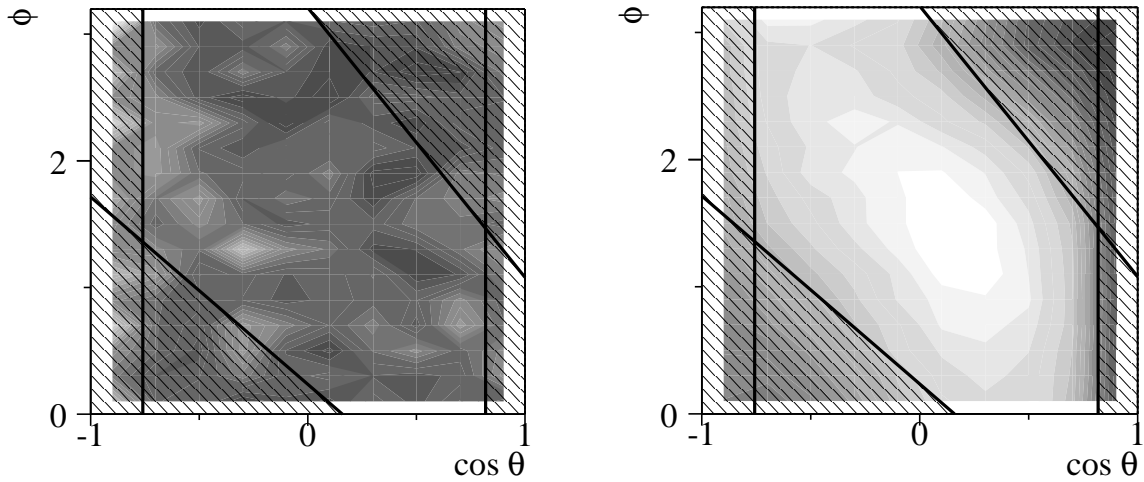


Figure 7.5: Example of the distribution of signal (left) and background (right) in $\cos\theta$ and ϕ . The distributions are for D^0 candidate pairs in a window of ± 50 MeV around the D^0 mass with p_t between 0.8 and 1.2 GeV, and the track sample without kaon identification. The cuts which were used in the analysis are also indicated.

7.6 Decay angle cuts

Each pair of tracks used in the analysis also allows to calculate the flight direction of the decay particles in the decay rest system, where they have equal and opposite momenta. The decay direction can be specified using the polar angle θ between the beam direction and the kaon flight direction and the azimuthal angle ϕ between the kaon and the flight direction of the D in the plane perpendicular to the beam.

An example of the distribution of the background from data and the expected signal in those parameters is shown in Figure 7.5. The distribution for the background clearly peaks at high values of $\cos\theta$, while the signal distribution is more or less flat. The distribution in $\cos\theta$ and ϕ changes with the transverse momentum of the decaying D , and is different for the samples with and without particle identification.

In the analysis, cuts are defined on $\cos\theta$ and ϕ which optimise the sensitivity ζ of the measurement, assuming the thermal distribution for the D mesons. The cuts are a combination of a minimum and maximum value of $\cos\theta$ and two cuts along a straight line in the $\cos\theta - \phi$ plane, as shown in Figure 7.5. The cuts are defined by six parameters (two for each of the straight line cuts and a minimum and maximum for $\cos\theta$) in five transverse momentum bins of 400 MeV. Separate cuts were determined for the samples with and without particle identification for the kaon.

7.7 Efficiency and invariant mass peak shape

The acceptance and efficiency were calculated by reweighting the generated sample of D^0 and \bar{D}^0 decays embedded in data events, as described in Section 7.5 and are presented in Table 7.2. Separate values are given for the sample with and without kaon particle

	with PID			
	256 time slices		512 time slices	
	w/cuts	wo/cuts	w/cuts	wo/cuts
\bar{D}^0 PYTHIA	9.6±0.3	13.5±0.4	9.1±0.4	12.7±0.4
D^0 PYTHIA	10.1±0.3	14.1±0.4	9.6±0.4	13.4±0.4
thermal	8.4±0.3	11.6±0.3	7.6±0.3	10.5±0.3

	without PID			
	256 time slices		512 time slices	
	w/cuts	wo/cuts	w/cuts	wo/cuts
\bar{D}^0 PYTHIA	11.9±0.4	19.9±0.5	7.9±0.3	14.9±0.5
D^0 PYTHIA	11.5±0.3	19.8±0.4	8.2±0.3	15.5±0.4
thermal	12.0±0.3	19.5±0.4	8.0±0.3	14.6±0.4

Table 7.2: Table of the efficiencies (in %) for D detection determined from embedded events.

identification and for embedding in 512 time slice data and 256 time slice data. Both the efficiency with and without the cuts on the decay angles are given in each case. The reduction of the acceptance due to the decay angle cuts is somewhat higher for the sample where no particle identification is available than for the sample with particle identification. The overall efficiency only weakly depends on the rapidity and p_t distribution of the D mesons. The efficiency for the 256 time slice data taken in the year 2000 is comparable to the efficiency for the 512 time slice data for the sample with particle identification. For the sample without particle identification, the efficiency is somewhat higher for the 256 time slice data. This is not the result of the reduction of the number of time slices, but is due to a small change in the tracking code, which treats the sector boundaries in a more accurate way. As a result, many tracks have a few more points, which increases the acceptance for short tracks.

The embedded D decays were also used to determine the shape of the expected invariant mass distribution. The shape of this distribution is entirely determined by detector resolution, since the natural width of the D meson is very small. The distribution as obtained from unweighted embedded events is shown in Figure 7.6. The observed distribution can be parametrised using a Breit-Wigner distribution

$$\frac{dN}{dm} \propto \frac{\Gamma}{m^2 + \frac{1}{4}\Gamma^2} \quad (7.8)$$

with $\Gamma = 6.2$ MeV. The shape of the mass distribution is only weakly dependent on the momentum of the decaying particle.

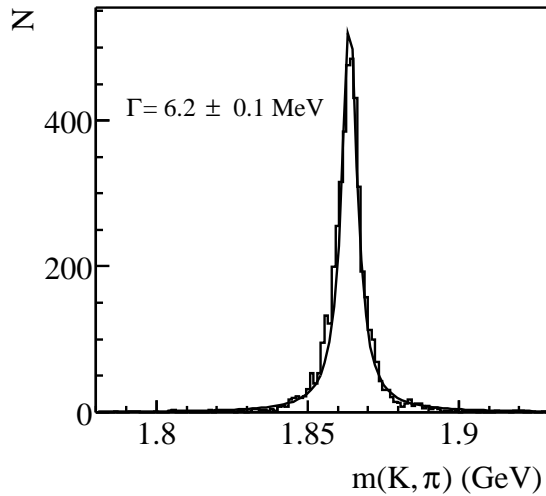


Figure 7.6: Invariant mass distribution of simulated D decays embedded in raw data events taken in the year 2000, with the 256 time slice setting of the detector. The line indicates a fit with a Breit-Wigner distribution function (see text).

7.8 Results

The invariant mass distributions resulting from the analysis of 3.7M events are shown in Figure 7.7. The open histograms represent the mass distribution before application of the decay angle cuts, the shaded histograms are the distributions after application of the decay angle cuts. All values have been scaled to represent the average pair density per event, corrected for the calculated efficiencies, using the thermal distribution functions and the branching ratio for the decay into a kaon and a pion. Separate histograms are given for the sample where the kaon could be identified using dE/dx (right panels) and where no kaon identification cut could be applied (left panels). Clearly, the number of pairs without particle identification is larger than the number of pairs where the kaon could be identified. The upper panels are the distributions for the D^0 candidates, while the lower panels are for \bar{D}^0 candidates. There are more \bar{D}^0 candidates because there are more positive than negative kaons. In addition, the sample of identified positive kaons is contaminated by protons. It can also be seen that the decay angle cuts strongly reduce the background in the sample without particle identification.

The invariant mass histograms are smooth enough to parametrise the background with a polynomial in the region around the D mass. The amount of signal pairs will therefore be determined by fitting the invariant mass histogram with the sum of a polynomial to parametrise the background and the peak shape as parametrised by Eq. 7.8. The stability of the result as a function of the fitted range and the order of the background polynomial is demonstrated in Figure 7.8. The test was performed using D^0 candidate pairs with particle identification (upper right panel in Figure 7.7). The invariant mass distribution was fitted with the sum of the background polynomial and the signal shape, Eq. 7.8, in the range $[m_{D^0} - \Delta m, m_{D^0} + \Delta m]$. The obtained signal is shown in the upper panel of Figure 7.8. The results of the fit with a third order polynomial are indicated by the circles and the light shaded band, while the squares and the dark shaded band are the result

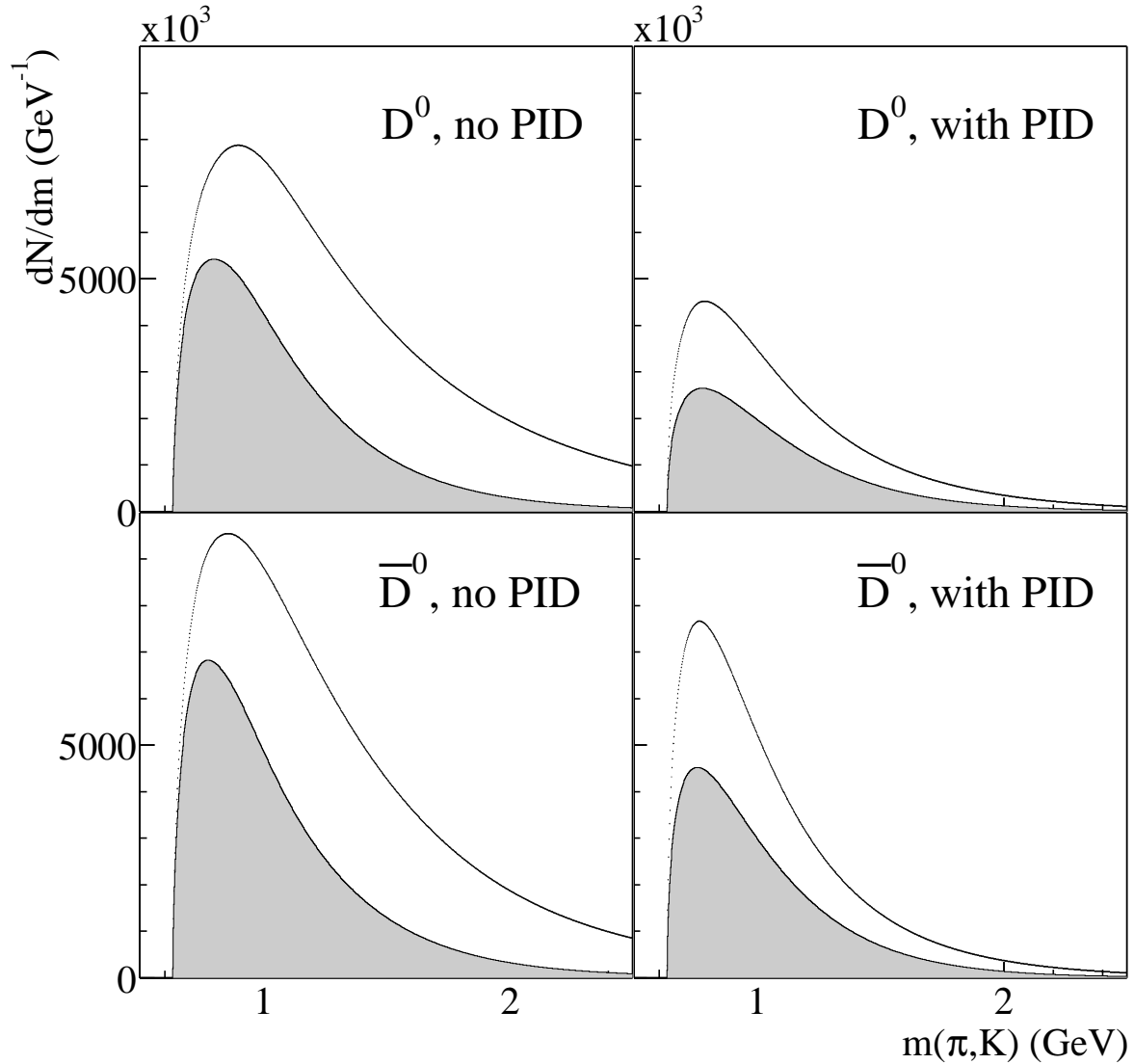


Figure 7.7: Invariant mass distributions of kaon-pion pairs. The upper panels show D^0 candidates and the lower panels show \bar{D}^0 candidates. The left panels are pairs without particle identification for the kaon, and the right panels are pairs where the kaon was identified using dE/dx . The histograms are normalised to represent average pair densities per event, corrected for detection efficiency and the branching ratio for the kaon-pion decay. The open distribution includes all kaon-pion pairs, while the shaded distribution only contains pairs which pass the decay angle cuts as described in Section 7.6.

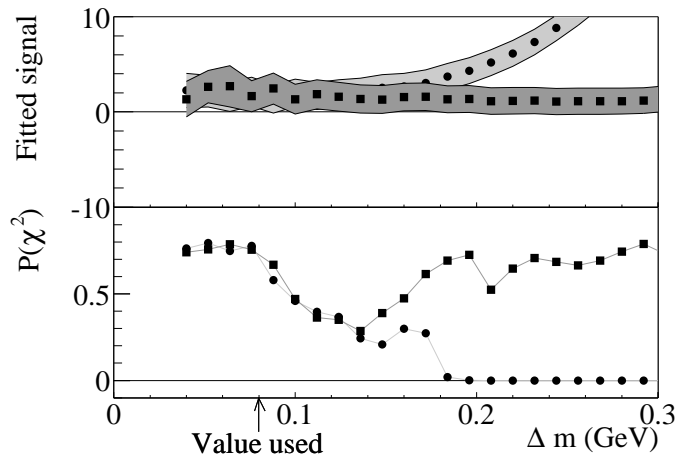


Figure 7.8: The dependence of the fitted total signal on the mass window used for the fit. The upper right distribution of Figure 7.7 was used to determine the total signal with a third (light shade) and fourth (dark shade) order polynomial. The upper panel shows the obtained signal as a function of half the width of the mass window in which the fit was performed. The lower panel shows the χ^2 -probability of the fit.

using a fourth order polynomial. The lower panel of Figure 7.8 shows the χ^2 -probability which is a measure of how well the fit describes the data. It is defined as the probability to find the observed χ^2 or a larger value, given the data. The χ^2 -probability of the third order polynomial fit is relatively stable up to $\Delta m \approx 0.08$ GeV. Only at $\Delta m \geq 0.16$ GeV, the third order polynomial does not properly describe the data and the extracted signal starts to deviate from the signal extracted using the fourth order polynomial. A value of $\Delta m = 0.09$ GeV is used in the analysis.

In Figure 7.9 the invariant mass distributions are shown after subtraction of the background parametrisation. The distributions were fitted with the sum of a third order polynomial and the signal parametrisation, in the displayed region. The four leftmost panels correspond to the four panels of Figure 7.7, showing the results of the samples with and without dE/dx particle identification separately. Those results were combined by taking a weighted average, with weights determined from the average error in the displayed region. The combined D^0 and \bar{D}^0 results are given in the rightmost panel. Clearly, no significant signal is observed. The values obtained from the fits to the combined results are $N(D^0) = -0.41 \pm 0.51$ and $N(\bar{D}^0) = 0.05 \pm 0.54$.

The mass distribution obtained by summing the D^0 candidate pairs and \bar{D}^0 candidate pairs is shown in Figure 7.10. Again, no signal is observed and the fitted integral of the signal distribution is $N(D^0 + \bar{D}^0) = -0.36 \pm 0.74$. These results will be compared to model expectations in the next chapter.

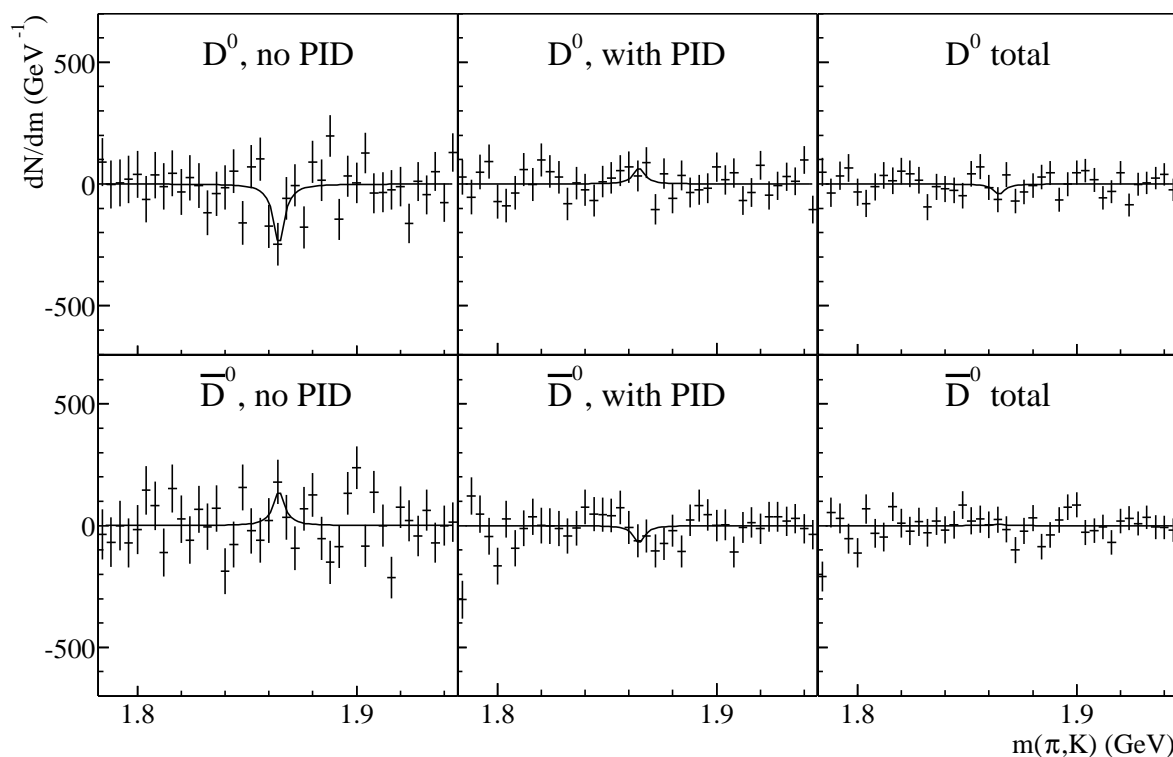


Figure 7.9: The invariant mass distributions from Figure 7.7 after background subtraction. The right panels show the results after combining the samples with and without particle identification.

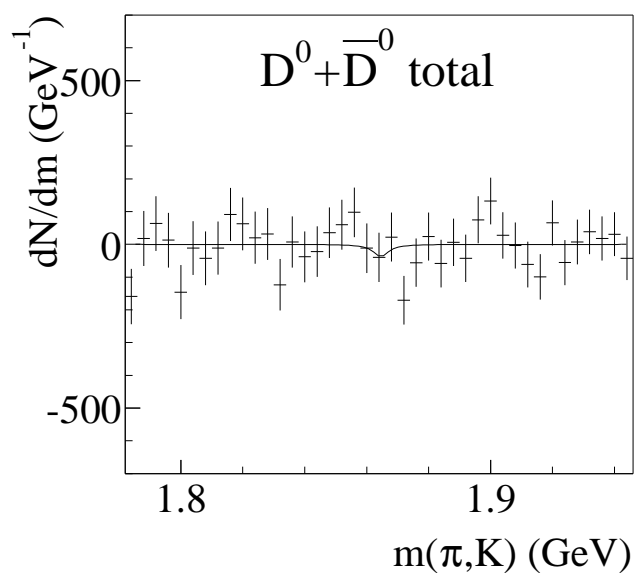


Figure 7.10: Summed invariant mass distribution for D^0 and \bar{D}^0 , after subtraction of the background parametrisation. The line indicates the fitted signal distribution.

Chapter 8

Discussion of the charm result

The open charm analysis presented in Chapter 7 has shown that the neutral D mesons are not produced frequently enough to be detectable in the present data sample. In this chapter the result is compared to different models.

8.1 Comparison to models

In Figure 8.1 the sum of the invariant mass distributions for D^0 and \bar{D}^0 candidates is shown, after background subtraction and compared to three different model expectations.

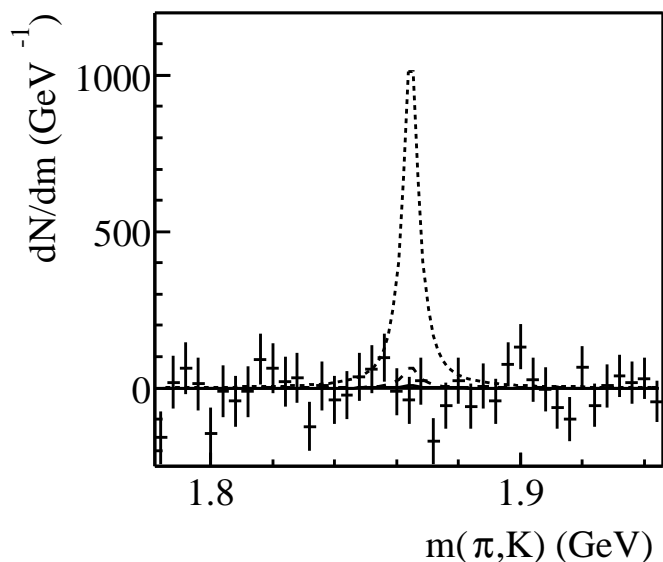


Figure 8.1: Summed invariant mass distribution for D^0 and \bar{D}^0 pairs after subtraction of the parametrised background. The curves indicate expected distributions for the QGP at $T = 265$ MeV (dotted line), the Hadron Gas Model (dashed line) and a Glauber-model superposition of independent nucleon-nucleon collisions (full line, almost coinciding with the line at $dN/dm = 0$).

model	$N(D^0)$	$N(\bar{D}^0)$	$N(D^0 + \bar{D}^0)$
Glauber Model	0.033	0.051	0.084
Hadron Gas	0.26	0.41	0.67
SMES	4.1	6.4	10.5
exp. result	-0.41 ± 0.51	0.05 ± 0.54	-0.36 ± 0.74

Table 8.1: *The expected yield of neutral D mesons for different models of the collisions (see text). An error of at least 20% should be assigned to these expectations.*

The three different models are the Statistical Model of the Early Stage (dotted line), the Hadron Gas Model (dashed line) and a Glauber-model superposition of independent nucleon-nucleon collisions (full line, coinciding with the line at $dN/dm = 0$).

A more quantitative comparison of the results to the different models is presented in Table 8.1, where expectations for D^0 and \bar{D}^0 are also quoted separately.

Within the Hadron Gas Model and the SMES, only total (open) charm yields are calculated. According to PYTHIA, 48% of the charm quarks hadronises into a D^0 , while 75% of the anti-charm quarks form a \bar{D}^0 meson. The hidden charm yield is only a very small fraction ($< 10^{-3}$) of the total charm yield and can therefore be neglected. These values are used to calculate the expected D meson yields from the Hadron Gas Model (0.55 open charm pairs per event) and the SMES yield (17 charm quarks). For the Glauber calculation, the total neutral D meson yield of $1.5 \cdot 10^{-4}$ was used and an average number of collisions $N_{coll} = 561$ per event, which was calculated using a simple Monte Carlo program based on the Woods-Saxon distribution. The resulting yields are presented together with the experimental results in Table 8.1. An error of at least 20% should be assigned to the different model expectations, arising from several uncertainties in the calculation.

Note that the difference between the kaon yields in the Hadron Gas Model and the SMES are not very large, while the difference in charm production is more than a factor of 10. This is mainly due to the much higher temperature in the SMES, which is the initial temperature and not the hadronisation temperature.

The expected yield of charm quarks in the SMES is much higher than the observed number, which either means that no QGP is formed or that it does not exist long enough to reach the equilibrium charm content. The present sensitivity is not enough to decide whether the charm yield is compatible with a Glauber-model superposition of nucleon-nucleon collisions or rather with the equilibrium Hadron Gas.

Comparing these result to the strangeness results, we conclude that while the strangeness yield is compatible with the equilibrium QGP expectation, the charm yield is not. The equilibration time in the QGP generally depends on the mass of the particle and the temperature [9]. It is therefore not excluded that the charm yield does not reach the equilibrium value, even if a QGP briefly exists, while the strangeness yield does.

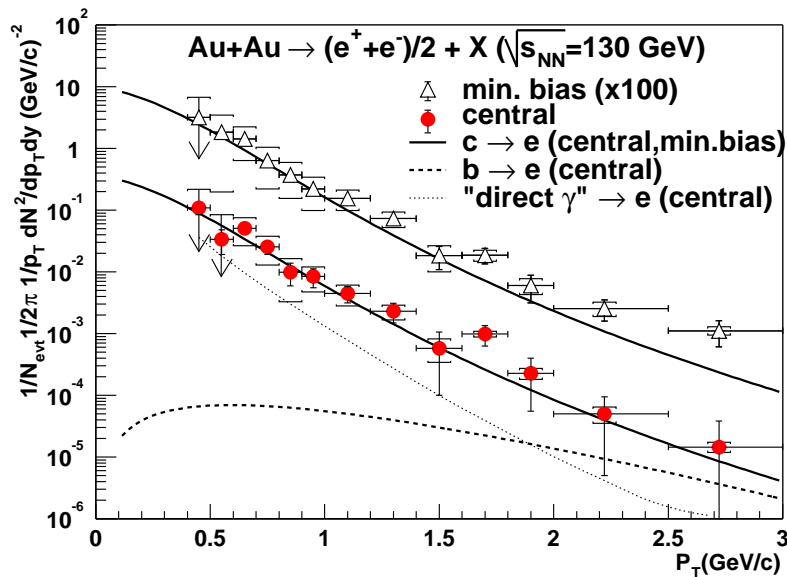


Figure 8.2: *Transverse momentum spectra of electrons after subtraction of contributions of light hadron decays and gamma conversions, as measured by PHENIX [55]. Indicated are the measured spectra in minimum bias and central events and the contributions to these spectra from charm, beauty and photon production according to PYTHIA.*

8.2 Open charm at RHIC

The SMES clearly provides a reasonable description of strangeness production but fails to predict charm production at the SPS. As discussed in the previous section, this could be due to the longer equilibration time for charm production compared to strangeness production. At RHIC, the estimated energy densities are higher, leading to shorter equilibration times. This, in combination with the expected longer time to hadronisation, possibly allows the charm content to reach the equilibrium value. If an equilibrium QGP is formed at RHIC energies, even a relatively moderate temperature of 185 MeV would already give an enhancement of a factor of two over the Glauber-model calculation [54].

A first result on charm production at RHIC energies was obtained by the PHENIX collaboration [55]. They measured the transverse momentum spectrum of electrons produced in central gold-gold collisions at $\sqrt{s}=130$ GeV. At high transverse momentum, a large fraction of the electrons comes from decays of D mesons. The transverse momentum spectra of electrons after subtraction of the contributions from decays of light mesons and photon conversions are shown in Figure 8.2, for both central and minimum bias gold-gold collisions. For comparison, the expected contributions from charm and beauty decays and direct photons as calculated with PYTHIA are also shown.

The charm yield was determined using a fit of the measured electron spectrum with the electron spectrum expected from semileptonic decays of open charm as calculated using PYTHIA, in the range $p_t > 0.8$ GeV. The result was scaled down using the number of binary collisions N_{coll} and is compared to expectations for proton-proton collisions from PYTHIA and next-to-leading order QCD calculations in Figure 8.3. Clearly, the measured value is compatible with a Glauber-model scaling of the expected proton-proton cross section. The present result, however, still has large errors, both due to uncertainties in

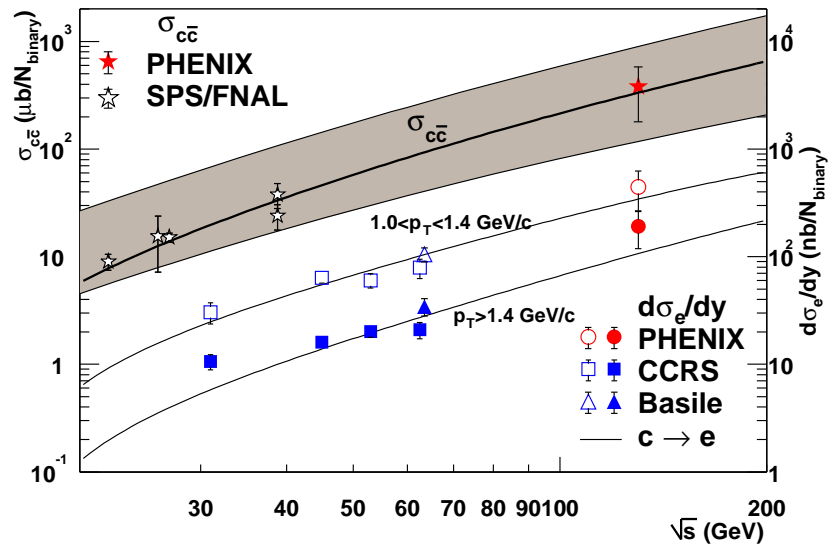


Figure 8.3: Comparison of the total cross section for charm production in Au-Au collisions as measured by the PHENIX collaboration (full star) to values measured in proton-proton collisions at lower energies (open stars). The PHENIX result has been scaled down by the number of elementary collisions N_{coll} in Au-Au collisions. Also shown are the expectations from PYTHIA and a next-to-leading-order QCD calculation. The squares, circles, and triangles indicate the measured cross section for electron production, and the lower set of curves indicate the electron production expected from open charm production. [55]

the analysis and due to the extrapolation to full phase space. In the next few years, more accurate measurements of open (and hidden) charm will become available, eventually allowing to distinguish between the different models for charm production.

Chapter 9

Conclusion

From the data as presented in Chapters 5 and 7 and the comparisons to models and data at other energies, as presented in Chapters 6 and 8, we would like to conclude the following. First of all, the observation that the transverse momentum spectra can be described by a radially expanding thermal source and the fact that the K/π ratios are higher in nucleus-nucleus collisions than in elementary collisions certainly indicate that the particle densities in the collisions are very high and that scattering between produced particles plays an important role in the evolution of the system. The particle yields and the transverse momentum spectra can even be described using equilibrium thermodynamics.

These observations can all be made within a hadronic picture of the dynamics in the system, be it the Hadron Gas Model, based on thermodynamics, or microscopic models based on scattering dynamics between hadrons. In fact, the Hadron Gas Model describes both the AGS data at low collision energies and the results at higher SPS energies presented in this thesis. At low energies, the thermodynamic parameters T and μ_B determined from fits to the data, turn out to be relatively far from the phase boundary as calculated with lattice QCD. At SPS energies, however, the thermodynamic parameters are close to, or even at, the phase boundary. Unfortunately, these results do not tell us whether the phase boundary has actually been crossed during the evolution of the system.

According to the Statistical Model of the Early Stage (SMES), the observed energy dependence of strangeness production is compatible with a phase transition to a QGP at collision energies just below 40 $A\cdot\text{GeV}$. At higher energies, the strangeness to entropy (or pion) ratio in this model is very close to values expected from the Hadron Gas Model with small baryon chemical potential and a temperature of approximately 170 MeV. This makes it difficult to distinguish between both scenarios by measuring strange particle production at higher energies. Within the SMES, the strangeness to entropy ratio will, however, sharply peak around the phase transition. The present data are in agreement with this expectation, but the upcoming measurements by NA49 at 20 and 30 $A\cdot\text{GeV}$ will test this prediction more precisely.

The upper limit as obtained for open charm production in central 158 $A\cdot\text{GeV}$ Pb-Pb collisions is clearly not compatible with equilibrium production in a hot ($T = 264$ MeV) QGP, as expected by the SMES. This could mean either that no QGP is formed or that the temperature and life-time of the QGP are such that the charm quark does not reach equilibrium, while the strange quark does. In a QGP scenario, one would expect that at higher energies, for example at RHIC, the equilibrium charm yield can be reached.

First data from RHIC do not point in this direction, but more detailed measurements and theoretical calculations are needed to draw firm conclusions.

The data presented in this thesis, will, together with new measurements of kaon and pion production at 20 and 30 $A\cdot\text{GeV}$ and more detailed investigations of charm production at RHIC, allow to resolve many of the remaining questions.

References

- [1] A. Chodos, R. L. Jaffe, K. Johnson, Charles B. Thorn, and V. F. Weisskopf, *A new extended model of hadrons*, Phys. Rev. **D9** (1974) 3471.
- [2] C.-Y. Wong, *Introduction to high-energy heavy-ion collisions*, World Scientific, 1994.
- [3] L.D. Landau and E.M. Lifshitz, *Statistical Physics*, volume 5 of *Course of Theoretical Physics*, Pergamon Press, 1969, Translated from Russian by J.B. Sykes and M.J. Kearsley.
- [4] F. Karsch, E. Laermann, and A. Peikert, *The pressure in 2, 2+1 and 3 flavour QCD*, Phys. Lett. **B478** (2000) 447.
- [5] F. Karsch, *Lattice results on QCD thermodynamics*, Nucl. Phys. **A698** (2002) 199.
- [6] S. Margetis et al. [NA49 collaboration], *Transverse energy production in Pb-208 + Pb collisions at 158 GeV per nucleon*, Phys. Rev. Lett. **75** (1995) 3814.
- [7] G. Agakishiev et al. [CERES/NA45 collaboration], *Low-mass e^+e^- pair production in 158 AGeV Pb Au collisions at the CERN SPS, its dependence on multiplicity and transverse momentum*, Phys. Lett. **B422** (1998) 405.
D. Adamova et al. [CERES collaboration], *New results from CERES*, Nucl. Phys. **A698** (2002) 253.
M. M. Aggarwal et al. [WA98 collaboration], *Observation of direct photons in central 158 AGeV Pb-208 + Pb-208 collisions*, Phys. Rev. Lett. **85** (2000) 3595.
C. Gale, *Direct photons and thermal dileptons: A theoretical review*, Nucl. Phys. **A698** (2002) 143.
- [8] M. C. Abreu et al. [NA50 collaboration], *The dependence of the anomalous J/ψ suppression on the number of participant nucleons*, Phys. Lett. **B521** (2001) 195.
M. C. Abreu et al. [NA50 collaboration], *Recent results on J/ψ from experiment NA50*, Nucl. Phys. **A698** (2002) 127.
- [9] J. Rafelski and B. Muller, *Strangeness production in the Quark - Gluon Plasma*, Phys. Rev. Lett. **48** (1982) 1066.
P. Koch, B. Muller, and J. Rafelski, *Strangeness in relativistic heavy ion collisions*, Phys. Rept. **142** (1986) 167.

- [10] R.J. Glauber and G. Matthiae, *High-energy scattering of protons by nuclei*, Nucl. Phys. **B21** (1970) 135.
- [11] K. J. Eskola, K. Kajantie, and J. Lindfors, *Quark and gluon production in high-energy nucleus-nucleus collisions*, Nucl. Phys. **B323** (1989) 37.
- [12] C. W. De Jager, H. De Vries, and C. De Vries, *Nuclear charge and magnetization density distribution parameters from elastic electron scattering*, Atom. Data Nucl. Data Tabl. **36** (1987) 495.
- [13] A. Białas, M. Bleszyński, and W. Czyż, *Multiplicity distributions in nucleus-nucleus collisions at high-energies*, Nucl. Phys. **B111** (1976) 461.
- [14] M. C. Abreu et al. [NA50 collaboration], *J/ψ and Drell-Yan cross-sections in Pb Pb interactions at 158 GeV/c per nucleon*, Phys. Lett. **B410** (1997) 327.
- [15] B. Nilsson-Almqvist and E. Stenlund, *Interactions between hadrons and nuclei: The Lund Monte Carlo — FRITIOF version 1.6 —*, Comp. Phys Commun. **43** (1987) 387.
- B. Anderson, G. Gustafson, and Hong Pi, *The FRITIOF model for very high energy hadronic interactions*, Z. Phys. **C57** (1993) 485.
- [16] S. Jeon and J. Kapusta, *Linear extrapolation of ultrarelativistic nucleon nucleon scattering to nucleus nucleus collisions*, Phys. Rev. **C56** (1997) 468.
- [17] K. Werner, *Strings, pomerons, and the VENUS model of hadronic interactions at ultrarelativistic energies*, Phys. Rept. **232** (1993) 87.
- [18] H. Sorge, *Flavor production in Pb(160 AGeV) on Pb collisions: Effect of color ropes and hadronic rescattering*, Phys. Rev. **C52** (1995) 3291.
- [19] S. A. Bass et al., *Microscopic models for ultrarelativistic heavy ion collisions*, Prog. Part. Nucl. Phys. **41** (1998) 225.
- M. Bleicher et al., *Relativistic hadron hadron collisions in the ultra-relativistic quantum molecular dynamics model*, J. Phys. **G25** (1999) 1859.
- [20] W. Cassing and E. L. Bratkovskaya, *Hadronic and electromagnetic probes of hot and dense nuclear matter*, Phys. Rept. **308** (1999) 65.
- E. L. Bratkovskaya et al., *Aspects of thermal and chemical equilibration of hadronic matter*, Nucl. Phys. **A675** (2000) 661.
- [21] B. Andersson, G. Gustafson, G. Ingelman, and T. Sjöstrand, *Parton fragmentation and string dynamics*, Phys. Rept. **97** (1983) 31.
- [22] S. Frixione, M. L. Mangano, P. Nason, and G. Ridolfi, *Heavy-quark production*, Adv. Ser. Direct. High Energy Phys. **15** (1998) 609.
- [23] P. Braun-Munzinger, D. Miskowiec, A. Drees, and C. Lourenco, *Open charm contribution to the dilepton spectra produced in nuclear collisions at SPS energies*, Eur. Phys. J. **C1** (1998) 123.

-
- [24] T. Sjöstrand et al., *High-energy-physics event generation with PYTHIA 6.1*, Computer Phys. Commun. **135** (2001) 238.
- [25] S. Aoki et al. [WA75 collaboration], *Charm production by 350 GeV/c π^- interactions in nuclear emulsion*, Prog. Theor. Phys. **87** (1992) 1305.
- [26] E. Fermi, *High-energy nuclear events*, Prog. Theor. Phys. **5** (1950) 570.
- [27] L. D. Landau, *On the multiparticle production in high-energy collisions*, Izv. Akad. Nauk SSSR Ser. Fiz. **17** (1953) 51, Also in Collected Papers of L.D. Landau, editor D. Ter Haar, Pergamom press 1965, p. 569.
S. Z. Belenkij and L. D. Landau, *Hydrodynamic theory of multiple production of particles*, Nuovo Cim. Suppl. **3S10** (1956) 15, Also in Collected Papers of L.D. Landau, editor D. Ter Haar, Pergamom press 1965, p. 665.
- [28] R. Hagedorn, *Thermodynamics of strong interactions*, CERN yellow report 71-12, Lecture given in the Academic Training Programme of CERN 1970-1971.
R. Hagedorn, *The long way to the statistical bootstrap model*, Invited talk at NATO Advanced Study Workshop on Hot Hadronic Matter: Theory and Experiment, Divonne-les-Bains, Switzerland, 27 Jun - 1 Jul 1994.
- [29] J. Cleymans and K. Redlich, *Chemical and thermal freeze-out parameters from 1 AGeV to 200 AGeV*, Phys. Rev. **C60** (1999) 054908.
- [30] Z. Fodor and S. D. Katz, *Lattice determination of the critical point of QCD at finite T and μ* , JHEP **03** (2002) 014.
- [31] P. Braun-Munzinger, J. Cleymans, H. Oeschler, and K. Redlich, *Maximum relative strangeness content in heavy ion collisions around 30 AGeV*, Nucl. Phys. **A697** (2002) 902.
- [32] S. V. Afanasiev et al. [NA49 collaboration], *Energy dependence of pion and kaon production in central Pb + Pb collisions*, Phys. Rev. **C66** (2002) 054902.
- [33] A. Tounsi and K. Redlich, *Strangeness enhancement and canonical suppression*, hep-ph/0111159.
- [34] M. I. Gorenstein, A. P. Kostyuk, H. Stöcker, and W. Greiner, *Statistical coalescence model with exact charm conservation*, Phys. Lett. **B509** (2001) 277.
- [35] M. Gaździcki and M. I. Gorenstein, *On the early stage of nucleus nucleus collisions*, Acta Phys. Polon. **B30** (1999) 2705.
- [36] S. Afanasev et al. [NA49 collaboration], *The NA49 large acceptance hadron detector*, Nucl. Instrum. Meth. **A430** (1999) 210.
- [37] C. Höhne et al. [NA49 collaboration], *System size dependence of strangeness production at 158 AGeV*, nucl-ex/0209018.
H. G. Fischer [NA49 collaboration], *Elementary hadronic interactions at the CERN SPS*, hep-ex/0209043.

- S. V. Afanasev et al. [NA49 collaboration], *New results from NA49*, Nucl. Phys. **A698** (2002) 104.
- [38] G. E. Cooper, *Baryon Stopping and Hadronic Spectra in Pb–Pb Collisions at 158 GeV/nucleon*, Ph. D. thesis, Lawrence Berkeley National Laboratory, 2000.
- [39] H.A. Bethe, *Theory of the passage of fast corpuscular rays through matter*, Annalen der Physik **5** (1930) 325.
F. Bloch, Z. Physik **81** (1933) 363.
- [40] R.M. Sternheimer and R.F. Peierls, *General expression for the density effect for the ionization loss of charged particles*, Phys. Rev. **B3** (1971) 3681.
- [41] C. Roland, *Flavor Fluctuations in Central Pb+Pb Collisions at 158 GeV/Nucleon*, Ph. D. thesis, Universität Frankfurt, 1999.
- [42] D. Decamp et al. [ALEPH collaboration], *Aleph: A detector for electron - positron annihilations at lep*, Nucl. Instrum. Meth. **A294** (1990) 121.
- [43] G. I. Veres, *New developments in understanding and correction of dE/dx* , Technical report, KFKI Research Institute for Particle and Nuclear Physics, Budapest, 2000, NA49 note, see <http://na49info.cern.ch/>.
- [44] J.D. Landau, *On the energy loss of fast particles by ionisation*, J. Phys USSR **8** (1944) 201, Also in Collected Papers of L.D. Landau, Editor D. Ter Haar, Pergamom press 1965, p. 417.
- [45] R. Brun, R. Hagelberg, M. Hansroul, and J.C. Lassalle, *Geant: Simulation program for particle physics experiments. user guide and reference manual*, Technical report, CERN-DD-78-2-REV.
- [46] M. Y. Toy, *Baryon Stopping and Charged Particle Production from Lead-Lead Collisions at 158 GeV per Nucleon*, Ph. D. thesis, University of California Los Angeles, 1999.
- [47] Particle Data Group, *Review of particle physics*, Eur. Phys. J. **C15** (2000) .
- [48] F. Cooper and G. Frye, *Comment on the single particle distribution in the hydrodynamic and statistical thermodynamic models of multiparticle production*, Phys. Rev. **D10** (1974) 186.
- [49] E. Schnedermann, J. Sollfrank, and U. W. Heinz, *Thermal phenomenology of hadrons from 200 AGeV S+S collisions*, Phys. Rev. **C48** (1993) 2462.
- [50] M. van Leeuwen et al. [NA49 collaboration], *Recent results on spectra and yields from NA49*, nucl-ex/0208014, Presented at Quark Matter 2002, Nantes, France.
- [51] F. Becattini, M. Gaździcki, and J. Sollfrank, *On chemical equilibrium in nuclear collisions*, Eur. Phys. J. **C5** (1998) 143.
- [52] F. Becattini, private communication.

- [53] D. Ouerdane et al. [BRAHMS collaboration], *Rapidity dependence of charged particle yields for Au + Au at $\sqrt{s_{NN}} = 200$ GeV*, nucl-ex/0212001, Presented at Quark Matter 2002.
- [54] M. I. Gorenstein, A. P. Kostyuk, L. D. McLerran, H. Stöcker, and W. Greiner, *Open and hidden charm production in Au + Au collisions at RHIC energies*, hep-ph/0012292.
- [55] K. Adcox et al. [PHENIX collaboration], *Measurement of single electrons and implications for charm production in Au+Au collisions at $\sqrt{s_{NN}} = 130$ GeV*, Phys. Rev. Lett. **88** (2002) 192303.

Samenvatting

Dit proefschrift beschrijft een onderzoek naar deeltjesproductie in botsingen van atoomkernen bij hoge energie. Het doel van een dergelijk onderzoek is het bestuderen van kernmaterie bij hoge dichtheid en temperatuur. De fundamentele bouwstenen van de atoomkern, quarks en gluonen, komen niet vrij in de natuur voor maar zijn altijd opgesloten in hadronen, zoals het proton en het neutron. Uit rooster-ijkberekening van de sterke wisselwerking verwacht men dat kernmaterie bij een temperatuur van ca. 170 MeV en een energiedichtheid van ca. $1 \text{ GeV}/\text{fm}^3$ een faseovergang doormaakt naar een quark-gluonplasma (QGP), waarin quarks en gluonen vrij kunnen bewegen over afstanden die veel groter zijn dan de typische straal (ca. 1 fm) van een hadron. Deze toestand is vergelijkbaar met de toestand van het heelal in de eerste microseconden na de Oerknal.

In het proefschrift worden twee verschillende metingen aan lood-loodbotsingen beschreven, namelijk een meting van de energieafhankelijkheid van strangenessproductie en, bij de hoogste bundelenergie van $158 A \cdot \text{GeV}$ ($\sqrt{s} = 17.3 \text{ GeV}$ per nucleon), een meting van charmproductie. Deze metingen zijn verricht met de NA49-detector aan het Super Proton Synchrotron (SPS) te CERN.

De detector bestaat uit vier grote Time Projection Chambers (TPC), waarmee de sporen van de geproduceerde (geladen) deeltjes gemeten worden. In elke loodkernbotsing worden ongeveer duizend sporen gedecteerd in de TPC's. Voor ieder deeltje wordt de impuls berekend uit de kromming van het spoor in een magneetveld. De NA49-detector kan elektronen, pionen, kaonen en protonen gedeeltelijk onderscheiden door de meting van het energieverlies (dE/dx) door ionisatie van het detectorgas in de TPCs en door een meting van de vluchttijd met speciale scintillatiedetectoren. Centrale botsingen worden geselecteerd met een calorimeter die de totale energie meet van alle (bundel-)nucleonen die geen deel hebben genomen aan de interactie.

De dE/dx -meting in de detector is gebruikt voor de identificatie van kaonen, die het grootste deel van de geproduceerde strange quarks bevatten. Het resultaat van de analyse zijn verdelingen in rapiditeit en transversale impuls p_t van zowel positieve als negatieve kaonen bij 40, 80 en $158 A \cdot \text{GeV}$ bundelenergie.

De analyse van de p_t -spectra in het kader van een hydrodynamisch model, zoals beschreven in het proefschrift, toont aan dat de spectra redelijk goed beschreven worden door aan te nemen dat de deeltjes voortkomen uit een radiëel uitzettende thermische bron.

De acceptantie van de detector is zodanig dat slechts een kleine extrapolatie naar ongemeten gebieden in rapiditeit en p_t nodig is om het totale aantal positieve en negatieve kaonen dat in elke botsing geproduceerd wordt te berekenen. Het door NA49 gemeten aantal pionen (het meest-geproduceerde deeltje) is gebruikt om bij elke energie de verhouding tussen het totaal aantal kaonen en pionen te bepalen. Uit een vergelijking van deze resultaten met resultaten bij lagere (AGS) en hogere (RHIC) energieën, blijkt dat de

verhouding van het aantal negatieve kaonen tot pionen monotoon toeneemt met de botsingsenergie. De verhouding van positieve kaonen en pionen daarentegen, stijgt sterk bij AGS-energieën, daalt dan weer tussen 40 en 80 $A \cdot \text{GeV}$ (SPS) en is min of meer constant vanaf 80 $A \cdot \text{GeV}$ bundelenergie tot aan de RHIC-energie van $\sqrt{s} = 200 \text{ GeV}$ per nucleon.

In het proefschrift worden de metingen vergeleken met twee modellen die de botsing beschrijven zonder aan te nemen dat een faseovergang naar een QGP plaatsvindt, namelijk het Hadron Gas Model en het microscopisch transportmodel RQMD. Beide modellen beschrijven ruwweg de waargenomen energieafhankelijkheid van de kaon-pionverhoudingen, maar zijn vooralsnog niet in staat de gemeten afname van de K^+/π^+ -verhouding tussen 40 en 80 $A \cdot \text{GeV}$ te reproduceren.

Het ‘‘Statistical Model of the Early Stage’’ (SMES), dat expliciet een quark-gluonfase introduceert in de beschrijving van kernbotsingen, reproduceert wel de gemeten afname in de verhouding tussen strangeness- en pionproductie bij SPS-energieën. Volgens het model neemt de relatieve strangenessproductie toe met de bundelenergie tot de faseovergangstemperatuur wordt bereikt, bij een bundelenergie tussen de 20 en 30 $A \cdot \text{GeV}$. De afname in de verhouding tussen strangeness- en pionproductie bij SPS-energieën is een direct gevolg van de overgang van (effectieve) hadronische naar quarkvrijheidsgraden bij de faseovergang. Dit model is vooralsnog het best in overeenstemming met de experimentele resultaten, maar om andere verklaringen uit te sluiten zijn metingen nodig tussen de hoogste AGS-energie en de laagste door ons gemeten energie. Als inderdaad een sterk verhoogde strangenessproductie wordt waargenomen in dergelijke metingen, is dat een sterke aanwijzing dat de faseovergang inderdaad plaatsvindt.

De productie van charm quarks in een QGP in thermisch evenwicht, zoals geformuleerd in het SMES, is 10 tot 100 keer groter dan verwachtingen gebaseerd op het Hadron Gas Model of op extrapolaties van charmproductie in proton-protonbotsingen. Om deze voorspelling voor charmproductie te verifiëren is, door middel van een invariante-massa-analyse gezocht naar het verval van neutrale D -mesonen in een kaon en een pion. Om het signaal zo goed mogelijk van de grote combinatorische achtergrond te kunnen onderscheiden, is de analyse uitgevoerd met alle ca. 4 miljoen door NA49 geregistreerde lood-loodbotsingen. Het signaal van het D -mesonverval blijkt echter toch te zwak om detecteerbaar te zijn. De gevonden bovenlimiet voor charmproductie is beduidend lager dan de voorspelling van het SMES, gebaseerd op thermische charmproductie in een QGP met een temperatuur van 264 MeV. Dit betekent, in het kader van het SMES, dat er geen QGP gevormd wordt, ofwel dat het te kort bestaat om de charmproductie tot thermisch evenwicht te laten komen.

Acknowledgements

The past four years of Ph.D. research have really been a great experience, thanks to many people at NIKHEF, Utrecht University and in the NA49 collaboration. Without your readiness to answer questions and to discuss technical matters as well as physics, it would not have been such a worthwhile experience.

I would like to mention a few people who have contributed in a specific way to my work as a graduate student. First of all, I would like to thank my promotor, René Kamermans, for providing the possibility to do this Ph.D. and for making me finish this work (almost) on time. Michiel Botje, my co-promotor, has been witness of my work on a more daily basis and ungrudgingly provided advice on many statistical and technical issues. Michiel, I would like to thank you in particular for the absolutely invaluable education you have provided on the writing of clear and readable scientific texts. Without your help, this thesis would not have been as readable I hope it now is.

The next group of people to whom I am indebted is the NA49 collaboration. Working with you has been a very nice experience! Special thanks go to the people with whom I worked more closely together in the analysis and on technical aspects of the dE/dx treatment: Volker, Vadim, Ferenc, Gabor, Thorsten, Roland, Peter. Thanks also to Gunther and Christof for efficiently helping me on my way in the analysis and to Christoph for maintaining the Root analysis framework and large parts of the simulation software.

Marek, you have in many ways acted as my third supervisor, for which I am very grateful. By frequent phone calls and long discussions at CERN, you have closely followed the progress of the analysis, providing guidance when needed, and greatly contributed to my education in heavy ion physics.

I would also like to thank Reinhard Stock and Peter Seyboth from NA49 for being very supportive of my work.

I cannot begin to thank everyone at NIKHEF who has at some point contributed to my work or general well-being by discussions or idle chat in coffee and lunch breaks or when I barged into your office. I just hope that you also felt free to bother me with questions or to vent your complaints about compilers, networks, \LaTeX , or the weather. With the risk of being unfair to others, I would like to mention here the names of Aart, Mark, Martin and René as the ones with whom I have most often experienced the gradual transition between work at NIKHEF and a relaxing evening in a bar.

Finally, I would like to thank my parents, brother, sister and others who have had to put up with my talk about the daily chores of a Ph.D. student. Unfortunately, I cannot promise that you have heard the last of it yet....

Curriculum Vitae

Op 13 juli 1975 ben ik geboren in Amsterdam. Na een korte periode in Amstelveen gewoond te hebben, verhuisden we naar Wilnis, waar ik basisonderwijs volgde. In 1988, na mijn dertiende verjaardag, nam het middelbare-schoolleven zijn aanvang. Dat voltrok zich eerst aan het Veenlandcollege te Mijdrecht en vanaf halverwege de derde klas aan het Eckartcollege te Eindhoven. Na zes jaar, in 1993, heb ik met goed gevolg het eindexamen VWO afgelegd en was ik rijp voor de universiteit.

In 1993 begon ik dus met frisse moed aan de opleiding Materiaalkunde van de Technische Universiteit Delft, waarvan ik een jaar later het propaedeutisch examen (met lof) haalde. Weer een paar jaar later kon ik beginnen aan een afstudeeronderzoek in de vakgroep FCM2: “Fysische chemie van de vaste stof”. Dat afstudeeronderzoek bestond uit een combinatie van de experimentele bepaling van de (rooster-)rek in een opgedampte nikkellaag met behulp van röntgendiffractie en uitgebreide berekeningen aan spanningstoestanden om het verband tussen macroscopische spanningen en de meetresultaten beter te begrijpen. Op 15 december 1998 ontving ik mijn ingenieursbul in de Materiaalkunde (met lof).

Tegen die tijd was het duidelijk dat het wetenschappelijk onderzoek me trok en zo ben ik dan per 1 februari 1999 begonnen aan een promotie-onderzoek aan de Universiteit Utrecht, werkend in de ALICE-groep op NIKHEF, waarvan dit proefschrift het resultaat is.